Ultrafast dynamics of the laser-induced solid-to-liquid phase transition in aluminum

A thesis presented

by

Maria Kandyla

to

The Division of Engineering and Applied Sciences

in partial fulfillment of the requirements

for the degree of

Doctor of Philosophy

in the subject of

Applied Physics

Harvard University

Cambridge, Massachusetts

September 2006

Ultrafast dynamics of the laser-induced

solid-to-liquid phase transition in aluminum

Eric Mazur   Maria Kandyla

ABSTRACT

This dissertation reports the ultrafast dynamics of aluminum during the solid-to-liquid phase transition of melting after excitation by an intense femtosecond laser pulse. Photoexcitation with intense femtosecond laser pulses is known to create a novel melting mechanism called non-thermal melting. This mechanism has been observed repeatedly in semiconductors, but not yet in metals. We investigate the melting mechanism of aluminum by monitoring the reflectivity response following excitation by an intense laser pulse. We employ an optical pump–probe technique designed to measure broadband reflectivity across the visible spectrum with femtosecond time resolution.

A non-thermal melting mechanism was proposed for aluminum by optical experiments that demonstrated transition of the optical properties from solid to liquid values within 500 fs after phototexcitation. This result was later challenged by electron diffraction experiments, which showed that the lattice loses long range order within 3.5 ps during photoinduced melting. This time scale implies conventional thermal melting.

We find that the broadband optical properties during the solid-to-liquid phase transition in aluminum agree with the results obtained by the electron diffraction experiments. The transition of the broadband reflectivity from solid to liquid values is complete within 1.5 – 2 ps in our experiments, which is compatible with thermal melting. We don't observe time scales on the order of 500 fs. All the experimental evidence in this dissertation lead to the conclusion that the laser-induced, solid-to-liquid phase transition in aluminum is a thermal process.

Table of Contents

List of Figures

Acknowledgements

Everybody likes to think of their PhD as their personal contribution to the matters of science. However, no one would be able to complete such a long-lasting and demanding commitment without the support of numerous friends, relatives, and colleagues. This section is entirely devoted to all the people who were there for me.

First and foremost I want to thank my parents and sister, who, although so far away, were always so close. Their support was infinite and unconditional from the day I started applying to grad school to the day I had to move to a different continent to the various unlucky moments in a grad student's life to the completion of the dissertation and joy. It would be literally impossible to be here without them. I would also like to thank the members of my extended family who I am so lucky to have and who were also providing their support and were there to welcome me every time I would return to Greece.

At Harvard the Mazur group became a second family. Much in the same way that when we are younger we spend day-to-day time with our family, we share the same space, and we eat our meals together, I found myself repeating this lifestyle with the other members in the group, laundry not included. In the lab we help each other, we share our problems, we go out and have fun, we organize trips, we share advice, we fight and make up, in short we live. It is my pleasure to thank each and every member of the Mazur group for making the research presented here possible to even think about. A PhD in experimental

science is the result of team work and good experiments require good groups to support them.

The existence and character of the group is solely determined by our advisor, Professor Eric Mazur. Eric makes a huge effort to provide an environment where everyone feels comfortable, no one feels like being judged, everyone feels important and respected. Moreover, Eric promotes so much the spirit of collaboration that he creates generations of team scientists, spreading good practice throughout the academic community. I am grateful to Eric for providing a human environment in which young people can work without giving up their lives. It was a pleasure doing science with him and I learned many precious lessons about how to interact with colleagues, lead a group no matter how small or big, and assign responsibilities in a gracious and respectful manner.

I was extremely lucky to meet such a noble person as Rafael during the first weeks of grad school. I want to thank Rafa wholeheartedly for being a real friend, for being generous in all material, emotional, and spiritual ways, for being good and positive and happy. More than that, I want to thank him because every day when he walks in the lab he opens up his heart and soul, setting the example of being first human and then a scientist, and spreading a warm feel around us.

Rafa was not the only person that welcomed me warmly when I joined the group. I was actually glad to find a welcoming atmosphere among all the other graduate students who helped a lot during the first months of research. First, I want to thank Chris who worked with me extensively and trained me on pretty much everything. It was a pleasure working with him and after he graduated I would often remember our collaboration with nostalgia, especially some evenings when I was alone in the dark and nothing seemed to be working. I would also want to thank Jon for being thoughtful and polite; Jim for being witty and fun; Mike for all the good jokes and the Thursday nights out; Nan for being

discrete and well-spirited; Adam for being friendly and optimistic.

Within a few years after I joined the group many students graduated and the lab was full with new people with whom I got to spend most of the later times. It's been lots of fun to complete my graduate student life having them around. Iva, Brian, and Sam, who are about to graduate, were actually along most of the way. I would like to thank them for being such good colleagues and for contributing to the shaping of our small community with valuable ideas, as well as helping out my research with precious feedback and technical support. I would like to thank Geoff for introducing me to the modern American lifestyle, with lots of innovative language tricks. Loren, Prakriti, Tina, and Jessica were not only fun people to hang out with, but also much sought-after female colleagues, which make me proud because they prove that despite the ongoing –and fortunately shrinking– gender gap, there are great women scientists out there. I would particularly like to thank Tina for all her help with the research presented in this dissertation. Mark and Eric close our graduate student circle vividly, and they are both active and full of ideas which we are glad to receive.

Apart from the graduate students I was really lucky to interact with many other Professors and post-docs that provide us with their experience and serve as role models as we are shaping our academic profiles. First, I would like to thank the members of my committee, Profs. Jene Golovchenko, Mike Aziz, and Eric Heller for supporting me during the PhD years and for their great insight concerning my findings and interpretation. I certainly want to thank Arantza and Cleber with whom I collaborated closely. They are both excellent scientists that offered me the chance to improve my skills by learning next to them, but also really warm and nice people, and I am glad I met them. Tommaso was not only the chemist we all adored, but also a great person to have in our group. I also want to thank Tobias, Mengyan, Limin, Veronica, Mercedes, Alex, and Catherine for all their input and help. Of course the group would be unable to function without the technical support

provided by "Mr. Awesome" Vijay, who was kind enough to put up with us when we were discussing several outrageous and home-built dating theories in the same room where he was trying to work.

Of course there is life outside the lab as well. The Harvard experience would be incomplete without the presence of the Greek community which gave me the chance to interact with students from other fields and also to make some valued friends that always helped put things in perspective. I want to thank Tzeni, Jordan, Eleni, Nikos, Giorgos, Loizos, Nikolas, Vangelis, Emma, Leonidas, Eva, Anna, Alkisti, and all the rest, graduates and undergraduates, who are creating a hospitable atmosphere for those who sometimes wish they could be closer to home. Dominik and Parisa are dear friends who are sadly away now, but I hope our paths will cross again in the future. Finally, I would like to thank Jon for being next to me during a particularly challenging last PhD year and for putting up with all my complaints about Boston's climate, fair or unfair.

The shock of being away from my friends in Greece was devastating when I first moved to Boston. This gave me the chance to realize how precious they are to me. I want to thank them for being around and for giving me some of the best home trips in the past few years. I also want to thank them for the great times we had together as undergrads. Looking back in my undergrad years, all I can remember is fun and joy and such good laughs. All in all it was a great time. I want to thank Eleni because she continues to be a best friend, with all the deep meaning of the word. Her optimism, happiness, compassion, love, and friendship were strong enough to be covering the entire distance from San Francisco to Boston all these years and to reach me intact, soothing, and golden.

This dissertation was written during controversial events of global significance. First, it was the soccer world cup, which served as an exercise in discipline. Then, it was the war in Lebanon which served as an exercise in tolerance. Scientists often forget the

world around them, but the world itself moves with breathtaking rush. It is important that as a community we make sure to keep up with human actions as much as we keep up with nature's slow unfolding of secrets.

<div align="right">

Maria Kandyla
Cambridge, Massachusetts
September, 2006

</div>

Citations to Published Work

Parts of this dissertation cover research reported in the following articles:

[1] C. A. D. Roeser, M. Kandyla, A. Mendioroz, and E. Mazur, "Optical control of coherent lattice vibrations in tellurium," *Phys. Rev. B*, vol. 70, p. 212302, 2004.

[2] M. Kandyla, C. A. D. Roeser, E. Mazur, and S. Kudryashov, "Intraband and interband optical deformation potential in femtosecond-laser excited α-Te," *submitted to Phys. Rev. B*, 2006.

[3] M. Kandyla, T. Shih, and E. Mazur, "Ultrafast dynamics of the laser-induced solid-to-liquid phase transition in aluminum," *submitted to Phys. Rev. B*, 2006.

[4] M. Shen, J. E. Carey, C. H. Crouch, M. Kandyla, H. A. Stone, and E. Mazur, "High-density regular nanospike array formed via femtosecond laser irradiation in water," *submitted to Opt. Commun.*, 2006.

For my parents and sister

who have taught me how to love.

But the universe speaks not only of the ultimate things

(which it does always in an obscure fashion)

but also of closer things, and then it speaks quite clearly.

UMBERTO ECO, THE NAME OF THE ROSE

Chapter 1

Introduction

The study of solids is one of the richest and most successful fields of physics. There are many reasons that contribute to the great interest in the field. From a theoretical point of view, lattice symmetry allows for analytical and elegant in-depth analysis. From an experimental point of view, solids are easy to handle and remain relatively unchanged over long periods of time allowing for reproducible results. From the technological point of view, solids are the building block of any product that offers easy access, minimum maintenance, small volume, non-destructive transportation, long lifetime, and reliable performance.

It is of no surprise, therefore, that almost every property of solid materials has been the subject of thorough investigation. Mechanical and electrical properties, chemical reactivity, and heat transport have been characterized through numerous studies. Additionally, a big portion of scientific research has been devoted to the optical properties of solids over the course of history. First, with conventional light sources the laws of reflection and refraction in solids were established. Later, the invention of the laser in 1960 [1] gave a priceless technological boost to the optical study of materials. Furthermore, the achievement of femtosecond laser sources in 1976 [2] allowed researchers to beat the time scales of

the ionic motion in materials: for the first time we were able to blink fast enough.

The use of a femtosecond pulse as a stroboscopic probe allows the visualization of chemical bond breaking, DNA unfolding, or structural transformations of matter. The applications of femtosecond laser sources span disciplines that range from chemistry to physics to biology. Our area of focus is ultrafast electronic and lattice dynamics in solids, more specifically phase changes (semiconductor-metal, order-disorder, solid-liquid, etc.) and coherent control on ultrashort timescales. Of the many ultrafast phenomena that have been investigated, ultrafast phase transitions are perhaps the most challenging to characterize fully due to the large number of electron-electron interactions at high excitation densities and the significant lattice distortions that ensue. Early experiments on semiconductors measured transient changes in linear and second harmonic reflectivity within a few hundred femtoseconds. While these experiments indicated that significant material changes occur and determined the relevant time scales, they did not provide sufficient information to deduce the precise nature of those changes. Recently, femtosecond x-ray and electron pulses have been employed to study ionic motion during non-thermal melting and other laser-induced phase changes. In x-ray and electron probe experiments, a loss of lattice ordering can be measured directly, but changes in lattice bonding and electron energy levels cannot. Conversely, femtosecond optical measurements, while unable to directly monitor ionic motion, provide a detailed view of the carrier dynamics responsible for these transitions. Optical techniques offer the additional advantages of higher time resolution and of measuring material response at wavelengths relevant to industrial applications. Thus, time-resolved optical, x-ray, and electron probe techniques are complementary tools for fundamental investigations of intensely photo-excited materials.

The topic of this thesis is the study of the laser-induced solid-to-liquid phase transition of melting. The material to which the experiments were applied is aluminum,

one of the most widely used metals. When using an intense femtosecond pulse to initiate the transition it is straightforward to deposit heat rapidly into the lattice to bring it up to its phase transition temperature. With a femtosecond probe we have the luxury to investigate some unique questions. Is it possible to heat the lattice so quickly that theoretical models would predict that the lattice would melt faster than the ions could actually move? At extreme conditions under which the lattice is no longer a bound state, can the lattice actually exist and if so, for how long? The novel melting mechanism that arises with the use of femtosecond laser pulses is called non-thermal melting. Not all materials exhibit non-thermal melting when photoexcited with a femtosecond pulse. The findings of this thesis contribute to an ongoing debate of whether the melting mechanism of aluminum goes through a thermal or a non-thermal path.

Organization of the dissertation

This dissertation is focused on the solid-to-liquid phase transition of aluminum. This of course does not mean that these were the only experiments performed in the course of the years devoted to the completion of the overall work. Significant part of our efforts was invested on ultrafast dynamics and coherent control in semiconductors. In order not to distract the flow of information too much we present these findings briefly, as an illustration of our experimental technique.

Chapter 2 provides the theoretical framework for understanding the optical response of solids and presents in detail one possible physical process to occur upon photoexcitation of a material: the solid-to-liquid phase transition, or melting. Differences between the optical response of metals and semiconductors are highlighted in an effort to elucidate the relevant physical processes.

Chapter 3 discusses the optical methods by which we can acquire time-resolved

measurements and elaborates on our variation of an optical technique, which expands on previous experimental methods. As an illustration of our technique we present results on ultrafast dynamics and coherent control in semiconductors obtained in our laboratory and we close with a discussion on the limitations of our setup.

Chapter 4 gives the context in which our contribution belongs. First we discuss the structural and optical properties of aluminum in order to help the understanding of the data we present in the next chapter. Furthermore, we present the results of previous studies on the laser-induced, solid-to-liquid phase transition of aluminum. We highlight the discrepancies between the existing results and we proceed to address them in the next chapter.

Chapter 5 presents femtosecond time-resolved measurements of the reflectivity of aluminum during the solid-to-liquid phase transition over the spectral range $1.7 - 3.5$ eV. Previous optical and electron diffraction studies have shown discrepancies in the time scale of the solid-to-liquid phase change, and have led to different interpretations of the transition mechanism. Our experiments yield optical data that agree with the electron diffraction study and verify that this transition is a thermal process mediated through the transfer of heat from the photoexcited electronic population to the lattice.

Chapter 6 summarizes our findings and highlights the most important conclusions. A series of future experiments, which aim at furthering the understanding of ultrafast dynamics in metals, is proposed.

Chapter 2

Interaction of Light with Solids

The interaction of light with solids is a rigorously investigated subject. In the pre-laser era, when the light sources were not as bright, it was the presence of matter that had an impact on the properties of light. After the invention of the laser, and with the increasing laser powers achieved in the laboratories, we are able to manipulate matter using light. The optical properties of solids and the response of substances to extreme electromagnetic conditions are of great technological importance. Light technology advances yearly and it is important to discover ways of tailoring the optical properties of materials to technological needs. In this chapter we provide the theoretical framework for understanding the optical response of solids and we present in detail one of the many physical processes to occur upon photoexcitation of a material: the solid-to-liquid phase transition, also known as melting.

2.1 Optical properties of solids

It is well established that matter affects light. For example, light reflects, refracts, becomes absorbed, or shifts in frequency when it interacts with materials. The topic of this thesis is actually the investigation of the opposite: how does light affect matter. In

both cases, however, the pertinent properties are the optical properties of matter. Optical properties such as reflectivity, absorptivity, dielectric function, optical conductivity, and nonlinear susceptibility play an essential role in the interaction of light with matter. Solids, more than any other form of matter, have been studied extensively in the presence of electromagnetic fields. The reason is twofold: first, solids are of great technological importance and second, due to translational symmetry and ease in handling they constitute an accessible field both to experimental and theoretical investigations. In the following sections we will introduce the optical properties of solids and we will give the theoretical framework that describes the interaction of light with matter.

2.1.1   Maxwell equations

When describing steady-state problems in electricity and magnetism the electric and the magnetic fields can be treated as independent. However, when considering time-dependent problems we realize that time-varying electric fields give rise to magnetic fields and vice-versa. Then we must talk about electromagnetic fields. Light consists of time-varying electric and magnetic fields, therefore we need to describe it as an electromagnetic field. For this purpose we need to introduce Maxwell's equations which describe the behavior of electromagnetic fields in vacuum or inside matter. For the scope of this thesis we prefer to present the equations that describe electromagnetic fields in the presence of matter [3]:

$$\nabla \times \mathbf{E} \;=\; -\frac{\partial \mathbf{B}}{\partial t} \tag{2.1}$$

$$\nabla \times \mathbf{H} \;=\; \frac{\partial \mathbf{D}}{\partial t} + \mathbf{J} \tag{2.2}$$

$$\nabla \cdot \mathbf{D} \;=\; \rho \tag{2.3}$$

$$\nabla \cdot \mathbf{B} \;=\; 0. \tag{2.4}$$

In the above equations $\mathbf{E}(\mathbf{r}, t)$ is the electric field, $\mathbf{B}(\mathbf{r}, t)$ is the magnetic induction, $\mathbf{D}(\mathbf{r}, t)$ is the electric displacement, $\mathbf{H}(\mathbf{r}, t)$ is the magnetic field, $\rho(\mathbf{r}, t)$ is the free charge density, and $\mathbf{J}(\mathbf{r}, t)$ is the free current density. In most materials, where the electric quadrupole and higher moment densities are negligible [3], the macroscopic field quantities $\mathbf{D}$ and $\mathbf{H}$ are given by:

$$\mathbf{D} = \epsilon_0 \mathbf{E} + \mathbf{P} \tag{2.5}$$

$$\mathbf{B} = \frac{1}{\mu_0} \mathbf{H} - \mathbf{M}. \tag{2.6}$$

Here, $\mathbf{P}$ and $\mathbf{M}$ are the electric polarization and magnetization of the medium, respectively, while $\epsilon_0 = 8.854 \times 10^{-12}$ F/m is the electric permittivity of free space and $\mu_0 = 4\pi \times 10^{-7}$ N/A^2 is the magnetic permeability of free space.

In order to solve Maxwell's equations one must know the constitutive relations between $\mathbf{D}$, $\mathbf{H}$ and $\mathbf{E}$, $\mathbf{B}$. For isotropic materials, these equations are taken as:

$$\mathbf{D} = \epsilon_0 \epsilon \mathbf{E} \tag{2.7}$$

$$\mathbf{B} = \mu_0 \mu \mathbf{H} \tag{2.8}$$

$$\mathbf{J} = \sigma \mathbf{E}. \tag{2.9}$$

Equation 2.9 is the generalized Ohm's law and σ is the electrical conductivity of the material. In Eq. 2.8 $\mu_0 \mu$ is the magnetic permeability of the medium, while μ is called the relative magnetic permeability because it is defined as the ratio of the magnetic permeability of a substance to the magnetic permeability of free space, μ_0. Diamagnetic materials, which consist of atoms with no net angular momentum, have $\mu < 1$, while paramagnetic materials, which consist of atomic units with unpaired electrons thus having a net angular

momentum, have $\mu > 1$. In both cases, however, μ is almost equal to 1 for most materials and this is the convention we will follow in the rest of this thesis. Ferromagnetic materials are paramagnetic but with drastically different behavior due to atomic interactions. Below the Curie temperature ferromagnetic substances show spontaneous magnetization, $\mathbf{M}$. The application of an external field leads to saturation of the bulk magnetization, while removal of the field leaves a permanent magnetization. For ferromagnetic materials Eq. 2.8 does not hold anymore and a nonlinear functional relationship must be used:

$$\mathbf{B} = \mathbf{F}(\mathbf{H}). \tag{2.10}$$

In Eq. 2.7 $\epsilon_0 \epsilon$ is the electric permittivity of the material and ϵ is the dielectric function. By definition the dielectric function is a dimensionless quantity. In most textbooks ϵ is called dielectric constant but we prefer the term dielectric function because it is a function of the frequency of the electromagnetic field incident on the medium. Because in most materials $\mu = 1$ as we mentioned above, the dielectric function is the most important property when studying the optical response of matter. Knowing the dielectric function one can infer a wealth of information about the material such as whether it is a metal or a semiconductor, how it conducts electricity, or how it reflects and absorbs optical radiation, to name a few examples. To illustrate how much the dielectric function depends on the frequency of the applied field we can consider some known dielectric function values[1]. At low frequencies ($\nu \leq 10^6$ Hz) where all charges, regardless of their inertia, respond to applied fields, solids have dielectric functions in the range of 2-20. Distilled water has a much higher dielectric function, $\epsilon = 88$ at 0° C. At optical frequencies ($\nu \approx 10^{15}$ Hz) where only the electrons can respond significantly, the dielectric function of solids is in the range of 2-3.

---

[1] As we will show later the dielectric function is a complex quantity. The aforementioned values correspond to the real part and are valid only away from resonances, meaning away from frequencies for which the material is particularly absorptive. The purpose of mentioning these values is only for a qualitative understanding of the frequency variation of the dielectric function.

Water has $\epsilon \approx 1.77 - 1.8$ over the visible range independent of temperature. When an electric field is applied to an isotropic material the induced polarization $\mathbf{P}$ is parallel to the field $\mathbf{E}$:

$$\mathbf{P} = \epsilon_0 \chi_e \mathbf{E}, \tag{2.11}$$

where χ_e is called the electric susceptibility of the medium. Combining Eqs. 2.5, 2.11, and 2.7 we obtain

$$\epsilon = 1 + \chi_e. \tag{2.12}$$

The presence of the dielectric function in Maxwell's equations indicates that the electric fields inside the matter are reduced by a factor $1/\epsilon$ when compared to the free space value. This reduction is due to the polarization of the atoms inside the material that produces fields in opposition to the external fields.

As we already mentioned the dielectric function is a very important intrinsic property of a material, and it is sufficient to describe the optical behavior of the medium under study. Due to the increased importance of the dielectric function we will devote the next section in deriving analytical expressions for the dielectric function of different types of materials and we will highlight the two major material categories from the dielectric perspective: metals and semiconductors.[2]

2.1.2 The dielectric function

As we already discussed the dielectric function is a quantity that depends on the frequency of the applied field. In this work we are primarily concerned with optical

---

[2]The most accurate distinction is the one between metals and insulators. In essence semiconductors are a subset of insulators but due to their increased technological importance they attract disproportional attention.

frequencies ($\nu \approx 10^{15}$ Hz) for which only the electrons have small enough inertia to respond to the time-varying electromagnetic fields. Therefore, the behavior of the dielectric function depends on the electronic properties of the material.

In semiconductors under equilibrium, valence electrons are localized between the ions forming the covalent bonds. In order to model the dielectric function of a semiconductor, that is the response of the electrons of the medium to an externally applied electric field, we need to consider a bound charge e of mass m which acts under the influence of a restoring force [4]

$$\mathbf{F} = -m\omega_0^2 \mathbf{x}, \tag{2.13}$$

where ω_0 is the natural frequency of the charge about the equilibrium position and $\mathbf{x}$ is the displacement of the charge away from equilibrium. When we apply an external electric field $\mathbf{E}(\mathbf{x}, t)$, the equation of motion for the charge becomes:

$$m[\ddot{\mathbf{x}} + \gamma\dot{\mathbf{x}} + \omega_0^2 \mathbf{x}] = -e\mathbf{E}(\mathbf{x}, t) \tag{2.14}$$

where γ is a phenomenological damping constant. In order to proceed we will follow the simplifying assumption that the amplitude of oscillation of the charge is small. This allows us to neglect the space dependence of the electric field and to use the value of the field at the average position of the charge. In the case of a harmonically varying electric field with frequency ω we have $E(t) = Ee^{-i\omega t}$, where for simplicity we treat the problem in one dimension. In this case we will try a solution of the form $x(t) = Ce^{-i\omega t}$. By substitution in Eq. 2.14 we obtain:

$$x(t) = \frac{e}{m} \frac{Ee^{-i\omega t}}{\omega_0^2 - \omega^2 - i\omega\gamma}. \tag{2.15}$$

In a solid it is more realistic to consider N charges per unit volume. Then the induced polarization in the medium becomes $P = Nex(t)$. From Eqs. 2.11 and 2.15 we obtain:

$$\chi_e = \frac{Ne^2}{\epsilon_0 m} \frac{1}{\omega_0^2 - \omega^2 - i\omega\gamma}. \tag{2.16}$$

In reality it is better to assume that not all the electrons in the solid have the same binding frequency ω_0. We can consider that f_i electrons have binding frequency ω_i and damping constant γ_i. Then, with the aid of Eq. 2.12, we obtain the Lorentz model for the dielectric function,

$$\epsilon(\omega) = 1 + \frac{Ne^2}{\epsilon_0 m} \sum_i \frac{f_i}{\omega_i^2 - \omega^2 - i\omega\gamma_i}. \tag{2.17}$$

The dielectric function is a complex quantity. From Eq. 2.17 the real and imaginary parts read:

$$\mathrm{Re}[\epsilon(\omega)] = 1 + \frac{Ne^2}{\epsilon_0 m} \frac{\omega_0^2 - \omega^2}{(\omega_0^2 - \omega^2)^2 + \omega^2\gamma^2} \tag{2.18}$$

$$\mathrm{Im}[\epsilon(\omega)] = \frac{Ne^2}{\epsilon_0 m} \frac{\omega\gamma}{(\omega_0^2 - \omega^2)^2 + \omega^2\gamma^2}. \tag{2.19}$$

In Figure 2.1 we plot the real and the imaginary part of a dielectric function derived by the Lorentz model around a resonance $\omega_0 = 1$. When the frequency of the applied electric field, ω, approaches the binding frequency of the electrons in the material, ω_0, the imaginary part of the dielectric function peaks, while the real part presents a characteristic wiggle. Because of this dramatic behavior of the dielectric function around a binding frequency, these frequencies are also called resonant frequencies and they are characteristic of the material. In the resonant frequencies there is strong absorption of the external field by the medium.
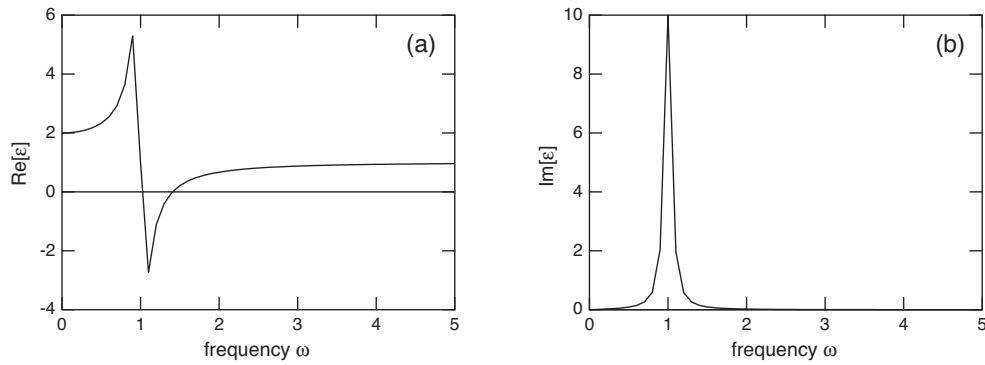
Figure 2.1: (a) Real and (b) Imaginary part of a Lorentz dielectric function with one resonance.

As we see in Figure 2.1(b) the imaginary part of the dielectric function is almost zero everywhere except near the resonant frequency, so for most frequencies the dielectric function is real. For most frequencies $Re[\epsilon]$ increases with increasing frequency and only around a resonance it decreases, as we see in Figure 2.1(a). In the case where $Re[\epsilon]$ increases with frequency, and this is the case most often, we say that we have normal dispersion while in the case where $Re[\epsilon]$ decreases with frequency we say that we have anomalous dispersion, and this is the case where very interesting effects like soliton formation occur [5].

In metals the case is quite different. The valence electrons are not localized in covalent bonds as in semiconductors, but they are delocalized and they are free to roam around the crystalline solid forming a "gas" of electrons. In order to derive an expression of the dielectric function of a metal in the range of optical frequencies we need to consider the response of a free electron to an applied electric field [6]. According to the Drude model, which is the simplest model to describe the behavior of free electrons in a metal, the equation of motion of a free electron in an electron "gas" under the influence of an external electric field is

$$\dot{\mathbf{p}} + \frac{\mathbf{p}}{\tau} = -e\mathbf{E}. \tag{2.20}$$

Here, τ is the average time that lapses before an electron picked at random suffers a collision and is is also known as the mean free time or relaxation time. From the definition of the relaxation time follows the definition of the mean free path of an electron, $l = v_0\tau$, where v_0 is the average electronic speed in the medium. The mean free path is the average distance an electron travels in a metal between two collisions. If we consider a harmonic field, $E(t) = Ee^{-i\omega t}$ and we simplify the problem to one dimension then we seek a steady-state solution of the form $p(t) = Ce^{-i\omega t}$. By substitution in Eq. 2.20 we obtain

$$p(t) = \frac{-eEe^{-i\omega t}}{1/\tau - i\omega}. \tag{2.21}$$

If we assume N electrons per unit volume in the metal, the current density is $J = -Nep/m$. From this definition and using Eq. 2.9 we obtain for the electrical conductivity of a metal

$$\sigma(\omega) = \frac{Ne^2\tau}{m} \frac{1}{1 - i\omega\tau}. \tag{2.22}$$

At zero frequency this quantity is known as the DC conductivity of a metal, $\sigma_0 = \frac{Ne^2\tau}{m}$. In the above derivation of the conductivity we assumed that the applied field and the current density do not exhibit spatial variation, *i.e.* we assumed they are independent of $\mathbf{x}$. Essentially we used the value of the field at the average position of the electron as a uniform value. We applied the same simplification above, when deriving the Lorentz dielectric function, going from Eq. 2.14 to Eq. 2.15. In the case of the Lorentz model, where we discussed bound charges, we were able to make this assumption because we considered small amplitude oscillations. The Drude model, which assumes free electrons does not use

the same assumption in order to justify the use of average values for the electric field. However, there is another reason why this simplification holds. The current density at one point in space, $\mathbf{x}$, depends on the interaction of the electric field with the electron located at $\mathbf{x}$ since the last collision of this particle. However for most metals the distance of the location of the last collision from $\mathbf{x}$ is no more than a few mean free paths. Therefore if the field does not vary much over distances on the order of the electronic mean free path we may use the average value of the field at $\mathbf{x}$ as a uniform value. For visible light, the wavelength is large compared to the mean free path and the approximation holds.

Once we know the conductivity we can calculate the dielectric function from [6]:

$$\epsilon(\omega) = 1 + \frac{i\sigma}{\epsilon_0 \omega}. \tag{2.23}$$

From Eqs. 2.22 and 2.23 we obtain an analytic expression for the dielectric function according to the Drude model:

$$\epsilon(\omega) = 1 + \frac{Ne^2}{\epsilon_0 m} \frac{i\tau}{\omega(1 - i\omega\tau)}. \tag{2.24}$$

The quantity $\omega_p^2 = \frac{Ne^2}{\epsilon_0 m}$ is also known as the plasma frequency. The real and imaginary part of the Drude dielectric function are:

$$\text{Re}[\epsilon(\omega)] = 1 - \frac{\omega_p^2 \tau^2}{1 + \omega^2 \tau^2} \tag{2.25}$$

$$\text{Im}[\epsilon(\omega)] = \frac{\omega_p^2 \tau}{\omega(1 + \omega^2 \tau^2)}. \tag{2.26}$$

Note that the Drude dielectric function, Eq. 2.24, can be derived from the Lorentz dielectric function, Eq. 2.17, setting $\omega_i = 0$ and $\gamma = 1/\tau$. Both expressions arise from the classical equation of motion of a charged particle inside an electric field and the difference is the existence or not of a restoring force.

In Figure 2.2 we plot the real and the imaginary part of a dielectric function derived by the Drude model. The most characteristic features of a Drude dielectric function are the negative real part and the diverging imaginary part as the frequency approaches zero.
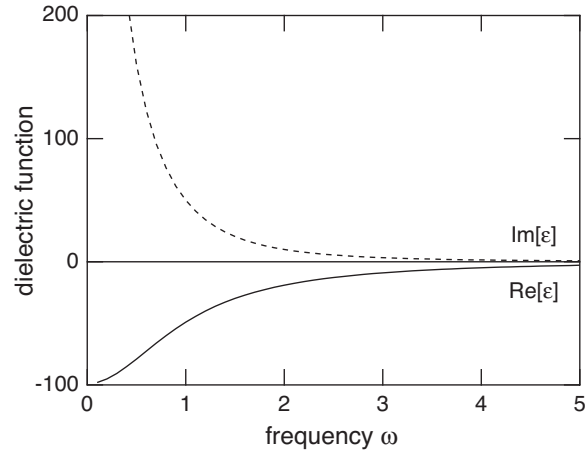
Figure 2.2: Real (solid line) and imaginary (dashed line) part of a Drude dielectric function.

In reality most materials have dielectric functions with contributions both from free and bound electrons. Therefore it is not rare to create a model that combines both Lorentz and Drude terms in order to explain successfully the optical properties of a solid. However, in semiconductors the contributions from bound electrons (interband contributions) dominate the picture while in metals the shape of the dielectric function is more Drude-like with small interband features.

In Figure 2.3 we plot the dielectric functions of GaAs and Cu. GaAs, which is a semiconductor, displays two resonances in the frequency window of the figure and can be fitted successfully with the Lorentz model using two oscillators with resonant frequencies at 3 and 4.5 eV [7]. Cu, on the other hand, is a metal and its dielectric function strongly resembles the Drude dielectric function. We can see in Figure 2.3(b) the negative real part and the diverging imaginary part. The most prominent deviation from the Drude shape is

a feature near 2 eV which arises from the interband transition of d-band electrons into the conduction band [6]. This feature is responsible for the reddish color of Cu.
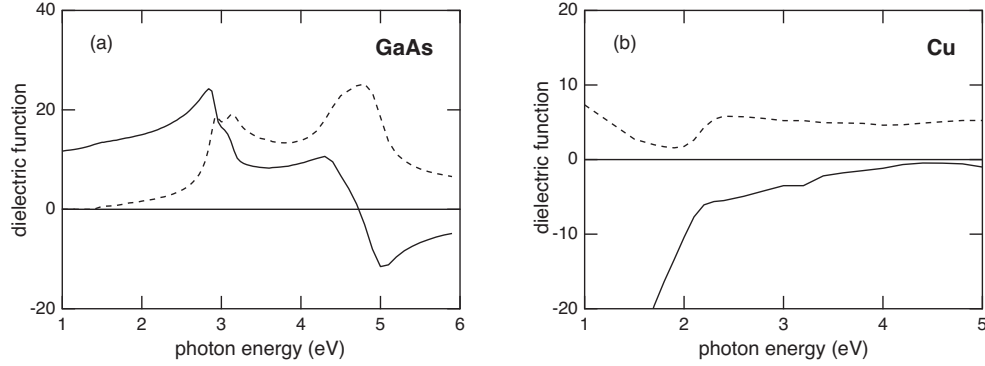
Figure 2.3: Real (solid line) and imaginary (dashed line) part of the dielectric function of (a) GaAs and (b) Cu.

Electronic effects are not the only contributions to the dielectric function of a medium. In the next section we will examine additional contributions to the optical properties of solids.

2.1.3   Relationship between dielectric function and band structure

In the previous section we derived two models for the dielectric function of a material based on the response of the valence electrons in the presence of an electric field. It has been shown in time-resolved experiments that a short laser pulse interacts primarily with the valence electrons because they have much smaller inertia than the ions [8–10]. When the laser excitation is sufficiently weak, the excited electrons will eventually relax back to the ground state and the material will reach equilibrium with little lattice disorder. In this case the optical response of the material is dominated by the excited electronic population and the discussion of section 2.1.2 is applicable. When the laser excitation is strong, the lattice will deform significantly due to the electronic excitation and the optical

properties of the material will be modified not only by the excited electronic population but also by the lattice deformation. The most striking example is how the optical properties of a surface change after melting or ablation, in many cases even to the naked eye [11–14]. Furthermore, the optical properties of solids are known to change between single-crystal and pollycrystalline samples or between films of different thicknesses and grain size [15,16].

Lattice and electronic effects are taken into account when deriving the band structure of a medium. By knowing the band structure of a material one can make valid predictions about the dielectric function and it is often the case that band structure calculations aim at increasing the understanding of the optical properties of a given medium. The fact that semiconductors and metals are best described with different models for the dielectric function is also manifested in the band structure. In semiconductors there is a forbidden energy range, while in metals all energy eigenvalues are accessible by the electronic states. In semiconductors the valence bands are completely filled and the conduction bands are completely empty. Upon photoexcitation the electrons can follow only one path that will allow them to accommodate the excess energy they absorb from the incident electric field: they are promoted from a filled valence band to an empty conduction band. This transition gives rise to an interband contribution to the dielectric function which is best modeled by the Lorentz model. In this case the resonant frequency in the Lorentz description corresponds to the energy difference between the two states participating in the electronic transition through the relation $E = \hbar\omega$. Figure 2.4 shows the band structure and dielectric function of GaAs.

As we discussed earlier, the dielectric function of GaAs has two resonances centered at 3 and 4.5 eV. Looking at the band structure it is obvious that the resonances arise from transitions around the L and X points of the first Brillouin zone [6]. The reason why these transitions dominate the optical spectrum of GaAs is that around these points the
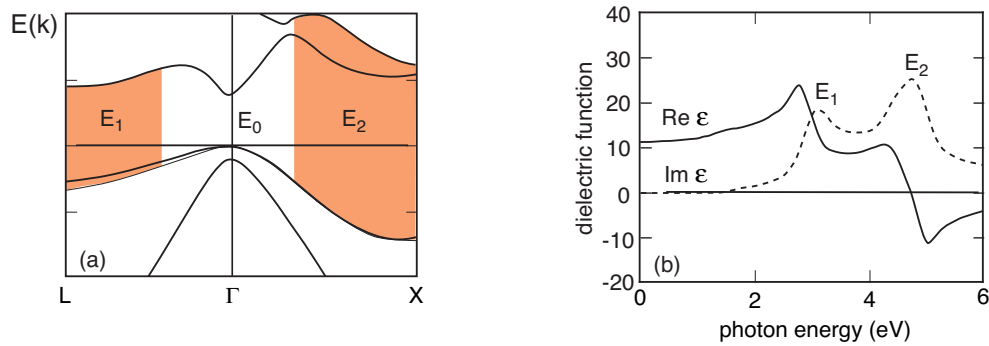
Figure 2.4: (a) Band structure and (b) Dielectric function of GaAs. The optical resonances centered at energies E_1 and E_2 arise from electronic transitions around the L and X points in the band structure (shaded regions).

valence and conduction bands are nearly parallel, thus increasing the probability of such transitions [17, 18].

In metals the situation is different. The highest occupied band is usually only half-filled and this offers the possibility of intraband electronic transitions occurring upon photoexcitation, that is electrons reaching a final state, the energy and wavenumber of which belong to the same band as the initial state. Intraband transitions are best described by the Drude model which indeed is a good first approximation for the dielectric function of many metals. However, interband transitions are also possible, either from the highest, partially occupied band or from lower-energy, filled bands to higher unoccupied bands. Figure 2.5 shows the band structure and dielectric function of Cu.

Cu $(3d^{10}4s^1)$ has all bands below the 4s band completely filled and the 4s band half filled. The five different 3d bands are the highest bands to be filled and they fall within a narrow energy range, denoted in Figure 2.5(a) by the shaded region. Interband transitions between the d bands and the 4s band are possible (little arrows), giving rise to the interband feature in the dielectric function of Cu around 2 eV. The big arrows in 2.5(a) indicate another possible interband electronic transition, this time from the partially
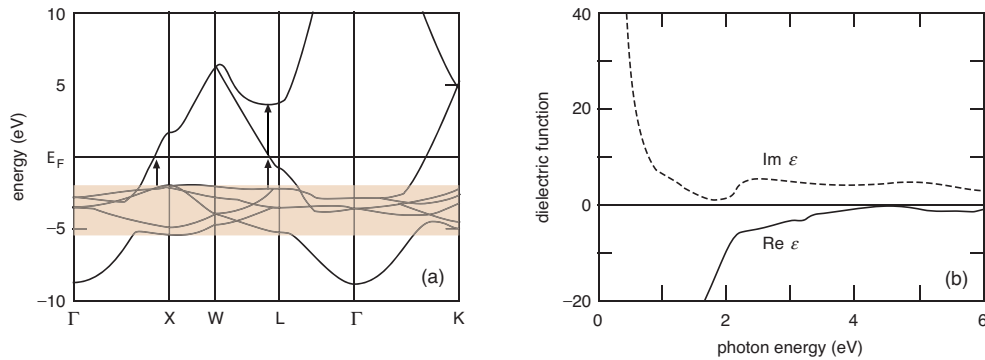
Figure 2.5: (a) Band structure and (b) Dielectric function of Cu. The interband feature of the dielectric function around 2 eV arises from electronic transitions between the d-band (shaded region in (a)) and the conduction band.

occupied 4s band to a higher empty conduction band.

It is clear at this point that the shape and occupation numbers of the band structure is associated with the optical properties of solids. In experiments where electrons and lattice are strongly driven by the excitation field, the observed optical properties change dramatically. With the appropriate framework these optical changes can be linked to changes in the band structure and eventually to changes in the crystal itself. The band structure is a path connecting the optical properties of a material to the electronic and lattice configuration in the crystal. Its importance in connecting optical data to physical processes cannot be easily overestimated.

2.1.4 Light at an interface

So far we have described the behavior of light inside bulk matter. However, in most practical cases light travels through multiple objects, for example it hits the front surface of a mirror when traveling through air, or it penetrates the lens of someone's glasses before reaching the human eye. Therefore if we want to have a complete description of light-matter interactions we must describe the behavior of light at an interface between two

different materials. For this purpose we must consider light as a wave. The easiest way to obtain a wave equation for light is by rewriting Maxwell's equations 2.1 – 2.4 in a space free of net charges and currents for simplicity. With the aid of the constitutive relations 2.7 and 2.8 Maxwell's equations become:

$$\nabla \times \mathbf{E} = -\frac{\partial \mathbf{B}}{\partial t} \tag{2.27}$$

$$\nabla \times \mathbf{B} = \epsilon\epsilon_0\mu\mu_0\frac{\partial \mathbf{E}}{\partial t} \tag{2.28}$$

$$\nabla \cdot \mathbf{E} = 0 \tag{2.29}$$

$$\nabla \cdot \mathbf{B} = 0. \tag{2.30}$$

Taking $\nabla\times$ the first equation and substituting the second and the third gives the wave equation for $\mathbf{E}$, while taking $\nabla\times$ the second equation and substituting the first and the fourth gives the wave equation for $\mathbf{B}$:

$$\nabla^2\mathbf{E} - \epsilon\epsilon_0\mu\mu_0\frac{\partial^2 \mathbf{E}}{\partial t^2} = 0 \tag{2.31}$$

$$\nabla^2\mathbf{B} - \epsilon\epsilon_0\mu\mu_0\frac{\partial^2 \mathbf{B}}{\partial t^2} = 0. \tag{2.32}$$

The solutions to the above wave equations are the usual solutions of a traveling wave with velocity

$$v = \frac{1}{\sqrt{\epsilon\epsilon_0\mu\mu_0}} = \frac{c}{n}. \tag{2.33}$$

The above equation indicates that the value of the speed of light in a material is reduced from the value of the speed of light in vacuum, $c = \frac{1}{\sqrt{\epsilon_0\mu_0}}$, by a factor $n = \sqrt{\epsilon\mu}$, also known as the index of refraction of the material. In most materials $\mu = 1$, as we discussed

in section 2.1.1, so the index of refraction is related to the dielectric function of a material by

$$n(\omega) = \sqrt{\epsilon(\omega)}. \tag{2.34}$$

Because the dielectric function is a complex quantity the index of refraction is also a complex quantity,

$$n = \eta + i\kappa. \tag{2.35}$$

The real part of the index of refraction, η, is also called index of refraction and the imaginary part, κ, is called the extinction coefficient for reasons that will become obvious later. The real and imaginary parts of the dielectric function are related to the real and imaginary parts of the index of refraction by

$$\text{Re}[\epsilon] = \eta^2 - \kappa^2 \tag{2.36}$$

$$\text{Im}[\epsilon] = 2\eta\kappa. \tag{2.37}$$

Conversely,

$$\eta = \sqrt{\frac{1}{2}\left(\text{Re}[\epsilon] + \sqrt{\text{Re}[\epsilon]^2 + \text{Im}[\epsilon]^2}\right)} \tag{2.38}$$

$$\kappa = \frac{\text{Im}[\epsilon]}{\sqrt{2\left(\text{Re}[\epsilon] + \sqrt{\text{Re}[\epsilon]^2 + \text{Im}[\epsilon]^2}\right)}}. \tag{2.39}$$

In order to understand the physical meaning of the refractive index and the extinction coefficient we need to consider one possible solution to the wave equation 2.31:

$$E(x,t) = E_0 e^{i(kx - \omega t)}. \tag{2.40}$$

Equation 2.40 describes a wave traveling in the x-direction. In the simplest case E_0 is a constant which does not depend on position, or time, or frequency and the above equation describes a monochromatic wave. The wave number k and the frequency ω must satisfy the condition

$$\frac{\omega}{k} = v = \frac{1}{\sqrt{\epsilon \epsilon_0 \mu \mu_0}} = \frac{c}{n}, \tag{2.41}$$

therefore Eq. 2.40 can be rewritten as

$$E(x,t) = E_0 e^{i(n\frac{\omega}{c}x - \omega t)} = E_0 e^{-\kappa \frac{\omega}{c} x} e^{i(\eta \frac{\omega}{c} x - \omega t)}, \tag{2.42}$$

where we made use of Eq. 2.35. Now the physical meaning of the index of refraction, η, and the extinction coefficient, κ, becomes transparent. The speed of light in the medium is determined by η in the way predicted by Eq. 2.33: $v = c/\eta$. The existence of an imaginary component, κ, leads to exponential decay of the electric field in the medium due to absorption. It is easier to observe the absorption of the experimentally measurable intensity of light, which depends on the square amplitude of the electric field. Therefore, according to Eq. 2.42, the intensity inside the medium varies as

$$I(x) = I(0) e^{-2\kappa \frac{\omega}{c} x}. \tag{2.43}$$

Based on the intensity decay we define the absorption depth, or skin depth, or penetration depth, as the distance l over which the intensity drops to $1/e$ of its initial value $I(0)$. The inverse of the absorption depth is the absorption coefficient

$$\alpha = \frac{2\kappa\omega}{c} = \frac{4\pi\kappa}{\lambda_0}, \tag{2.44}$$

where λ_0 is the wavelength of the electric field in vacuum.

Now that we have established the description of light as a wave it is easy to imagine what happens when an electromagnetic field meets an interface between two materials: part of it reflects off the boundary and part of it transmits into the second material. These processes are presented pictorially in Figure 2.6.
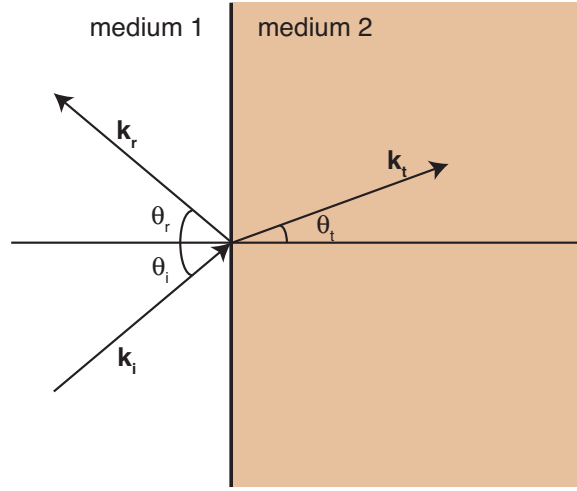
Figure 2.6: Reflection and transmission at interface. $\mathbf{k_i}$, $\mathbf{k_r}$, and $\mathbf{k_t}$ are the wave vectors of the incident, reflected, and transmitted field, respectively. θ_i, θ_r, and θ_t are the angles of the incident, reflected and transmitted beam propagation direction with respect to the surface normal, respectively.

In the figure we plot an electric field with wave vector $\mathbf{k_i}$ incident on an interface between two materials at an angle θ_i with respect to the surface normal. Part of the field reflects at an angle θ_r and propagates into medium 1 with wave vector $\mathbf{k_r}$ and part of it transmits into medium 2 at an angle θ_t and propagates with wave vector $\mathbf{k_t}$. Applying the appropriate boundary conditions [19] that determine the behavior of an electromagnetic field at an interface, we obtain the law of reflection

$$\theta_i = \theta_r \tag{2.45}$$

and Snell's law

$$n_i \sin\theta_i = n_t \sin\theta_t, \tag{2.46}$$

where $n_i = n_1$ is the index of refraction of medium 1, in which the incident beam propagates, while $n_t = n_2$ is the index of refraction of medium 2, in which the transmitted beam propagates.

Application of the boundary conditions provides us not only with laws about the geometry of the reflected and transmitted beams but also allows us to determine the fraction of the incident power that will be reflected and transmitted. These fractions depend on the angle of incidence, the properties of the two media, the frequency and polarization of the incident field. The polarization of the field is defined with respect to the plane of incidence. The plane of incidence is the plane defined by the direction of propagation of the incident field and the surface normal. For example, in Figure 2.6 the plane of incidence is the plane of the paper. An electric field is called p-polarized if the field vector (not shown in Figure 2.6) is parallel to the plane of incidence and s-polarized if the field vector is perpendicular to the plane of incidence. The equations that determine the fraction of the incident field to be reflected and transmitted at an interface are called the Fresnel equations and for p-polarized fields read [3]

$$r_p = \frac{E_r}{E_i} = \frac{\frac{\mu_1}{\mu_2} n_2^2 \cos\theta - n_1 \sqrt{n_2^2 - n_1^2 \sin^2\theta}}{\frac{\mu_1}{\mu_2} n_2^2 \cos\theta + n_1 \sqrt{n_2^2 - n_1^2 \sin^2\theta}} \tag{2.47}$$

$$t_p = \frac{E_t}{E_i} = \frac{2 n_1 n_2 \cos\theta}{\frac{\mu_1}{\mu_2} n_2^2 \cos\theta + n_1 \sqrt{n_2^2 - n_1^2 \sin^2\theta}}, \tag{2.48}$$

where $\theta = \theta_i$ is the angle of the incident beam. The above equations assume that the beam is incident from medium 1 to medium 2. For s-polarized fields, Fresnel equations become

$$r_s = \frac{E_r}{E_i} = \frac{n_1 \cos\theta - \frac{\mu_1}{\mu_2}\sqrt{n_2^2 - n_1^2 \sin^2\theta}}{n_1 \cos\theta + \frac{\mu_1}{\mu_2}\sqrt{n_2^2 - n_1^2 \sin^2\theta}} \tag{2.49}$$

$$t_s = \frac{E_t}{E_i} = \frac{2n_1 \cos\theta}{n_1 \cos\theta + \frac{\mu_1}{\mu_2}\sqrt{n_2^2 - n_1^2 \sin^2\theta}}. \tag{2.50}$$

The quantities r and t are complex numbers because the index of refraction is complex. More useful and experimentally measurable are the reflectivity R and transmissivity T, which measure the fraction of the power of the incident field to be reflected and refracted. Analytical expressions for these quantities read [20]

$$R = \frac{I_r}{I_i} = |r|^2 \tag{2.51}$$

$$T = \frac{I_t}{I_i} = \frac{n_2 \cos\theta_2}{n_1 \cos\theta_1}|t|^2. \tag{2.52}$$

In most materials $\mu = 1$ and the Fresnel equations can be simplified. Furthermore, in many practical applications medium 1 is air with $n = 1$ and medium 2 is the material under investigation with dielectric function ϵ. In this case the Fresnel equation take the much simpler form

$$r_p = \frac{\epsilon \cos\theta - \sqrt{\epsilon - \sin^2\theta}}{\epsilon \cos\theta + \sqrt{\epsilon - \sin^2\theta}} \tag{2.53}$$

$$t_p = \frac{2\sqrt{\epsilon}\cos\theta}{\epsilon \cos\theta + \sqrt{\epsilon - \sin^2\theta}} \tag{2.54}$$

$$r_s = \frac{\cos\theta - \sqrt{\epsilon - \sin^2\theta}}{\cos\theta + \sqrt{\epsilon - \sin^2\theta}} \tag{2.55}$$

$$t_s = \frac{2\cos\theta}{\cos\theta + \sqrt{\epsilon - \sin^2\theta}}. \tag{2.56}$$

Figure 2.7 shows the p and s reflectivity of Al at 800 nm as a function of angle of incidence. We observe that while p-reflectivity reaches a minimum, s-reflectivity varies

monotonically with angle. This is a common behavior in all materials and it is a consequence of the functional form of the Fresnel equations. In many materials there is an angle where the *p*-reflectivity vanishes, the so called Brewster angle. In materials like Al, where the *p*-reflectivity does not entirely vanish, the angle of minimum is called pseudo-Brewster angle. The Brewster angle is given by

$$\theta_B = \tan^{-1} \frac{n_2}{n_1}. \tag{2.57}$$
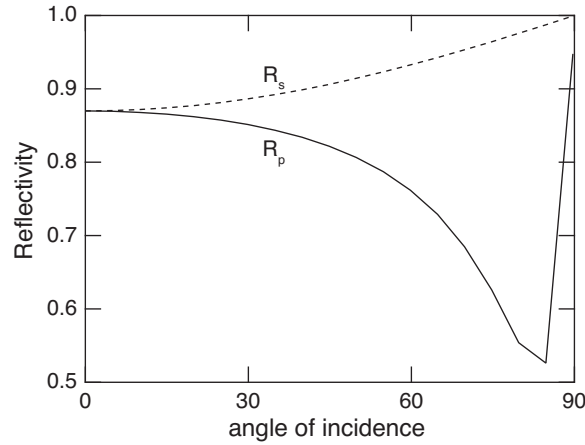
Figure 2.7: *p*- (solid line) and *s*- (dashed line) polarized reflectivity of aluminum at 800 nm as a function of angle of incidence.

Since most optical experiments are based either on reflection or transmission measurements the Fresnel equations are extremely useful for the study of the optical properties of materials. Furthermore, as we will discuss later, the Fresnel equations relate observable quantities, like reflectivity and transmissivity, to intrinsic optical properties of a material, like the dielectric function, and they are extremely useful in analyzing optical data to infer changes in the material structure and electronic configuration.

2.1.5   The Kramers-Kronig relations

As we mentioned above, the dielectric function is a complex quantity. However, the real and imaginary parts of the dielectric function are not independent variables. They are connected by the Kramers-Kronig relations [3]

$$\text{Re}[\epsilon(\omega)] \quad = \quad 1 + \frac{1}{\pi}\mathcal{P}\int_{-\infty}^{\infty}\frac{\text{Im}[\epsilon(\omega')]}{\omega'-\omega}\,\text{d}\omega' \tag{2.58}$$

$$\text{Im}[\epsilon(\omega)] \quad = \quad -\frac{1}{\pi}\mathcal{P}\int_{-\infty}^{\infty}\frac{\text{Re}[\epsilon(\omega')]-1}{\omega'-\omega}\,\text{d}\omega'. \tag{2.59}$$

According to the Kramers -Kronig relations, if we can determine the imaginary part of the dielectric function from absorption measurements then we can infer the real part. In reality, however, the measurement will have to extend over a very large range of frequencies because for the correct application of the Kramers-Kronig relations, knowledge over an infinite frequency interval is required. For this reason it is often the case that in practical applications people prefer to take more than one set of measurements in order to determine the real and imaginary parts of the dielectric function independently.

2.2   Laser-induced structural changes in solids

The dynamical properties of the electrons and the lattice in solids define many basic properties of these materials, such as conductivity, superconductivity, magnetism, linear and nonlinear optical characteristics. For this reason carrier dynamics and other transient electron behavior in bulk, single crystals or polycrystalline thin films are of fundamental importance. One way of inducing extreme nonequilibrium processes in the laboratory in order to study the resulting dynamics is by excitation with intense, ultrashort laser pulses. However, a comprehensive understanding of the relevant physics remains elusive due to

the extreme non-perturbative nature of strong-field laser interactions with valence and core states.

Previous studies have shown that large laser-induced changes in carrier occupation in metals and semiconductors can lead to substantial band structure renormalization and even to structural phase transitions [10, 21–25]. An ultrafast laser pulse, with a duration shorter than the excited electron energy-loss lifetime, can rapidly heat electrons to a very high temperature while leaving the lattice relatively cool since the heat capacity of the electrons is much smaller than that of the lattice. This transient two-temperature system tends to reach equilibrium within a few picoseconds via electron-phonon interactions as well as electron transport out of the excited region. In the perturbative low-intensity regime, the excited region reaches equilibrium with little disorder [26]. In the high-intensity regime, on the other hand, a plasma can be created and the plasma-related phenomena, such as hydrodynamic expansion or resonance absorption need to be taken into account [27–32]. For laser intensities slightly lower than the ones required for plasma formation, structural changes such as melting [22] and ablation [11, 12] take place and the material is permanently modified. Previous studies have shown a novel non-thermal melting mechanism in semiconductors [10, 33–39]. This non-thermal process is typically very fast, on the order of hundreds of femtoseconds, and occurs when the ions rapidly gain kinetic energy after the laser-induced electronic excitation and rearrange themselves in a liquid configuration before the lattice has enough time to thermalize.

In this thesis we are primarily concerned with the solid-to-liquid phase transition (melting). In the following sections we will highlight the differences between thermal and non-thermal melting in order to provide the appropriate background for the presentation of our experimental data on the solid-to-liquid phase transition in aluminum.

2.2.1 Laser-induced thermal melting in metals

The process of laser-induced thermal melting applies both to metals and semiconductors. We choose to illustrate the mechanism in the case of a metal in order to help the discussion of our study on aluminum that will be presented later.

Figure 2.8(a) shows the crystal of a metal, where the ions and core electrons occupy lattice cites and the valence electrons become detached and form the electron gas, or Fermi sea of electrons.

(a)   (b)

Figure 2.8: (a) The crystal of a metal. Circles: ions and core electrons. Shaded background: valence electron gas. (b) The Fermi-Dirac distribution at $T = 0$ K.

The valence electrons follow the Fermi-Dirac distribution, according to which, the probability $f(E)$ of one electron occupying a state with energy E is

$$f(E) = \frac{1}{e^{(E-\mu)/K_B T} + 1}. \tag{2.60}$$

We note that the probability depends on the temperature T of the electronic population which, under equilibrium, is the same as the temperature of the metal itself. The chemical potential, μ, is equal to the Fermi energy of the material, E_F, at $T = 0$ K

$$\lim_{T \to 0} \mu = E_F. \tag{2.61}$$

The Fermi energy is the energy of the highest-energy occupied one-electron level. Although strictly speaking the chemical potential equals the Fermi energy only at zero temperature, in the case of metals it remains very close to the Fermi energy at higher temperatures as well and it is often the case that the two quantities are used interchangeably. Figure 2.8(b) shows the energy distribution of the electrons in a metal at zero temperature according to the Fermi-Dirac description. All energy levels up to the Fermi energy are occupied with probability 1 and all levels above the Fermi energy are empty.

At room temperature the situation is slightly different. Figure 2.9(a) shows a schematic of a metal at $T = 300$ K where the electronic population is "hotter". Figure 2.9(b) shows how the Fermi-Dirac distribution evolves at a temperature above absolute zero. Due to thermal excitation the electrons closer to the Fermi energy gain kinetic energy and raise their total energy by about $K_B T$ and occupy energy levels above the Fermi energy, leaving some energy levels below the Fermi energy empty.
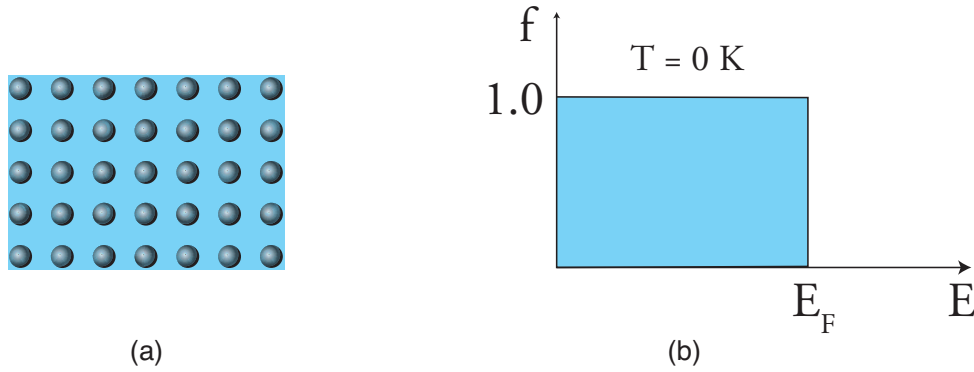

(a)   (b)
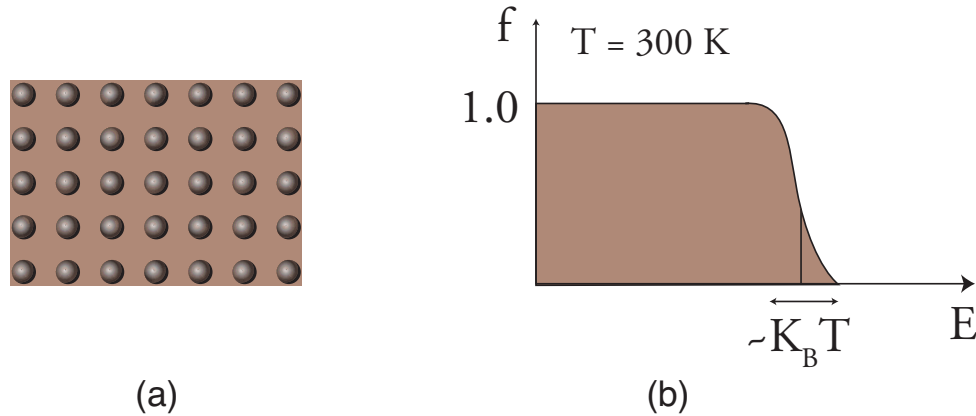
Figure 2.9: (a) The crystal of a metal. Circles: ions and core electrons. Shaded background: valence electron gas. (b) The Fermi-Dirac distribution at $T = 300$ K.

The situation changes drastically upon the arrival of a femtosecond laser pulse [26], as shown in Figure 2.10. The top panel shows the arrival of the laser pulse. We label this

instant as $\Delta t = 0$. Initially the laser pulse is absorbed by the valence electrons within a volume starting from the illuminated surface and reaching deeper into the bulk up to the penetration depth of the incident field. The absorption of the laser pulse changes the electronic energy distribution significantly. A fraction of the valence electrons of the metal absorb photons of energy $E = h\nu$ and occupy states above the Fermi energy, leaving empty states behind. At the top panel of Figure 2.10 we show the resulting energy distribution for the electrons right after photoexcitation, where for simplicity we assume only linear absorption, meaning that each electron absorbs only one photon and gains one quantum of energy. In reality under strong excitation conditions multiphoton absorption is also possible although with a much smaller probability than linear absorption. The energy distribution at $\Delta t = 0$ is not a Fermi-Dirac distribution. It is a non-equilibrium distribution and we cannot define a temperature for the electronic system at this point. The photoexcited electrons immediately engage themselves in two parallel processes. One process is ballistic excited electron transport into deeper parts of the crystal with velocities close to the Fermi velocity. For example, we mention that the Fermi velocity for gold is 1.4×10^6 m/s [6]. This process redistributes the absorbed laser energy deeper into the sample, increasing the photoexcited volume and decreasing the energy density stored in the material. The second process is electron-electron collisions which redistributes the energy of the photoexcited electrons among the entire electronic system and helps in establishing a thermal equilibrium among the electrons.

After tens or hundreds of femtoseconds, depending on the material and the excitation strength of the incident field, the situation evolves into what we show in the middle panel of Figure 2.10. The photoexcited depth now lies beyond the optical penetration depth, due to ballistic motion of electrons. The energy distribution of the electronic population inside the photoexcited region is again a Fermi-Dirac equilibrium distribution due to
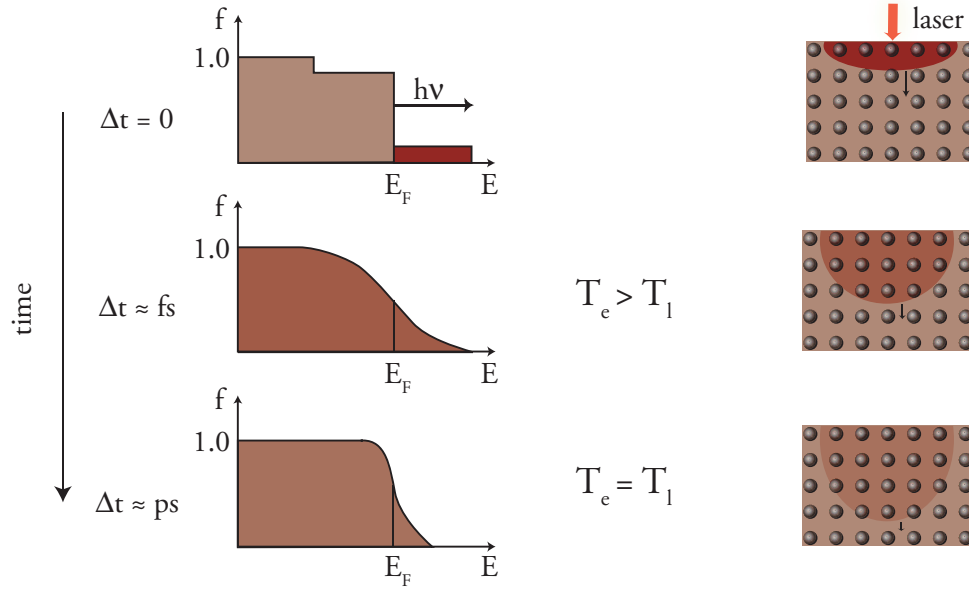
Figure 2.10: Top panel: an incident laser pulse is absorbed by electrons near the surface (right) and creates a non-equilibrium electronic distribution (left). Middle panel: Electrons reach a temperature T_e (left) and start thermal diffusion (right). Bottom panel: electrons and lattice reach a common temperature (left) and thermal conduction starts (right).

electron-electron collisions. However, the energy absorbed by the laser pulse has increased the temperature of the electrons and the spread of the distribution around the Fermi energy is wider than in room temperature. So far no energy has been transferred to the lattice.[3] Therefore at this point the electrons and the lattice are two systems with different temperatures. The electronic temperature, T_e, is much higher than the lattice temperature, T_l.

We can attempt an order of magnitude estimate of the electronic temperature based on the fact that the energy density stored in a thermal bath of electrons of temperature T_e is [26]

---

[3]In reallity, through electron-phonon scattering some energy has already been transferred to the lattice but it is negligible because in such a short time very few electron-phonon scattering events have occured.

$$Q = \frac{1}{2}C_e T_e, \tag{2.62}$$

where C_e is the constant-volume heat capacity, or specific heat, of the electrons. The heat capacity of electrons is proportional to their temperature, $C_e(T_e) = \gamma T_e$, and given that the absorbed energy density is the energy density deposited by the laser, Q_L, we can estimate the electronic temperature as

$$T_e^2 = \frac{2Q_L}{\gamma} = \frac{2}{\gamma}\frac{F_{abs}}{d}. \tag{2.63}$$

In the above equation we express the energy density in terms of the absorbed laser fluence, F_{abs}, which is given by the absorbed laser energy divided by the area of the incident beam. Dividing the absorbed fluence by the deposition depth, d, we obtain the absorbed energy density. The ballistic range for gold was found to be approximately 100 nm [40]. We will use this value as the deposition depth. For an absorbed fluence of 10 mJ/cm^2, which is a typical value for strongly driven photoexcitation experiments, and $\gamma = 71$ J/m^{3}K^2, which is the electronic specific heat for gold [41], we obtain $T_e = 5,300$ K. This is the maximum temperature reached by the electronic system, before coupling to the lattice takes place. At the same time the lattice's temperature is equal to room temperature, $T_l = 300$ K, since not enough time has lapsed for the energy deposited by the laser to be transferred to the lattice. Therefore the two systems, electrons and lattice, have dramatically different temperatures on the femtosecond time scale.

The two systems will now start reaching an equilibrium through electron-phonon collisions, which transfer energy from the hot electron bath to the cold lattice. At the same time the hot electrons start a diffusive motion deeper into the material due to the temperature gradient between the electrons in the photoexcited region and the electrons in the rest of the material. The diffusion speed in much slower than the ballistic motion.

After a few picoseconds these processes create the picture we show at the bottom panel of Figure 2.10. Now the electrons and lattice have one common temperature and energy transport to deeper parts of the material proceeds by lattice thermal diffusion. The speed of this process depends on the heat conductivity of the lattice. If the temperature of the lattice at this point is higher than the melting temperature of the material, melting occurs. This mechanism is called thermal melting and it is governed by picosecond time scales. The time scale is set by the electron-phonon coupling strength of the material because this is the mechanism through which energy is transferred to the lattice.

For a microscopic description of melting we need to think in terms of ionic displacements. Figure 2.11(a) shows the lattice of a metal during equilibration with the hot electrons. The phonons emitted through the electron-phonon coupling effects result in oscillations of the ions around their equilibrium positions. As more and more energy is transferred to the lattice the amplitude of the oscillations increases until the lattice becomes destabilized and the ions start wandering great distances resulting in melting of the solid, shown in Figure 2.11(b).

(a)   (b)
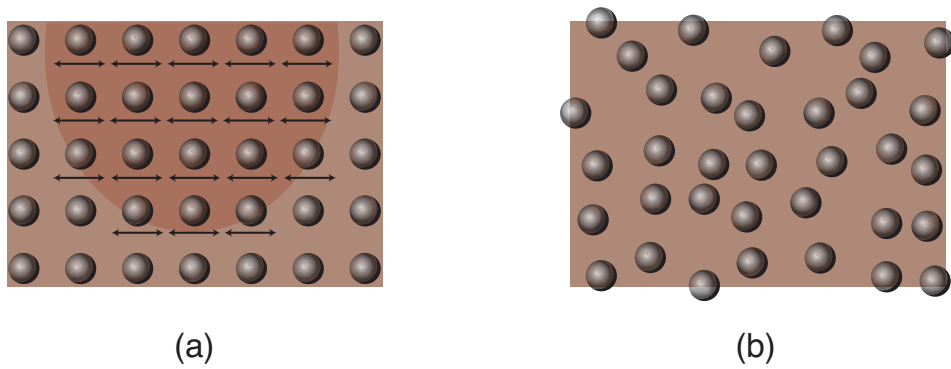
Figure 2.11: (a) Excitation of large amplitude oscillations through electron-phonon coupling in a photoexcited metal leads to loss of long-range order and melting (b).

In this section we provided a qualitative picture of thermal melting. A quantitative

description follows in the next section.

2.2.2 The two-temperature model

Once the electronic system of a photoexcited metal has reached equilibrium with a high temperature T_e, different than that of the lattice T_l, a quantitative description of the ensuing dynamics is given by the two-temperature model [42]

$$C_e(T_e)\frac{\partial T_e}{\partial t} = \frac{\partial}{\partial z}\left(K_e\frac{\partial T_e}{\partial z}\right) - g(T_e - T_l) + P(\mathbf{r}, t) \tag{2.64}$$

$$C_l\frac{\partial T_l}{\partial t} = g(T_e - T_l). \tag{2.65}$$

In the above equations $C_e = \gamma T_e$ is the electronic specific heat, K_e is the thermal conductivity of the electrons, g is the electron-phonon coupling constant, $P(\mathbf{r}, t)$ is the laser power density (given in W/m^3), and C_l is the lattice specific heat.

The two temperature model captures the physical processes we described in Section 2.2.1. The first equation denotes that the electrons gain energy from the absorbed laser energy, which helps raise their temperature, and then redistribute this energy through thermal diffusion and coupling to the lattice. The latter processes help decrease the electronic temperature. The second equation shows that the only way for the lattice to gain energy is through electron-phonon coupling.

The existence of two equilibrium systems with different temperatures inside the solid is a novelty of femtosecond science. With nanosecond and even picosecond laser pulses the duration of the laser pulse is comparable to the time scale of electron-lattice equilibration and therefore by the time the excitation pulse is gone the electrons and lattice are already in equilibrium with a common temperature. Only femtosecond pulses beat the electron-lattice equilibration time preparing the metal in this unusual state. The two-temperature model

was very successful in describing this new state of matter and its particular contribution was the inclusion of the electron-phonon coupling constant as the only source of communication between electrons and lattice.

Equations 2.64 – 2.65 are valid for bulk samples. By bulk we mean any sample with thickness greater than the ballistic range of the photoexcited electrons. If the sample thickness is smaller than the ballistic range then during the first femtoseconds after the arrival of the laser pulse, ballistic electrons are able to travel through the bulk of the metal reaching the back surface and to reflect towards the front surface. Multiple reflections result in homogeneous heating of the electronic population across the film thickness and the diffusion term in Eq. 2.64 disappears because there is no temperature gradient among the electrons.

Once we neglect the diffusion term in the two-temperature model, the equilibration between electrons and lattice speeds up, as shown in Figure 2.12. This Figure shows two-temperature model calculations which predict the evolution of electronic and lattice temperatures following laser excitation in the case of a 20-nm thick Au film (solid lines) and a bulk Au sample (dashed lines). We observe from the Figure that the bulk sample reaches electron-lattice equilibrium much faster than the thin film.

Another consequence of trapping all the laser energy inside a very thin film is that we achieve higher energy densities stored in the thin film compared to a bulk sample where energy would diffuse deep into the material and the energy density would drop. As a result, very thin films have lower damage thresholds than bulk samples of the same material, meaning the minimum incident laser energy required to create damage is lower for thin films.

The two-temperature model is a quantitative description of thermal dynamics that follow photoexcitation of a metal. The mechanism proposed is called thermal because
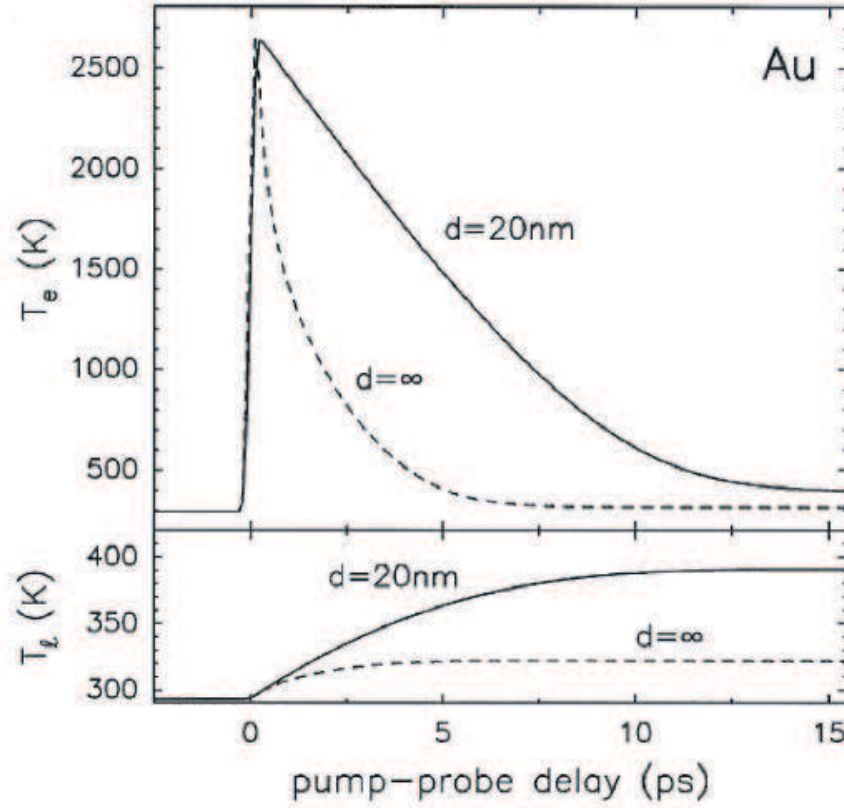
Figure 2.12: Solution of the two-temperature model for the case of phototexcited bulk Au (dashed lines) and a 20-nm thick Au film (solid lines). After Ref. [26].

we assume that at every instant the electrons and lattice are systems with well defined temperature. As we mentioned above, a state of matter where the electrons and the lattice have different temperatures is accessible only by femtosecond lasers. However this is not the only exotic result obtained with femtosecond lasers. Non-thermal melting is a process observed and initiated only when femtosecond lasers became available. In the next section we will discuss non-thermal melting and we will highlight its differences compared to thermal melting.

2.2.3 Laser-induced non-thermal melting in semiconductors

The effect of non-thermal melting was observed in a series of experiments in semiconductors where photoexcitation was provided by a femtosecond pulse. The effect has been investigated rigorously both with optical pump-probe experiments [10, 33–36, 43, 44] and with x-ray diffraction measurements [37–39] and it is now well understood.

In semiconductors the valence electrons are not detached from the ions like in metals, but they are localized between atomic lattice sites forming covalent bonds between the atoms of the material. When a laser pulse is incident on the material, the valence electrons absorb photons and some of them become excited from bonding to anti-bonding states. As a result free carriers are created in the photoexcited region and electronic charge is removed from areas located between the ions. Due to the removal of the negative charge, the screening of the ionic potential is reduced and the ions start repelling each other. The lattice deforms in order to reach the new equilibrium position. According to the Lindemann criterion [45] if the atomic displacement exceeds 10–20% of the lattice constant the solid will melt. This is a non-thermal melting mechanism because it happens really quickly after the arrival of the laser pulse, before the electrons have the time to equilibrate and reach a uniform temperature T_e. Moreover, the lattice does not deform due to large-amplitude oscillations induced by an increase in its temperature, as in thermal melting, but due to deformation created by the altered potential landscape after the electronic photoexcitation. The experimental studies showed that the process is complete in hundreds of femtoseconds, much faster than the picosecond time scale of the thermal melting mechanism, set by the electron-phonon coupling constant.

Theoretical investigations [46] came soon after the experimental realization of non-thermal melting. Figure 2.13 shows calculations of the cohesive energy per atom in the lattice of Si as a function of the amplitudes of the transverse and longitudinal phonons δ_t

and δ_l, respectively. Figure 2.13(a) shows material in equilibrium; the energy is minimum at $\delta_t = \delta_l = 0$; the ions prefer to stay at the equilibrium position and phonon excitation is not preferable. Figure 2.13(b) shows the material when a dense electron-hole plasma has been excited by a laser pulse. In this particular case it is assumed that 15% of the valence electrons have been excited to anti-bonding states ($\xi_0 = 0.15$). We see that what before was a minimum now is a saddle point; a repulsive potential has been established from the presence of the electron-hole plasma and the excitation of phonon modes, leading to lattice deformation is preferable.
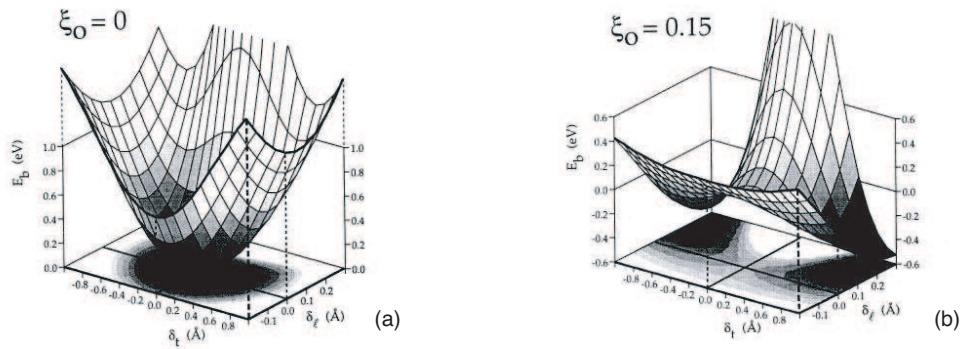
Figure 2.13: (a) Calculation of the cohesive energy per atom as a function of transverse (δ_t) and longitudinal (δ_l) phonon amplitudes for Si in equilibrium. (b) After the photoexcitation of 15 % of the valence electrons a repulsive potential is established . After Ref. [46].

Figure 2.14 shows several trajectories resulting from the potential surface of Figure 2.13(b). Before the laser pulse ($t < 0$) the crystal is stable and it performs oscillations within the dark region around the ideal diamond structure where $\delta_t = \delta_l = 0$. The different trajectories shown in the Figure result from different phases in the oscillations. After the laser pulse a superposition of transverse and longitudinal phonons is excited and leads the atoms to increasing displacements from the equilibrium position. When the displacements become large enough, which happens 100 fs after the arrival of the laser pulse, the atoms are far enough from the lattice sites that long-range order is lost and Si reaches the molten

state, which is metallic rather than semiconducting.
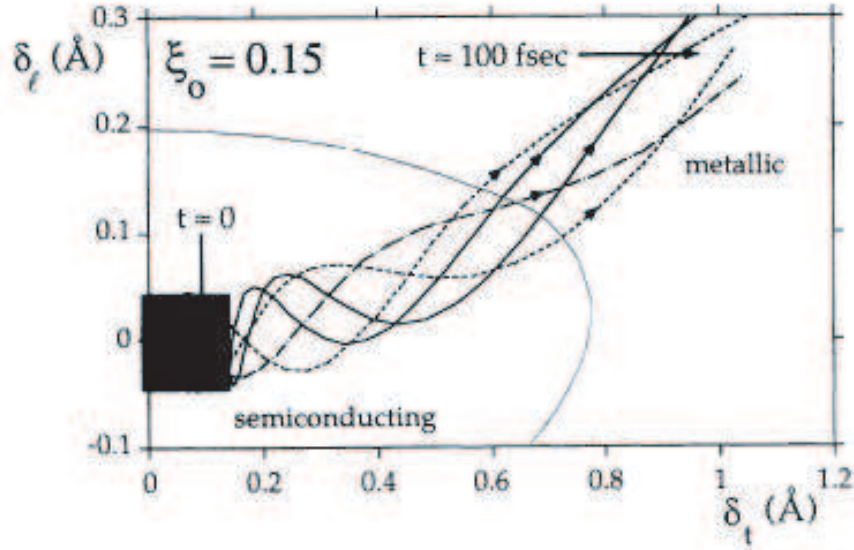
Figure 2.14: Ionic trajectories following the potential of Figure 2.13(b). 100 fs after the arrival of the laser pulse Si has melted into a metallic state. After Ref. [46].

The two mechanisms, thermal and non-thermal melting differ drastically. In thermal melting the lattice equilibrates with the electrons and heat is transferred from one system to the other. In non-thermal melting the two systems do not have time to equilibrate. Thermal melting is induced by large amplitude oscillations triggered from the increase in the lattice temperature. Non-thermal melting is induced by ionic deformations caused by a repulsive potential established between the ions due to the presence of the photoexcited electron-hole plasma. Experimentally, the clear signature of non-thermal melting is the subpicosecond time scale of the effect. Thermal melting takes picoseconds to occur because it depends on electron-phonon coupling processes which are slower.

2.3   Summary

The interaction of light with matter is described by the Maxwell equations. The effects of mater are cast in the dielectric function, which depends on the electronic configuration of the material. Most materials are described successfully by combining the free and bound electron models for the dielectric function. Knowledge of the band structure of a solid helps in explaining the optical properties, along with the Fresnel equations which relate observable quantities, such as reflectivity or transmissivity, to intrinsic material properties like the dielectric function. When the incident electromagnetic field is strong it can create permanent structural changes in a solid. With the advent of femtosecond lasers new mechanisms for melting were discovered. Thermal and non-thermal melting are customarily initiated in the laboratory in order to help the understanding of the response of matter under extreme conditions. In chapter 5 we will present our results on the solid-to-liquid phase transition of aluminum and discuss whether it is a thermal or a non-thermal process.

Chapter 3

Experimental Setup and Technique

Time-resolved measurements are of fundamental importance in the study of material properties. Intense laser pulses serve as a first step in order to excite an electron-hole plasma inside the material. In the strong excitation regime a big electronic population is excited and the material is prepared in an exotic state. The pathway of the material evolution after such an excitation reveals much information about the mechanisms involved in phase transitions. The response of a material during the first picosecond after photoexcitation is extremely critical in defining the evolution of the material state. Therefore, dynamical studies with femtosecond time resolution are needed for elucidating the relevant processes. Although pulsed x-ray and electron sources advance rapidly towards the few-femtosecond regime, optical pulses remain the shortest probes we have for time-resolved experiments. In this chapter we will discuss the optical methods by which we acquire time-resolved measurements and we will elaborate on our expansion of a previous experimental technique. As an illustration of our technique we will present results obtained in our laboratory and we will close with a discussion of the limitations of our setup.

3.1 The pump-probe technique

3.1.1 Introduction to pump-probe methods

There is a myriad of processes that take place in ultrafast time scales in materials. As a matter of fact, the response of a material during the first picosecond after the arrival of a femtosecond laser pulse is the most important in determining the outcome of the interaction of the medium with light. In chapter 2 we discussed laser-induced non-thermal melting, a process with a subpicosecond time scale, as well as thermal melting, a process taking tens of picoseconds to be completed. These are only two examples out of a wide variety of physical processes that result from the interaction of short pulses of light with matter. Upon the arrival of a femtosecond pulse on the surface of a material, carrier excitation and the creation of an electron-hole plasma takes place within tens of femtoseconds [9]. The excited carriers will then thermalize with the lattice within piscoseconds [47] . When the intensity of the incident laser pulse is high enough, melting and ablation will occur within nanoseconds [11] and the material will resolidify within microseconds [48].

The challenge lies in the detection of such fast processes. Electronics are not fast enough to offer any time-resolved information. The field of ultrafast spectroscopy needs another tool for the study of laser-induced dynamics [49–51]. One solution is provided by the pump-probe method, which uses ultrashort laser pulses not only for creating the processes under study but also for detecting them. A schematic of the pump-probe method is shown in Figure 3.1. A laser pulse, called the *pump*, irradiates the surface of the sample under study and initiates a sequence of physical processes. A second pulse, much weaker in intensity, called the *probe*, arrives some time after and upon reflection it is collected by a detector. By varying the time delay between the pump and the probe, $\Delta\tau$, we can measure how the reflectivity of the material evolves in steps of $\Delta\tau$ after the photoexcitation created

by the pump. From such data we can obtain information about the temporal and spatial evolution of the excited carrier distribution arising from scattering processes or transport from the region of excitation.
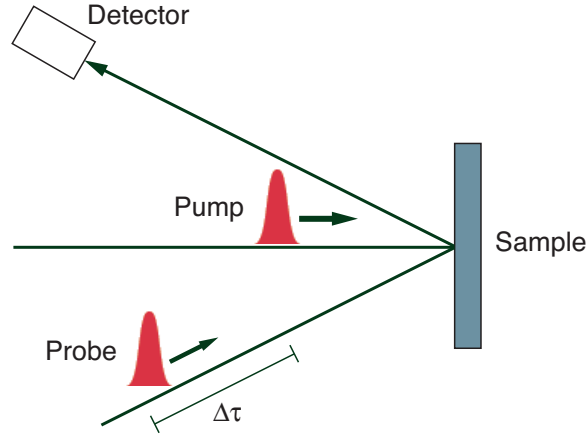
Figure 3.1: Schematic representation of pump-probe setup.

The time resolution of the method is limited by two factors: the size of $\Delta\tau$ and the duration of the probe pulse. We vary the time delay, $\Delta\tau$, by mounting the optics that guide either the probe or the pump beam on a translation stage, as shown in Figure 3.2. By varying the beam path we vary the arrival time of the pulse on the sample. We have translation stages that can move with the precision of $\Delta l = 100$ nm, which corresponds to a time step of $\Delta\tau = \frac{2\Delta l}{c} = 0.6$ fs. The factor of 2 arises from the fact that light travels back and forth the translation stage, as shown in Figure 3.2, and c is the speed of light. The time resolution of a pump-probe setup is rarely 0.6 fs and the reason is that the duration of the probe pulse is usually bigger than that. If we consider a 20-fs long probe pulse then we know that these 20 fs will appear as one instant in our measurements because the probe signal will be integrated in the detector. Therefore the 0.6 fs time difference provided by the translation stage will be lost in the 20-fs long integration of the probe and the detector

will not distinguish the delay steps. The result is that the time resolution of pump-probe experiments is most often limited by the duration of the probe pulse.
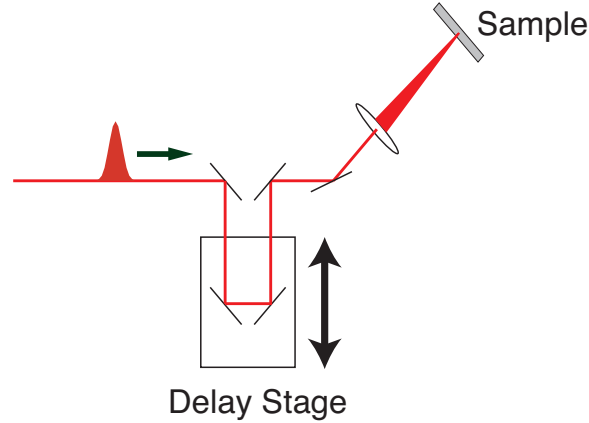
Figure 3.2: Schematic representation of a delay line.

The probe is usually much weaker than the pump in order to minimize the photoexcitation it creates. Ideally we would like a probe that does not add any excitation to the material under study but it is impossible to measure a system without perturbing it. To minimize our perturbation, we use probe pulses that are more than 1000 times weaker in intensity than the pump pulses and therefore the effects created by them are negligible compared with the effects created by the pump. Furthermore, in order to ensure probing of a uniformly excited sample area, we keep the probe spot size on the sample surface much smaller than the pump spot size. Finally, to avoid scattered pump light entering the detection area, we keep the pump and the probe beams cross polarized, and with the aid of a polarizer mounted in front of the detector we select only the polarization of the probe.

Many different pump-probe techniques exist to study a material's response to an incident laser pulse. The pump-probe setup shown in Figure 3.1 corresponds to the particular case of a reflection setup [52,53]. Other optical measurements, such as transmissivity [54]

and second-harmonic generation [10], can be employed in a pump-probe setup in order to investigate the material's transient dielectric response to optical excitation. The choice of technique depends on the material and the question under study. For liquid samples with weak reflectivity transmission pump-probe is the best tool for ultrafast spectroscopy, while for opaque solid samples reflectivity is a more suitable probe. For crystalline materials second harmonic generation is a useful probe because the ability of a material to generate the second harmonic depends on the centrosymmetry of the lattice [55, 56]. For melting and ablation experiments, femtosecond microscopy, a variation of the reflection method, is often used [11, 21, 48, 57]. In femtosecond microscopy the probe images the pumped area of the sample with femtosecond time-resolution. In contrast to a typical pump-probe reflection setup, the spot size of the probe is bigger than the spot size of the pump in order to be able to capture the entire photoexited area. Regardless of the choice of technique, in all pump-probe experiments the idea is the same: the pump pulse arrives first and the probe follows with a varying time delay which allow us to track the evolution of the material properties with temporal resolution that depends on the probe pulse duration.

So far we have discussed optical pump-probe settings only, where both the pump and the probe pulses are laser pulses. Historically, this type of experiment was the first one to appear because the optical pulses were the only available pulses with femtosecond time duration, thus allowing for subpicosecond time resolution. Recently, however, notable progress was made in the generation of pulsed, subpicosecond x-ray [29, 37, 39, 45] and electron sources [58]. X-ray pulses of femtosecond time duration can serve as a probe by letting them diffract through the photoexcited material –often the pump is still an optical pulse– and collect the time-resolved diffraction spectra. Similarly, one can let an electron pulse of femtosecond duration to be diffracted though the material and collect the diffracted electron pattern. In both cases we obtain time-resolved information on the position of the

atoms in the lattice since both x-rays and electrons interact with the atoms only. This type of measurement provides us with a microscopic view of the material under study. Optical measurements cannot provide such a microscopic view but have the advantage that they give a complete picture of both structural and electron dynamics, while the latter cannot be detected with an x-ray or electron diffraction experiment. Subpicosecond x-ray sources preceded electron subpicosecond sources because the latter face implications arising from space-charge effects that broaden the pulse [59]. However, there are significant advantages in utilizing a subpicosecond electron source because the scattering cross-section of electrons is $10^5 - 10^6$ times bigger than the scattering cross section of x-rays.

In the following section we will describe the experimental setup of the technique we employ in order to perform ultrafast spectroscopy of highly excited materials. Our technique is a reflective pump-probe technique with a twist: the probe is not a single-wavelength laser pulse, as is usually the case with optical pump-probe experiments, but a white-light beam containing a continuum of frequencies across the visible and the UV.

3.1.2 White-light pump-probe setup

Over the past 10 years, our laboratory has made great advances in studying electron and lattice dynamics in highly photoexcited semiconductors [44]. We developed a unique time-resolved, broadband dual angle reflectometry technique [60], which allows us to probe the dielectric function of a solid with femtosecond time resolution. Our setup has a time resolution of 20 fs and a broadband frequency range extending from the near infrared to the near ultraviolet. Because our laser system is amplified, we are able to excite the materials under investigation to well above the damage threshold. This allows us to create exotic states of matter that contain excited electronic populations up to 3 or 4 orders of magnitude larger than previous weak excitation studies. In contrast to traditional single-

wavelength reflectivity and second-harmonic data, broadband dielectric data provide direct information on the response of an intrinsic optical property of the material. Recently, using our broadband technique, we directly observed an ultrafast semiconductor-to-metal phase transition [36] and demonstrated all-optical control of the lattice configuration of a highly excited semiconductor via optical phonon excitation [61].

Figure 3.3 shows our experimental setup. We use a commercially available Ti:sapphire oscillator to seed a home-built, 1-kHz repetition rate, Ti:sapphire multipass amplifier which produces 40-fs, 0.5-mJ pulses at 800 nm. The design of the amplifier follows that of Backus *et al.* [62]. The multipass amplifier allows seven passes of the oscillator pulse through the amplifying Ti:sapphire crystal before the beam exits the amplifier. A mask placed in the amplifier path inhibits the propagation of amplified spontaneous emission (ASE). At the output of the laser system we typically measure ASE to be 10% of the total output power.

In Figure 3.3 we see that the output of the laser system is split by a beamsplitter in two parts: one becomes the pump beam and maintains 90% of the laser output power while the other 10% becomes the probe beam, or more accurately, the seed for the white light which we will use as the probe beam. The pump beam passes through a waveplate-polarizer combination which, by rotating the waveplate, allows for the modulation of the intensity of the beam according to the needs of the experiment. Moreover, the polarizer ensures that the pump beam is *s*-polarized, perpendicular to the *p*-polarized probe beam. Next, the pump beam goes through a delay stage allowing for a variable time delay with respect to the probe beam in order to achieve time-resolved measurements. In section 3.1.1 we mentioned that the variable time delay can be provided by either the pump or the probe beam. In our experiment, we send the pump beam through the delay stage because the alignment of the pump is less critical than the alignment of the probe. In the actual setup we can further split the pump beam into two pump beams in order to allow for double-
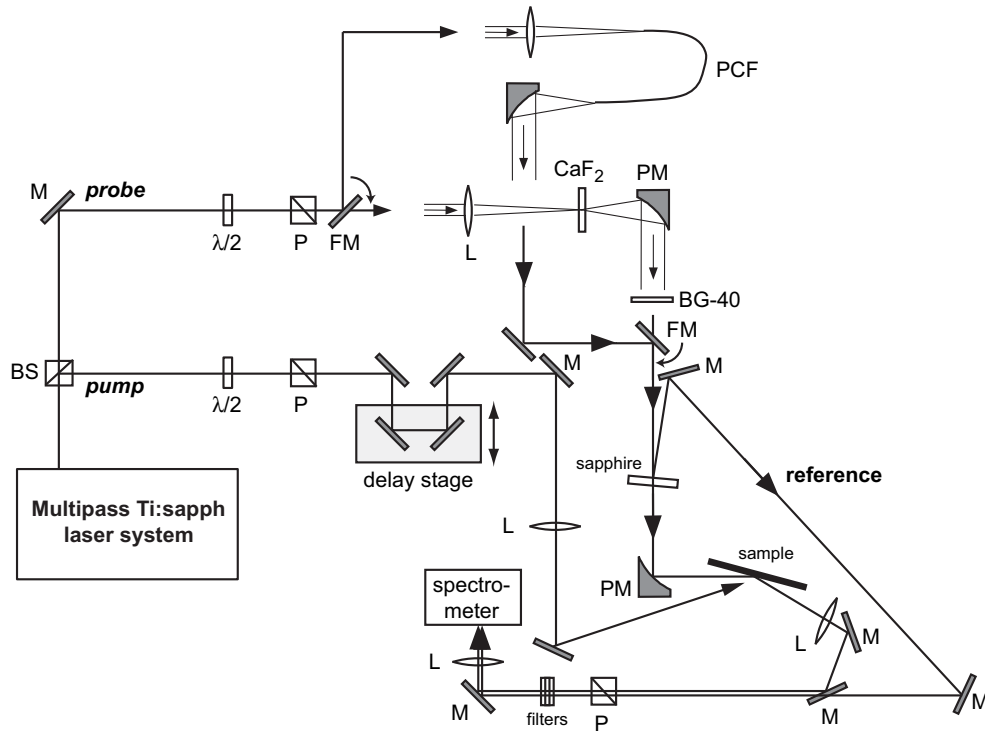
Figure 3.3: Schematic representation of white-light pump–probe setup. BS = polarizing beam splitter; M = flat mirror; PM = parabolic mirror; FM = flipper mirror; L = lens; P = polarizer; $\lambda/2$ = half-wave plate; PCF = photonic crystal fiber.

pump experiments, most suitable for optical control studies [61]. In the double-pump setup we send each of the split pump beams through a delay stage in order to allow for variable time delays between the pump beams and the probe. Our delay stages are motorized, long-travel, computer-controlled translation stages with 100 nm step resolution, which, as we discussed in section 3.1.1, yields time delays significantly below the probe-width limited time resolution. Therefore the delay stages are not a limitation on the specifications of our setup. After exiting the delay stage, the pump beam passes through a slowly focusing lens, focal length 20 cm, and on to the sample surface. In most cases we position the sample before the focal spot of the lens so that the pump beam has a considerably larger diameter than the tightly-focused probe beam at the sample surface. Depending on the nature of

the experiment we want to perform, we can vary the distance between the sample and the pump focusing lens in order to allow for more or less focused pump light, resulting in higher or lower pump intensity at the sample surface.

The sample is positioned on a mounting system, which allows for translation in all x, y, and z directions, as well as rotation. The translation, which is computer controlled, gives us the opportunity to perform above damage threshold experiments where the sample needs to be translated between each laser shot as the changes induced by the previous laser pulses are permanent. Indeed the results presented in this thesis were taken under single-shot conditions, meaning that the sample was irradiated each time by a single pump and a single probe pulse and then it was translated in order for the next pulses to irradiate a fresh surface area. The rotation stage allows us to change the angle of the sample and therefore to vary the angle of incidence for the experiment. As we will discuss below, the sensitivity of our measurements depends on the choice of the angle of incidence.

The beam path of the pump stops at the sample surface. After the pump light is absorbed by the material it is of no further use to the experiment and the reflected part of the pump must be blocked so it does not interfere with the rest of the setup. The probe, on the other hand, is guided on the sample and its reflection is collected and measured by a spectrometer. As we see in Figure 3.3 the 10% of the laser output, which serves as the probe, has two options depending on the orientation of a flipper mirror: it will serve as a white light seed for either a CaF_2 crystal or for a photonic crystal fiber (PCF). In both cases the output is a white-light pulse but it spans different wavelengths. Given an 800 nm seed the CaF_2 crystal generates white light in the visible and the UV while the PCF generates light in the visible and the infrared. Depending on the application we can choose either one of the two white-light sources. We will elaborate on the white-light generation mechanisms later. In both cases the diverging white-light beam is recollimated by a parabolic mirror

and guided towards the sample where it is focused tightly by another parabolic mirror. We make sure that the spot size of the probe beam is at least four times smaller than the spot size of the pump beam.

A small part of the incident probe beam is reflected by a 1-mm thick piece of sapphire mounted before the sample and becomes the *reference* beam, shown in Figure 3.3. The part of the white-light beam that we let reflect off the sample is called the *reflected* beam. Both the reflected and the reference beams are directed in a CCD spectrometer which uses a prism to spatially separate the different colors and measure their relative intensities. This way we can measure the reflectivity of each color contained in the white light and present broadband data. The white light which is generated by the CaF_2 crystal is detected by a silicon based CCD spectrometer. However, silicon detectors are not sensitive in the infrared because infrared photons do not have enough energy to bridge the silicon band gap and excite electrons from the valence to the conduction band. The result is that silicon does not react to infrared light and it cannot be used as an IR detector. The exception is microstructured silicon devices which, due to sulfur doping, are sensitive both to the visible and to the IR [63–65]. Therefore, for the white light generated by the PCF an InGaAs detector array is used, which is sensitive to the infrared. Both the reflected and reference beams are measured and the ratio of the reflected by the reference becomes our data set. The reason for this extra step is the large fluctuations in the white-light intensity. As we will discuss later, white light generation is the result of a superposition of nonlinear processes. Nonlinear processes depend critically on the intensity of the seed pulse and therefore small intensity fluctuations in the output power of the laser translate into large intensity fluctuations, as large as 10%, in the white light intensity. We account for white-light fluctuations by splitting each white light pulse into a reflected and a reference pulse and normalizing the reflected part to the reference. Without this crucial step we

would mistakenly interpret the reflectivity changes of the material under study.

We only use reflective optics in order to direct the white-light beams. For example, for recollimating or focusing the beams we prefer to use parabolic mirrors rather than lenses. The reason is that we want to avoid dispersive stretching of the white-light pulses. Dispersive stretching occurs in all light pulses every time they travel through a medium, including air, because the index of refraction of any material is a function of frequency (*c.f.* Eq. 2.34). Therefore, each of the frequencies contained in a laser pulse travels at a different speed through a medium and the pulse stretches in time. The situation is of course more dramatic for a white-light pulse due to the wide range of frequencies contained in it. In order to prevent dispersive stretching we avoid transmissive optics in the path of the white-light beams and we use reflective optics which do not stretch the pulses. In order to ensure the highest time resolution in our experiments, we need the white-light pulse to be the shortest *at the sample surface*. This is the important point where the pulse gathers information about the material's response and we want this information to be divided in the shortest time window possible. The duration of the white-light pulse when it arrives at the detector is of no importance, since the pulse will be integrated anyway. The integrated value corresponds not to one instant in time, but to a time interval, which is equal to the duration of the probe at the sample surface. Therefore, after the pulse reflects off the material surface we can use transmissive optics without affecting the time resolution of our experiment. Indeed, the reflected part of the white light is recollimated by an achromatic lens and later it passes through a polarizer which ensures that only *p*-polarized light will arrive at the detector. This way scattered pump light, which is of *s*-polarization, does not make it in the detector.

Our experimental setup is a more complicated version of a traditional reflection pump-probe setup. The additional feature obtained with our setup is the ability to perform

broadband measurements because we use white light as a probe and not a single-color pulse. Therefore, the generation of white light is of vital importance for our technique. In the next sections we will discuss in more detail the mechanisms involved in white light generation.

3.1.3 White light generated by CaF$_2$

CaF$_2$ is a transparent solid material with a large bandgap of 10.2 eV. White light is generated by focusing an 800-nm pulse into a 3-mm thick piece of CaF$_2$. A number of nonlinear optical processes, including self-focusing, self-phase modulation, self steepening, avalanche ionization, and multiphoton ionization contribute to the generation of this white-light continuum [66, 67]. We will discuss self focusing and self phase modulation in more detail because they are very important for the generation of white light and they illustrate how nonlinear effects can affect a laser pulse both spatially and temporally.

In chapter 2, where we discussed the interaction of light with matter, we examined only linear effects, *i.e.* effects that depend linearly on the incident electric field $\mathbf{E}$. The point where our discussion became linear was when writing Eq. 2.11, where we assumed that the polarization $\mathbf{P}$ induced in a medium by the presence of an electric field $\mathbf{E}$ depends linearly on the field,

$$\mathbf{P} = \epsilon_0 \chi_e \mathbf{E}. \tag{3.1}$$

This is not always the case, however, because for very strong fields nonlinear terms appear and a more complete description needs to take these nonlinear terms into account, writing

$$\mathbf{P} = \epsilon_0 \chi^{(1)} \mathbf{E} + \epsilon_0 \chi^{(2)} : \mathbf{E} \cdot \mathbf{E} + \epsilon_0 \chi^{(3)} :: \mathbf{E} \cdot \mathbf{E} \cdot \mathbf{E} + \cdots . \tag{3.2}$$

What we defined in chapter 2 as electric susceptibility of the medium, χ_e, is actually the linear susceptibility, $\chi^{(1)}$. The polarization depends on higher orders of the electric field and each one of them contributes to the final signal according to the value of the corresponding nonlinear susceptibility, $\chi^{(2)}, \chi^{(3)}$, etc. In most materials the higher order susceptibilities are small compared to the linear susceptibility and nonlinear effects become important only at very high field intensities. In the case of femtosecond laser pulses the intensities are indeed very high due to the short duration of the pulses.

For centrosymmetric materials even-order susceptibilities, that is $\chi^{(2)}, \chi^{(4)}$ etc., vanish and only odd-order susceptibilities remain [55, 56]. In this case, the dominant terms in Eq. 3.2 become

$$\mathbf{P} = \epsilon_0 \chi^{(1)} \mathbf{E} + \epsilon_0 \chi^{(3)} :: \mathbf{E} \cdot \mathbf{E} \cdot \mathbf{E}. \tag{3.3}$$

Equation 3.3 can be rewritten as [55]

$$\mathbf{P} = \epsilon_0 \left(\chi^{(1)} + 3\chi^{(3)} |\mathbf{E}|^2 \right) \mathbf{E}. \tag{3.4}$$

Combining Eqs. 2.5, 3.4, and 2.7 we obtain

$$\epsilon_{eff} = 1 + \chi^{(1)} + 3\chi^{(3)} |\mathbf{E}|^2, \tag{3.5}$$

where the linear part of the dielectric function is still given by Eq. 2.12, $\epsilon = 1 + \chi^{(1)}$. The index of refraction is now redefined with the aid of Eq. 2.34 as

$$
\begin{aligned}
n_{eff} &= \sqrt{1 + \chi^{(1)} + 3\chi^{(3)}|\mathbf{E}|^2} & (3.6) \\
&= \sqrt{\epsilon + 3\chi^{(3)}|\mathbf{E}|^2} & (3.7) \\
&= n\sqrt{1 + \frac{3\chi^{(3)}}{\epsilon}|\mathbf{E}|^2} & (3.8) \\
&\approx n + \frac{3\chi^{(3)}}{2n}|\mathbf{E}|^2, & (3.9)
\end{aligned}
$$

for small $\frac{\chi^{(3)}}{\epsilon}|\mathbf{E}|^2$. Given that the intensity of the electric field is proportional to the square amplitude of the field, $I \sim |\mathbf{E}|^2$, the effective index of refraction can be written as [68]

$$
n_{eff} = n + n_2 I. \tag{3.10}
$$

Equation 3.10 describes the most important implication of nonlinear effects: the index of refraction depends not only on the frequency but also on the intensity of the incident field. We note here that this is the result of keeping only the $\chi^{(3)}$ term in the polarization expansion, given by Eq. 3.2. The effects of self focusing and self phase modulation are both consequences of the intensity dependent index of refraction.

We can understand self-focusing if we consider that for most laser systems the output beam intensity has a Gaussian dependence on space when looking at the beam cross section. For example, if the beam propagates along the z direction, the envelope of the intensity profile of the beam along each of the x and y directions looks like Figure 3.4.

The intensity of the beam is higher near the center and decays fast as we move towards the wings. From Eq. 3.10 we know that the index of refraction is higher when the intensity of the beam is higher. This is the case for positive n_2, which is actually true for most materials. Therefore the center of the beam experiences a higher index of refraction than the wings, as it propagates through a medium. This is equivalent to propagating the beam through a lens, where the middle part of the lens is thicker, and therefore the central
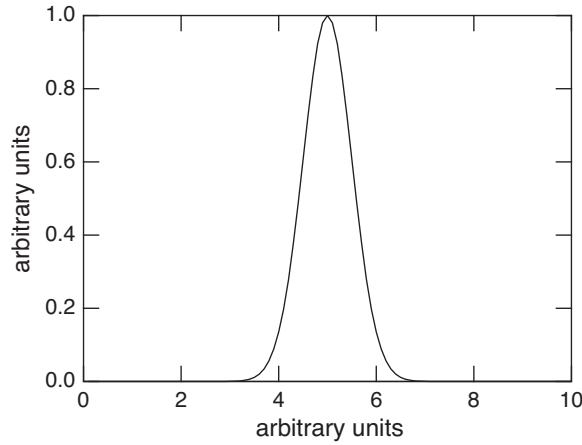
Figure 3.4: Gaussian function.

part of the beam travels through more material thus experiencing the effect of the index of refraction more than the wings do. The result therefore is the same: when an intense beam propagates through a medium the central part experiences higher index of refraction and the beam focuses, in the same way that a beam focuses when it passes through a lens. The effect is called self-focusing because it is the intensity profile of the beam itself that initiates it.

Self-phase modulation is the analogous temporal event of self-focusing. This time the relevant feature of the beam is that, apart from having a Gaussian intensity envelope as a function of cross section coordinates, it also has a Gaussian intensity envelope in time. Figure 3.4 applies again with the horizontal axis being the time axis. The middle part of the beam –temporally speaking– experiences a larger intensity-dependent index of refraction than the leading and trailing edges of the pulse. Therefore the middle part becomes delayed with respect to the edges and it runs away from the leading edge, while at the same time it moves closer to the trailing edge, as shown in Figure 3.5. This effect generates red frequencies at the leading edge of the pulse and blue frequencies at the trailing edge of the

pulse.
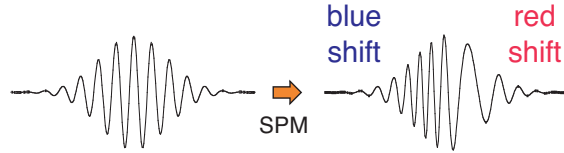
Figure 3.5: The effect of self-phase modulation on the spectral content of a pulse.

Self-phase modulation is one mechanism that generates new frequencies from a given pulse, which is necessary for white light generation. However, it is not the only mechanism responsible for the generation of new frequencies. The other mechanisms mentioned above contribute new frequencies as well. Self-focusing increases the intensity in the middle part of the pulse thus enhancing the effect of the other nonlinear processes, which all depend on the intensity of the beam.

The white-light spectrum we obtain from CaF_2 is shown in Figure 3.6. The narrow peak is the spectrum of the 800-nm (1.55 eV) pulse we use as seed for the white light generation. The white-light spectrum is shown by the bold line. We observe that most of the broadening is happening towards the blue frequencies. The spectrum we show in Figure 3.6 is white light filtered by a BG-40 filter which absorbs photons with energies lower than 1.55 eV. This is why the white light does not seem to have a strong component at the 1.55 eV energy of the seed pulse. In fact, most of the energy of the seed pulse remains around 1.55 eV, thus filtered by the BG-40, and only a small part of the seed energy is converted to higher frequencies, which are then used to irradiate the sample.
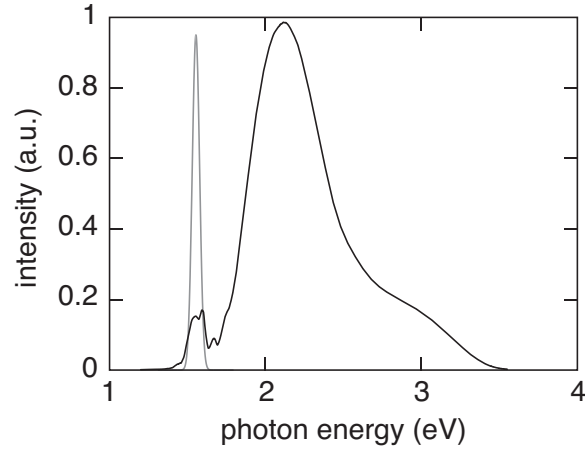
Figure 3.6: Spectrum of white light generated by a CaF_2 crystal (bold line). The spectrum is recorded after the white light has been filtered by a BG-40 optical filter. The narrow peak at 1.55 eV is the spectrum of the seed pulse.

White light can be generated by other materials such as water, fused silica, or LiF to name a few [69]. In all cases the seed pulse energy needs to be on the order of μJ, so the effect can only be observed with amplified laser systems. We prefer to use CaF_2 because it gives the broader spectrum while being easy to use. LiF is the only material that produces broader spectrum than CaF_2 but it is hydroscopic and difficult to handle.

Although we do not send white-light pulses through transmissive optics in order to avoid dispersive stretching (chirp), the pulses are already stretched when they exit the CaF_2 crystal due to the frequency generation mechanisms and due to the propagation through the 3-mm CaF_2 crystal and through air. Figure 3.7 shows the chirp of our white light measured on a Te sample [61]. We observe that across 1.7–3.5 eV the duration of a white-light pulse is 800 fs. As shown in Figure 3.7 this means that different colors contained in the white-light pulse arrive at the sample surface at different times. In order to correct for this chirp we time shift the final reflectivity data accordingly.

CaF_2 is a reliable white-light source, suitable for ultrafast spectroscopic experi-
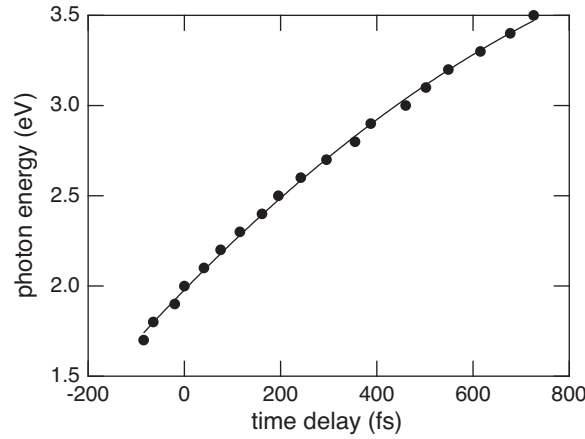
Figure 3.7: Chirp of white light generated by a 3-mm thick CaF_2 crystal, measured on a Te sample [61].

ments. The spectrum of the generated white light pulses is not greatly affected by laser intensity fluctuations, but the white-light intensity is affected. This limits the sensitivity of our experimental setup to the detection of reflectivity changes down to 2-3%. This is adequate for the study of structural phase transitions where the change in the reflectivity signal is around 10%. For studies where the change in the reflectivity is less, other detection schemes need to be used.

3.1.4   White light generated by a photonic crystal fiber

For experiments where it is important to measure reflectivity changes in the infrared it is not suitable to use CaF_2 seeded by an 800-nm pulse. As we observe in Figure 3.6, CaF_2 creates only blue broadening in the spectrum of the seed pulse. Therefore if we need to generate frequencies in the infrared we have two solutions. One is to downconvert the frequency of the seed pulse using an optical parametric amplifier and generate a seed pulse with higher wavelength. Then we will obtain infrared and visible frequency components by blue broadening. The other, slightly less involved solution, is to seed a photonic crystal

fiber with the 800-nm light generated by our laser system.

Photonic crystal fibers, or microstructured fibers, use a microstructured cladding region with air holes to guide light in a pure silica core. Figure 3.8 shows SEM pictures of the cross section of the photonic crystal fiber we use in our setup. This fiber has a core of 1.8 μm diameter surrounded by a cladding region of 120 μm diameter. The entire structure is protected by an acrylate coating with a diameter of 240 μm.
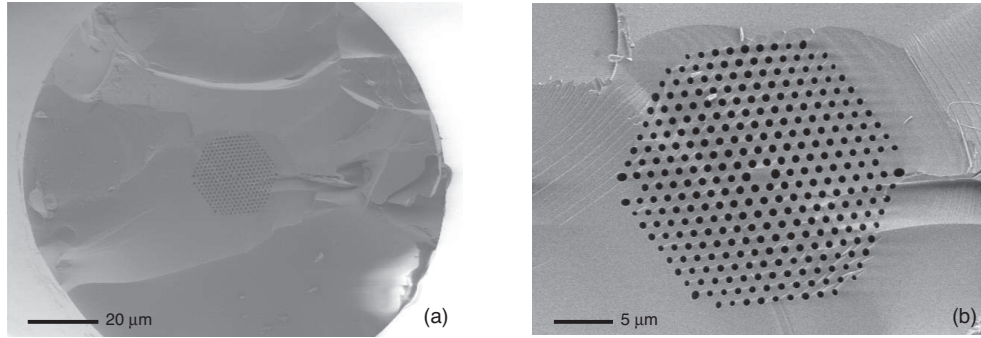
Figure 3.8: SEM pictures of the cross section of a photonic crystal fiber used for supercontinuum generation.

Unlike photonic crystal fibers, standard optical fibers [5] are made of a homogenous dielectric core surrounded by a homogenous dielectric cladding producing a step variation in the index of refraction. Guiding of light in optical fibers is a result of total internal reflection when the index of refraction of the core is higher than the index of refraction of the cladding. Standard optical fibers already find numerous applications ranging from telecommunications to medical diagnostics. Photonic crystal fibers, on the other hand, guide light through photonic band gap effects [70]. The photonic band gap, meaning a range of photon energies which cannot propagate in any direction in the medium, arises from the periodically varying index of refraction in a photonic crystal fiber much in the same way that the electronic band gap arises from the lattice periodicity in a semiconductor. A photonic crystal fiber with an extremely small glass core, like the one shown in Figure 3.8,

enhances nonlinearities dramatically by tight light confinement and is suitable for white light generation [5]. In applications where nonlinearities are not welcome the core can instead be made of air.

The idea of photonic crystals, meaning periodic arrangements of dielectrics, emerged in 1987 in order to address strong light localization and inhibition of spontaneous emission. Later, it was shown that in photonic crystals the propagation of light can be totally suppressed at certain wavelengths for all propagation directions and polarizations, opening a photonic band gap [70]. For the frequencies contained in the band gap, the light density of states vanishes, so even spontaneous emission of light is inhibited. An example of a one-dimensional photonic crystal is the Bragg mirror, also known as multilayer reflector. Multilayer reflectors consist of a periodic stack of alternating dielectric layers and are customarily used as low-loss high reflectors in optical applications. They maintain the feature of high reflectivity only for certain frequencies around the operating frequency because the thickness of the layers has to be a specific fraction of the light wavelength for the reflector to work. Two-dimensional photonic crystals can be constructed by etching holes in a slab waveguide and are used in integrated photonic circuits. Three-dimensional photonic crystals were first constructed by drilling an array of holes at three different angles into a dielectric material.

The concept of guiding light in a photonic crystal fiber is based on introducing a defect which creates states inside the bandgap [71, 72]. If the defect is a single point the light emitted by it will remain confined around the defect since it cannot propagate due to the existence of the band gap. If the defect is a line then light will remain confined around the defect but will be able to propagate along it. This is the case in our photonic crystal fiber shown in Figure 3.8, where the silica core serves as a defect that guides light inside the photonic crystal created by the cladding. In conventional fibers, propagation can only

occur if the core is of higher index of refraction than the cladding. In photonic crystal fibers, however, the defect can confine and guide light in a low refractive index medium. Thus, these fibers can guide light in a gas, air, or even vacuum. Guiding light in vacuum offers orders of magnitude reduction in losses and nonlinear effects, allowing for high power applications. Moreover, guidance of atoms, molecules or cells through hollow core optical fibers could be possible.

In our setup we use a photonic crystal fiber for white light generation where nonlinearities play an important role [73]. For this reason we use a silica core fiber with a small core diameter which enhances nonlinear effects. Due to the long propagation length over which the light is tightly confined, the input energy required for white light generation is much smaller in photonic crystal fibers than in CaF_2. As we mentioned above, in order to generate white light in CaF_2, water, or fused silica we need amplified pulses with energies on the order of μJ. One big advantage of using photonic crystal fibers is that they can generate white light using an input energy on the order of nJ and therefore non-amplified oscillator-only laser systems are sufficient for white light generation [74]. The mechanism by which infrared broadening is achieved in white light generation in photonic crystal fibers is based on soliton launching [75]. The input pulse breaks up into solitonic pulses inside the fiber. Solitons are wave packets that propagate inside the fiber unaffected, due to a balance between anomalous dispersion and self-phase modulation [5]. This gives the solitons the opportunity to interact repeatedly with the material and through multiple Raman self-frequency shift events, which continuously transfer energy from shorter to longer wavelengths, infrared frequencies are generated in the resulting spectrum. Frequencies are also generated on the blue side of the seed pulse due to transfer of energy in the normal dispersion regime via the generation of non-solitonic dispersive wave-radiation [76].

Figure 3.9 shows the spectrum of the white light we take out of the photonic crystal

fiber shown in Figure 3.8. This spectrum is obtained by focusing the 800-nm probe seed in the 130-cm long photonic crystal fiber using a 40x microscope objective lens. Alignment of light into the fiber is very critical. For this reason we use an ultra-high precision 3D translation stage on which we mount the front end of the fiber. The front end of the fiber needs to be cleaned thoroughly and cleaved properly in order to couple light efficiently into the fiber. We attenuate the input power of the seed pulse as much as possible. Given that this pulse carries μJ of energy it is possible that it can damage the fiber. By attenuating the pulse we end up with ~ 400 nJ of energy which are enough for white light generation but not enough to damage the fiber. This spectrum is recorded with a monochromator followed by an InGaAs amplified photodiode, which is sensitive to the infrared. We note that the white light produced by the photonic crystal fiber exhibits severe infrared broadening, reaching up to 1400 nm in wavelength.
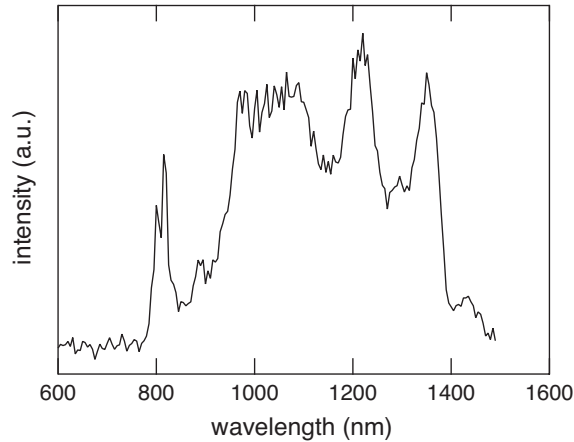

Figure 3.9: Infrared part of white-light spectrum generated by a 130-cm photonic crystal fiber.

In Figure 3.9 only the infrared part of the white light is shown because the spectrum is recorded with an InGaAs photodiode, which is not sensitive to the visible light regime. Figure 3.10 shows the spectrum recorded with a Si amplified photodiode following

a monochromator. We observe that there is also significant blue broadening in the spectrum of the seed pulse, extending down to 400 nm. Therefore the total spectrum of the white light generated by the photonic crystal fiber extends from 400 to 1400 nm!
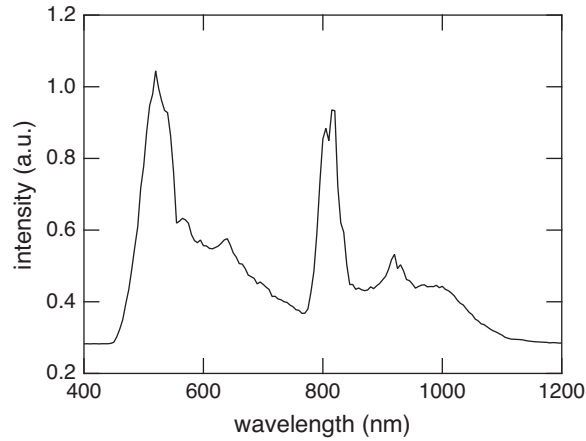
Figure 3.10: Visible part of white-light spectrum generated by a 130-cm photonic crystal fiber.

The spectra in Figures 3.9 and 3.10 are produced by a fiber 130 cm long. The length of the fiber affects the frequency range of the white light. If the fiber is too short, spectral peaks will be generated at frequencies different than the seed frequency. As the fiber becomes longer and longer the peaks broaden and form a supercontinuum. However we do not want the fiber to be longer than necessary, because the longer it is, the more dispersion the white light experiences as it travels inside the fiber and the more chirped the pulse becomes. We measured the spectra of white light generated through the 130-cm long fiber and a 90-cm long fiber, identical in every other aspect with each other. The result is shown in Figure 3.11. We observe that the two spectra look almost identical and the 90-cm spectrum looks more intense although this is probably a result of applying a more intense seed or positioning the detector better. Therefore, in our case it would be best to use the 90 cm fiber. Of course it would be best to find the minimum length required to produce the

white light we need but there is no non-destructive way to determine the optimum length.
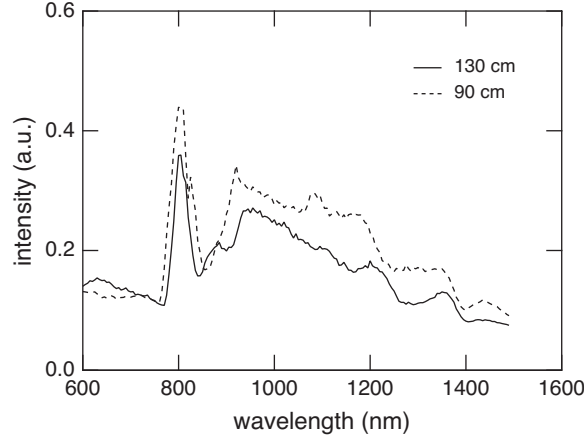
Figure 3.11: White-light spectra generated by a 130-cm (solid line) and a 90-cm (dashed line) photonic crystal fiber.

Another feature to investigate is the dependence of the white light spectrum on the duration of the seed pulse. Because white light generation is a nonlinear process it is expected to depend critically on the intensity of the electric field. By changing the duration of the seed pulse we change the intensity and therefore we expect to reach the threshold for white light generation. We are able to vary the duration of the seed pulse by using the compressor in our laser system. Our laser system has a grating compressor which follows the amplifier [77]. The reason for this compressor is that we stretch the oscillator pulse before we send it in the multipass amplifier in order to avoid very high intensities during the amplification stage that could damage the Ti:sapphire crystal and the optics of the amplifier. This technique is called chirped pulse amplification [78, 79] and it is very common in amplified laser systems. Therefore after the beam has been amplified in energy and it exits the amplifier cavity it goes through a grating compressor that compresses it as much as possible before letting it exit the laser system. By varying the distance between the gratings in the grating compressor we can vary the chirp of the output pulse and therefore

increase or decrease its duration in time. The result of this investigation is shown in Figure 3.12. In this Figure we show white light spectra generated in the same photonic crystal fiber with a seed pulse of 68 fs (solid line) and 926 fs (dashed line). The output spectrum seems insensitive to the duration of the seed pulse, at least in the subpicosecond regime. This finding indicates that for subpicosecond pulses we are still well above the threshold for white light generation.
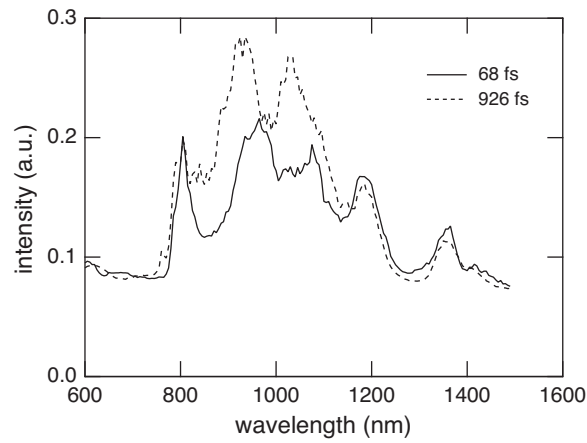
Figure 3.12: White-light spectra obtained by the same photonic crystal fiber using seed pulses of 68 fs (solid line) and 926 fs (dashed line) durations.

The two sources of white light that we use in our setup are suitable for spectroscopic measurements in multi-shot experiments. In such experiments, where the process under study is reversible, the material relaxes back to the equilibrium state between two pump pulses, which arrive on the medium surface every 1 ms. Therefore, there is no need to translate the sample between different shots and we can repeat the same measurement for many different shots and average, thus reducing the experimental noise. In this case both the photonic crystal fiber and the CaF_2 produce white light which is steady enough to serve as a probe. When the process under study is irreversible, however, the sample must be translated between different shots and we are obliged to take single-shot data or, due to

sample surface limitation, to average over a very small number of shots. In the single shot configuration the photonic crystal fiber proves to be quite unstable and the shot-to-shot fluctuations reach 10% of the signal level, which prohibits the observation of the material dynamics. Therefore, for single-shot measurements, CaF_2 is the only acceptable white light source we have. The data is this thesis had to be single-shot because the solid-to-liquid phase transition is an irreversible process. For this reason we used CaF_2 as a white light source.

3.2 Dual-angle reflectometry method

3.2.1 Measuring absolute reflectivity

As we already mentioned our setup is a reflectivity pump-probe setup. Therefore it is important to be able to measure absolute reflectivities. Many reflectivity experiments measure normalized reflectivity, meaning they only report relative changes of the reflectivity of the material after photoexcitation, with respect to the unexcited reflectivity, which they arbitrarily take as 1. We prefer to measure the absolute reflectivity, for example rather than assuming that the unexcited p-reflectivity of aluminum at 800 nm and for an angle of incidence of 68° is 1, to actually measure that it is 0.71 (or 71%). Measuring absolute reflectivity renders our experimental findings comparable to other studies and practical applications and it also allows us to convert reflectivity to dielectric function, as we will show below.

The conceptually simplest way of measuring the absolute reflectivity of a material is to measure the intensity of the incident beam, then the intensity of the reflected beam and then divide one by another. However, in experiments that involve pulsed sources of light this is impossible. If we measure the intensity of the incident pulse we block it, so we will

never be able to measure the intensity of the same pulse after reflection. One way around this is to measure different incident and reflected pulses but given that our white light probe suffers from pulse-to-pulse intensity fluctuations our measurement would be affected and the result would be wrong. Therefore we developed a technique which uses the reference beam.

As we mentioned in section 3.1.2, before the white light probe reaches the sample we split it into the reference beam, which goes around the sample, and the reflected beam, which we let reflect off the sample. This way we obtain two copies of the same pulse, since the splitting occurs for each pulse contained in the white light. If we denote by $I_{inc}(\omega)$ the intensity of the incident white-light pulse, before we split it to a reference and a reflected pulse, and by $I_{refer}(\omega)$ and $I_{refl}(\omega)$ the intensities of the reference and the reflected pulses, respectively, then we can write $I_{refer}(\omega) = a(\omega)I_{inc}(\omega)$ and $I_{refl}(\omega) = b(\omega)I_{inc}(\omega)$. The incident pulse is split by a sapphire crystal so $a(\omega)$ and $b(\omega)$ are essentially the reflectivity and transmissivity of the sapphire crystal, respectively. The reference pulse goes through a set of mirrors and lenses before it reaches the spectrometer, therefore its intensity is modified by the reflectivity and transmissivity of all these optics. The result of this modification can be cast into a multiplicative factor $g(\omega)$. Therefore the intensity (or spectrum) of the reference pulse that we measure with the spectrometer is $S_{refer}(\omega) = a(\omega)g(\omega)I_{inc}(\omega)$. The reflected pulse has to go through a set of optics and acquires a multiplicative factor $h_1(\omega)$, then it reflects off the sample and its intensity is further modified by the (absolute) reflectivity of the sample, $R(\omega)$, and finally it goes through another set of optics, before reaching the detector, acquiring another multiplicative factor $h_2(\omega)$. Therefore, the intensity, or spectrum, of the reflected pulse as measured by the detector is $S_{refl}(\omega) = b(\omega)h_1(\omega)h_2(\omega)I_{inc}(\omega)$. By taking the ratio of the reflected and reference spectra we essentially calculate

$$\frac{S_{refl}}{S_{refer}} = \frac{b(\omega)h_1(\omega)h_2(\omega)}{a(\omega)g(\omega)}R(\omega). \tag{3.11}$$

The quantity we want to measure is the absolute reflectivity of the sample, $R(\omega)$. In order to extract the absolute reflectivity, we need to determine the value of the fraction that multiplies it in Eq. 3.11, which for simplicity we call correction factor, CF. Therefore $CF = \frac{b(\omega)h_1(\omega)h_2(\omega)}{a(\omega)g(\omega)}$. The correction factor is independent of the sample under investigation and depends only on the piece of sapphire and the optics that build the beam paths. Therefore, if we replace our sample with another sample of known reflectivity, $R_1(\omega)$, and for the new sample we measure the spectra $S_{refl,1}$ and $S_{refer,1}$, we can calculate the CF by

$$CF = \frac{S_{refl,1}}{S_{refer,1}}\frac{1}{R_1(\omega)}. \tag{3.12}$$

In practice we use more than one calibration samples of known reflectivity to calculate the CF in order to minimize the error of the calibration. We align each of the calibration samples to the original sample using a HeNe alignment beam. Using more than one calibration samples allows us to calculate not only the CF, but also the angle of incidence of the probe and the thickness of an oxide layer that is possibly present on the sample under investigation. The way we calculate the angle is the following: we note that in order to use Eq. 3.12 correctly we need to know the value of the reflectivity of each calibration sample. However the reflectivity is a quantity that depends on the angle of incidence. Therefore, only when we calculate the CF using the correct angle of incidence will all the calibration samples yield the same result. This way, by using multiple calibration samples and then trying different values for the angle of incidence we can determine the experimental angle of incidence as the angle that minimizes the discrepancy between the CFs given by the different calibration samples. This method allows us to determine the angle of incidence in our setup with an accuracy of $\pm 0.1°$. In Figure 3.13 we show the result of using Al, Si, and

GaAs as calibration materials. Figure 3.13(a) shows that the CFs agree very well when we assume that the angle of incidence is 58.9°, while Figure 3.13(b) shows that if we assume an angle of incidence of 58° the CFs agree less well. Therefore we choose 58.9° to be the angle of incidence of our setup.
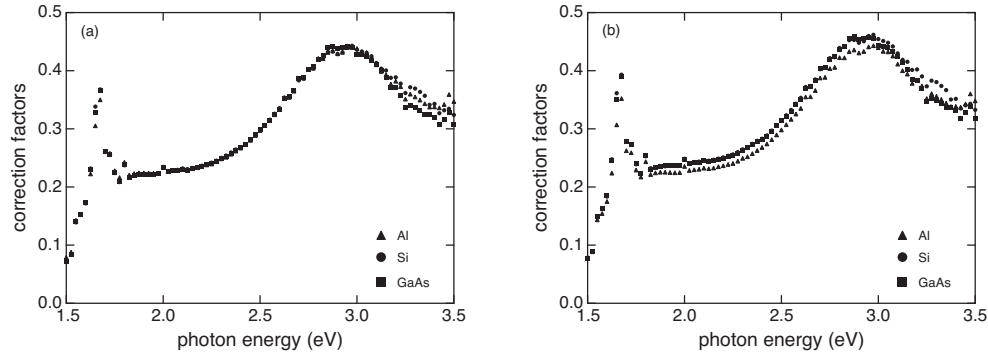
Figure 3.13: Correction factors taken using Al, Si, and GaAs as calibration materials and assuming an angle of incidence of (a) 58.9° and (b) 58°.

In a similar way we can use the oxide thickness of the sample as a free parameter and try to find the value that minimizes the discrepancy between CFs determined by a set of materials, one of which is the material with the oxide. In general we need to use as many calibration materials as the parameters we want to determine, meaning the CF, the angle, the oxide layer, etc.

3.2.2 Extracting the dielectric function

Once we calibrate our setup to measure absolute reflectivities, we can use the reflectivity data to extract dielectric function values. By using the Fresnel equations 2.53 and 2.55 we convert reflectivity to dielectric function. In our case the white light probe is *p*-polarized so we only need Eq. 2.53, keeping in mind that what we measure in the lab is the power reflectivity, $R = |r_p|^2$. From Eq. 2.53 it appears that having measured the reflectivity $R(\omega)$ and knowing the angle of incidence by matching the CFs, we should

be able to calculate the dielectric function for each of the frequencies of the white light. However there is a small complication since the dielectric function is a complex quantity. For this reason we need two independent sets of measurements. One combination could be to take one s and one p-polarized reflectivity measurements, however it is more favorable for error minimization to take two p-reflectivity measurements at two different angles of incidence [60]. The sample holder, shown in Figure 3.3, is mounted on a rotation stage, so by rotating the sample we can change the angle of incidence of the experiment.

Performing the experiment twice in order to determine the dielectric function has fundamental advantages. The dielectric function is a much more intrinsic property of the material than the reflectivity. Knowing the dielectric function we can calculate all the optical properties of the material, such as reflectivity, transmissivity, index of refraction, extinction coefficient, and skin depth, using Eqs. 2.53 – 2.56, 2.38 – 2.39, and 2.44. Moreover, we can also calculate electrical properties such as the electrical conductivity using Eq. 2.23. Finally, using the Drude and Lorentz models described in chapter 2 and knowing the shape of the dielectric function we can derive conclusions about the band structure, or the lattice and electronic configuration of the material. This is particularly useful for phase transition experiments where we expect to resolve semiconductor-to-metal, or crystalline-to-amorphous, or solid-to-liquid phase transitions, which are accompanied by big changes in the band structure and microscopic properties of the medium.

The Fresnel equations cannot be solved analytically in order to convert reflectivity to dielectric function. We need to invert them using an optimization routine, which returns the dielectric function values that minimize the error between experimental and calculated reflectivity. The routine we use is the simplex downhill method [80], which is the only multi-dimensional optimization routine[1] that does not make use of derivatives, thus running faster

---

[1]We are optimizing for the real and imaginary parts of the dielectric function simultaneously.

than other routines. The inversion from reflectivity to dielectric function will propagate the experimental error in measuring the reflectivity to dielectric function error. It proves that the choice of the angle of incidence and polarization of the white-light probe affects the error propagation significantly.

In the most general case we can assume that the functional relationship between dielectric function and reflectivity is $R = f(\epsilon, \theta)$. If the experimental error in measuring the reflectivity at two different angles of incidence is $\Delta R(\theta_1)$ and $\Delta R(\theta_2)$, then the error in calculating the dielectric function is

$$\begin{pmatrix} \Delta R(\theta_1) \\ \Delta R(\theta_2) \end{pmatrix} = \mathbf{J} \begin{pmatrix} \Delta \epsilon_1 \\ \Delta \epsilon_2 \end{pmatrix}, \tag{3.13}$$

where

$$\mathbf{J} = \begin{bmatrix} \frac{\partial f(\theta_1)}{\partial \epsilon_1} & \frac{\partial f(\theta_1)}{\partial \epsilon_2} \\ \frac{\partial f(\theta_2)}{\partial \epsilon_1} & \frac{\partial f(\theta_2)}{\partial \epsilon_2} \end{bmatrix}, \tag{3.14}$$

is a Jacobian matrix and ϵ_1, ϵ_2 are the real and imaginary parts of the dielectric function, respectively. In order to calculate the dielectric function error we need to invert the Jacobian,

$$\begin{pmatrix} \Delta \epsilon_1 \\ \Delta \epsilon_2 \end{pmatrix} = \mathbf{J}^{-1} \begin{pmatrix} \Delta R(\theta_1) \\ \Delta R(\theta_2) \end{pmatrix}. \tag{3.15}$$

In order to understand the effect of the angle of incidence and probe polarization on the inversion error, we can consider Figure 3.14. Figure 3.14(a) shows a grid of dielectric function values with the dielectric function of four different materials superimposed on it. Figure 3.14(b) shows the obtained reflectivity values, if we replace each one of the grid points in Figure 3.14(a) in the Fresnel equations 2.53 and 2.55, assuming a 45° angle of incidence and s-polarized light (horizontal axis) or a 45° angle of incidence and p-polarized

light (vertical axis). We observe that many different dielectric function values collapse onto similar reflectivity values. This would be a poor experimental choice because in trying to invert the reflectivity values of Figure 3.14(b) we wouldn't be able to distinguish between different dielectric function values, and the inversion error would be big. Figure 3.14(c) shows the same thing as Figure 3.14(b) but this time on the horizontal axis we plot p-reflectivity calculated at $45°$ and on the vertical axis we plot p-reflectivity calculated at $60°$. The result is slightly better, meaning that the spread in the reflectivity values is bigger than in Figure 3.14(b). This indicates that taking two measurements at two different angles of incidence with p-polarized light produces less error than taking two measurements at the same angle of incidence but with different polarizations. In an effort to make the reflectivity spread even better we show in Figure 3.14(d) the calculations for p-reflectivity at $45°$ and $75°$, which correspond to the grid of points of Figure 3.14(a). We observe that as the second angle increases the spread becomes bigger, thus making it easier to match measured reflectivity with dielectric function values. Increasing the second angle even more, as in Figure 3.14(g), the spread becomes even better.

We can calculate the inversion error using Eq. 3.15 and replacing the functional relation with the Fresnel equations. Figures 3.14(e) and 3.14(f) show the result of this error calculation assuming that we take two p-reflectivity measurements, one at $45°$ and one at $75°$, as shown in Figure 3.14(d), with 1% error each. Figure 3.14(e) shows the error for the real part of the dielectric function for each of the grid points in Figure 3.14(a), while Figure 3.14(f) shows the corresponding error for the imaginary part of the dielectric function. We observe that if we were to use these conditions to measure the dielectric function of any of the four materials shown in the Figure, the error would be less than 10%. The error becomes smaller for the conditions of Figure 3.14(g), as we expect from the bigger spread in the reflectivity values. Figures 3.14(h) and 3.14(i) show the error in the real and
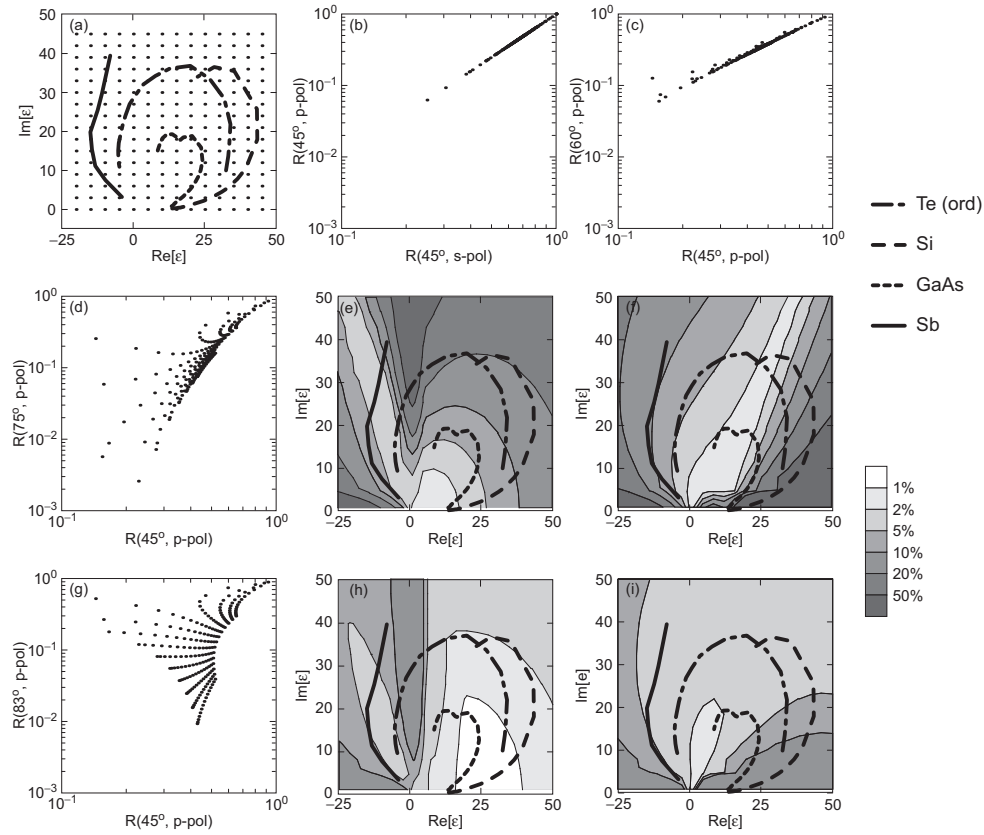
Figure 3.14: (a) The dielectric functions of Si, GaAs, Sb, and Te (from 1.5 to 3.5 eV) are plotted over a grid of dielectric constant values. In (b), (c), (d), and (g), the Fresnel formulas are used to calculate reflectivity pairs at the angles and polarizations indicated for each of the points in (a). In (e) and (f), contour plots represent the uncertainty in extracting $Re[\epsilon(\omega)]$ and $Im[\epsilon(\omega)]$, respectively, given a 1% error in measuring the reflectivity for the parameters indicated in (d). Plots (h) and (i) are analogous to (e) and (f), but are calculated for the parameters indicated in (g). In all four contour plots, the representative materials are overlaid as a reference.

imaginary part of the dielectric function given a 1% error in the reflectivity measurements indicated in Figure 3.14(g). We observe that now the error for any of the four materials under consideration is less than 5%. As a rule of thumb we mention that the sensitivity of reflectivity measurements to changes of the dielectric function increases as the angle of incidence approaches the Brewster angle of the material [81]. We want to note that Figure 3.14 is a correction to a similar figure published in [60]. In particular, parts (e), (f), (h),

and (i) are corrected in Figure 3.14.

In the following section we present reflectivity and dielectric function measurements we performed on semiconductors, where we monitored the evolution of the reflectivity or the dielectric function after photoexcitation of the material with an intense laser pulse, with femtosecond time resolution.

3.3 Dielectric function dynamics

During the past three years, we have investigated ultrafast laser-induced dynamics and optical control in Te and Ti_2O_3 [61, 82], using the dual-angle reflectometry technique described above. Taken as a whole, our extensive body of work in this area reveals the importance of the electron-hole plasma and lattice dynamics in band gap renormalization of highly excited semiconductors and allows for the realization of optical control schemes.

3.3.1 Subpicosecond band gap renormalization in Te

The crystal structure of Te allows for optical excitation of coherent phonons in the bulk. The displacive excitation of coherent phonons (DECP) allows symmetry preserving phonon modes to be excited coherently when a laser pulse shorter than the phonon period is incident on the material [83]. Previous investigators observed oscillatory behavior in the transient reflectivity and attributed this signal to DECP [84, 85]. While single-color reflectivity transients indicate the presence of coherent phonons, our technique for measuring the time-resolved dielectric function provides a direct view of the material at different lattice displacements. Figure 3.15, for example, shows the transient behavior of the real part of $\epsilon_{ord}(\omega)$ of Te for an excitation of 9 J/m^2.

After excitation of coherent phonons, the bulk optical properties oscillate at the phonon frequency and move toward lower photon energies with increasing displacement of
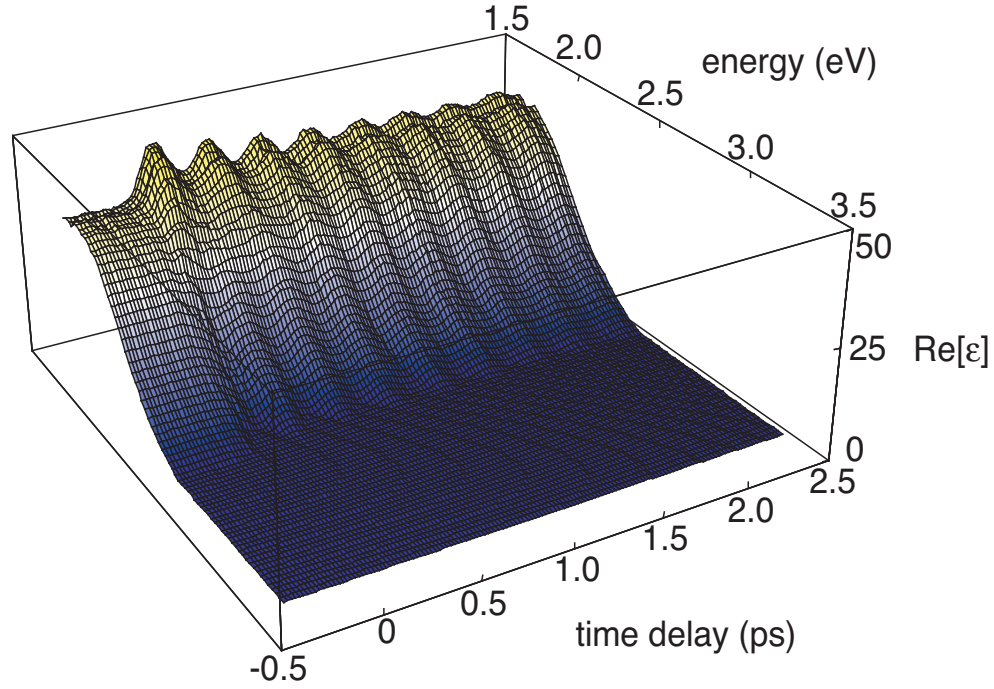
Figure 3.15: Temporal evolution of the real part of the ordinary dielectric function of Te for a pump fluence F = 9 J/m^2.

the lattice from its initial position. Theory predicts that lattice displacements along the symmetry preserving A$_1$ phonon mode on the band structure of Te modulate the material's indirect band gap [86]. Coupled with theoretical results, which model the phonon-induced band gap renormalization in terms of the electronic excitation, our data allow the determination of interband and intraband optical deformation potentials in Te [87]. Interband and intraband deformation potentials stand respectively for the diagonal and off diagonal matrix elements of the relevant optical deformation potentials that describe band gap renormalization in a first order perturbation theory applied on the Frölich Hamiltonian [87].

3.3.2   Optical control of coherent lattice vibrations in Te

We demonstrated optical control of large amplitude coherent phonons in tellurium using a two-pulse excitation scheme [61]. Time-resolved dielectric tensor measurements reveal both the cancellation of lattice oscillations by the second excitation pulse as well as a red-shift of the main resonance of the material as a result of the lattice displacement. Coupled with theoretical band structure calculations, the data provide an estimate of the size of the lattice displacement as well as the magnitude of the single-pulse-induced lattice vibration. The data also indicate a departure from the semiclassical mass-and-spring picture of the lattice dynamics observed under weak excitation [88].

Figure 3.16 shows the changes in the resonance energy of the material obtained from fits to $\epsilon_o(\omega)$ and $\epsilon_e(\omega)$ under various single and double pulse excitation conditions. In all parts, pump pulses 1 and 2 (and 3) indicate their time of arrival and their 35-fs pulse duration is drawn to scale. In Figure 3.16(a), the variation in the resonance energy in $\epsilon_o(\omega)$ is shown under single and double pulse excitation, the latter with a pulse separation of 133 fs. The data show that this double pulse combination leads to cancellation of the coherent phonons. The cancellation of oscillations in the $\epsilon_e(\omega)$ data is shown in parts (b) and (c) under different excitation conditions. Figure 3.16(b) shows single pulse oscillations, double pulse cancellation, and double pulse enhancement of the oscillations. For cancellation, the time delay between pump pulses is 127 fs, while for maximum enhancement the time delay is 267 fs. Figure 3.16(c) shows cancellation at the first maximum as well as at the second maximum, both leading to roughly the same lattice displacement for different excitations.

In contrast to data obtained at low excitation [88], our experiments reveal that under strong excitation the vibrations do not stop at the maximum displacement. The 127 fs and 133 fs time delays that achieve cancellation as shown in Figure 3.16 do not coincide with the time to reach the maximum displacement in the single pump case, which
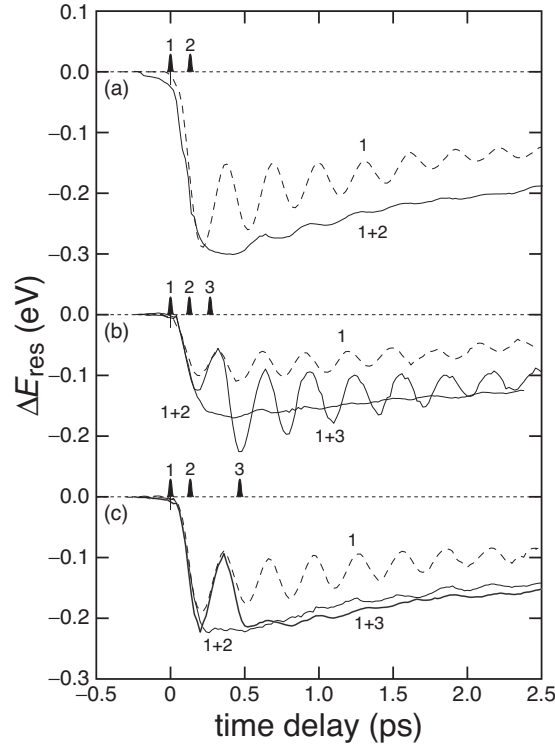
Figure 3.16: Transient behavior of the main resonance energy. (a) Pump pulses 1 and 2 lead to cancellation of the oscillations at the first peak. By varying the time delay between the two pump pulses, enhancement (b, 1+3) or cancellation at later peaks (c, 1+3) can be achieved.

is approximately 220 fs. Similar results occur in bismuth under strong excitation, where a 500 fs delay between pump pulses cancelled the lattice vibrations near the second maximum, while the second maximum is reached 600 fs after single pulse excitation [89], but the authors do not comment on the discrepancy. Our dielectric tensor data reveal that the resonance energy red-shifts beyond the single pump maximum for phonon-canceling excitations, as shown in Figure 3.16. Thus, in addition to the delay between pulses being different from their expected values, the nuclei do not stop their coherent oscillations at the classical turning point, which is also different from the low-excitation strength behavior of other materials [88]. The fact that the second pump pulse causes the ions to move past the classical

turning point without resulting in oscillations indicates a departure from the classical model of the impulsively driven mass-spring system. This is a manifestation of a time-dependent driving term, *i.e.*, the carrier-lattice coupling through the deformation potential changes over time. The physical origin of such a phenomenon would likely involve many body effects, such as a deformation coupling that changes with lattice configuration. A sufficiently large displacement of the lattice may allow the excited electrons to redistribute in such as way as to further perturb the lattice equilibrium position. In this way, the lattice essentially pulls the equilibrium position along until it costs too much energy to displace the lattice further, at which point the expansion stops and the lattice slowly returns to its unexcited configuration.

3.3.3   Semiconductor-to-semimetal phase transition in Ti_2O_3

Currently, we are conducting coherent control experiments on Ti_2O_3. Ti_2O_3 is similar to Te in that photoexcitation leads to changes in the lattice configuration. The lattice distortion necessary to achieve a semiconductor-semimetal transition is smaller in Ti_2O_3 than in Te. For this reason, we believe that it will be possible to drive Ti_2O_3 to its semi-metallic state without permanently damaging the sample, which we cannot do in the case of Te. Figure 3.17 shows preliminary data on large amplitude reflectivity oscillations induced in Ti_2O_3 through the photoexcitation of its A1- phonon mode through the DECP mechanism. Because Ti_2O_3 has a very narrow band gap, the resonance of its dielectric function lies in the near-IR. Therefore, the most suitable white-light source for the completion of this experiment is the photonic crystal fiber.
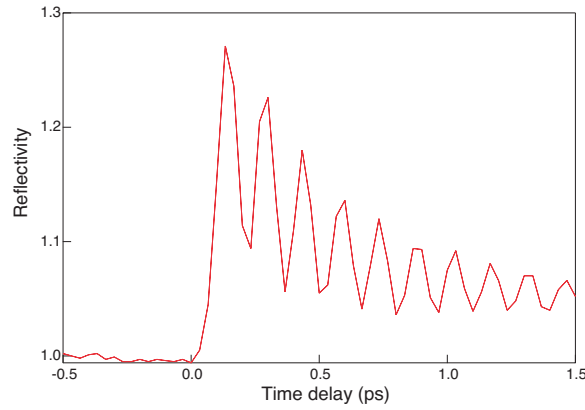
Figure 3.17: Large amplitude reflectivity oscillations in Ti_2O_3 induced by intense photoexcitation.

3.4 Differences between semiconductors and metals

In the previous section we demonstrated that the technique of dual-angle reflectometry and inversion to dielectric function works successfully in the case of semiconductors and provides lots of insight about the evolution of the material properties under photoexcitation. However, in the case of metals, error propagation renders the inversion of the Fresnel equations invalid. The reason is that in metals a wide range of dielectric function values collapses onto a very small range of reflectivity values, meaning that the experimental uncertainty in the measured reflectivity will translate into a large uncertainty in the dielectric function after the inversion.

The difference between semiconductors and metals lies in the sign of the real part of the dielectric function. Figure 3.18(a) shows a grid of dielectric function values, where both the real and the imaginary parts of the dielectric function are taken to be positive. This is often the case for semiconductors like Si, the dielectric function of which (from 1.7 to 3.5 eV) we superimpose on Figure 3.18(a). When two reflectivity measurements are taken with p-polarized light at different angles of incidence, the uncertainty in extracting the dielectric

function can be reduced to reasonable levels of 1-2%, as shown in section 3.2.2. Figure 3.18(b) shows the mapping of the grid of dielectric function values into reflectivity space for the angles of incidence used in our aluminum experiment, *i.e.*, 58° paired with 68°. As the second angle is increased, the grid of points in (a) spreads over a larger range of reflectivities because the pseudo-Brewster angle is approached for many of the dielectric function values. Figure 3.18(c) shows a grid of dielectric function values where now the real part of the dielectric function is taken to be negative, as is often the case for metals like aluminum, the dielectric function of which (from 1.7 to 3.5 eV) we show in Figure 3.18(c). Figure 3.18(d) shows the mapping of the grid of dielectric function values into reflectivity space for 58° angle of incidence paired with 68°. We see that for metals the result is quite different than for semiconductors: the reflectivity remains constant for many different dielectric function values. Because there would be too much uncertainty in the inversion of reflectivity to dielectric function, we choose to present our data on the solid-to-liquid phase transition of aluminum as reflectivity data in order to guarantee the validity of our conclusions.

For dielectric function measurements in metals ellipsometry seems more suitable than reflectometry [90, 91]. In ellipsometry, reflectivity data are taken at a fixed angle of incidence while the polarization of the incident light varies continuously. By measuring the change in the ellipticity of the reflected light , which depends on the ratio of the p- to the s-reflectivity of the material, we are able to determine the optical properties of the material under study. However, femtosecond time-resolved ellipsometry is far more complicated and not commonly used as an experimental technique.
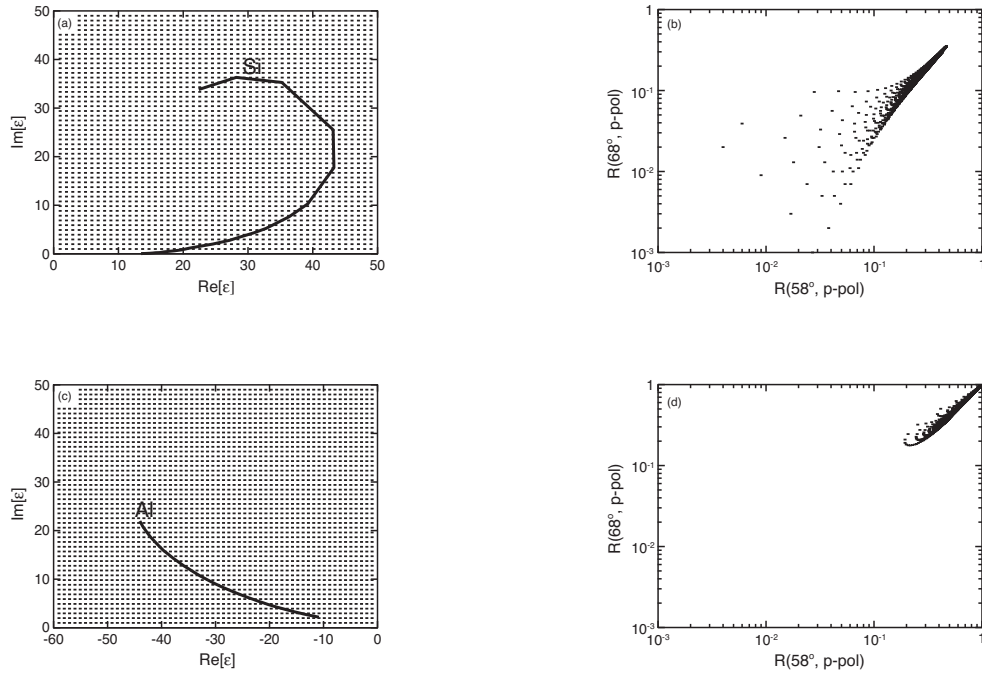
Figure 3.18: (a) The dielectric function of Si (from 1.7 to 3.5 eV) is plotted over a grid of dielectric function values with positive real and imaginary parts. In (b) the Fresnel formulas are used to calculate reflectivity pairs at the angles and polarizations indicated for each of the points in (a). (c) The dielectric function of Al (from 1.7 to 3.5 eV) is plotted over a grid of dielectric function values with negative real parts. In (d) the Fresnel formulas are used to calculate reflectivity pairs at the angles and polarizations indicated for each of the points in (c).

3.5   Summary

The optical pump-probe technique is one of the most valuable methods to study time-resolved dynamics following laser excitation of materials, and it can be accomplished though numerous configurations, including reflectivity or transmissivity measurements. We developed a variation of the reflectivity pump-probe setup, which provides spectral, in addition to temporal, information. This expansion allows for unambiguous interpretation of the observed dynamics and for inversion of the reflectivity data to dielectric function results. Dielectric function is an intrinsic property of a material and it offers fundamental

advantages as a subject of study. Our results on optical excitation and control of coherent oscillations in semiconductors illustrate the capabilities of our technique. Even though inversion of reflectivity to dielectric function is not favorable for the study of metals, the broadband nature of our reflectivity measurements still offers valuable insight in the study of the solid-to-liquid phase transition of aluminum, which we will present in chapter 5.

Chapter 4

Previous work on Aluminum

In this chapter we discuss the structural and optical properties of aluminum in order to help the understanding of the data we present in the next chapter. Furthermore, we present the results of previous studies on the laser-induced, solid-to-liquid phase transition in aluminum. We highlight the discrepancies between the existing results and we proceed to address them in the next chapter.

4.1 Properties of aluminum

Aluminum is one of the most studied materials both theoretically and experimentally. It is easily machined and has excellent corrosion resistance and durability. Aluminum is used in myriads of applications losing the first place only to iron. Its applications range from aircraft and rocket manufacturing to household and telescope mirrors, cans and foil, construction units, electrical transmission lines, machinery, paint, weapons, glass making, rocket fuels and heat sinking in electronic devices. It is only natural that it has attracted a great deal of scientific attention and its properties are well known. Al is the 13th element in the periodic table and its electronic configuration in the ground state is [Ne] $3s^2$ $3p^1$.

Among all other properties, the optical properties of aluminum have attracted significant attention. As a result, the lattice structure, electronic configuration, band structure and dielectric function of the material are well known. In the following two sections we will give an overview of the structure and optical properties of solid and liquid aluminum before we go on to discuss the dynamics of the transition between the two phases.

4.1.1 Solid aluminum

Solid aluminum crystallizes in the face-centered cubic (fcc) Bravais lattice with one atom at each lattice site [6]. The lattice constant is $\alpha = 0.405$ nm. Aluminum is a trivalent metal, meaning that each atom contributes 3 valence (or conduction) electrons to the sea of electrons of the material. The Fermi energy of aluminum is 11.7 eV. The density of valence electrons in aluminum can be calculated easily in the same way that applies to all metals. A metallic element contains 0.6022×10^{24} atoms per mole (Avogadro's number) and ρ_m/A moles per cm^3, where ρ_m is the mass density and A is the atomic mass of the element. As we mentioned aluminum is a trivalent metal, so each atom contributes 3 valence electrons. As a result the density of valence electrons, $n = N/V$ is

$$n = 0.6022 \times 10^{24} \frac{3\rho_m}{A}. \tag{4.1}$$

For aluminum the density of valence electrons turns out to be 18.1×10^{22} cm^{-3}. This density, which is typical for a metal, is a thousand times greater than the density of a classical gas at normal temperatures and pressures. In photoexcitation experiments a significant portion of the valence electrons is excited by the laser pulses. The band structure of aluminum has been shown to be nearly free-electron-like [92]. The free-electron approximation neglects electron-ion interactions in metals and can serve as a rough model for a qualitative understanding of many metallic features, although it fails to explain some of

the experimental observations. For a more successful model, electron-electron and electron-ion interactions need to be taken into account. Polyvalent metals, such as aluminum, pose additional challenges in constructing a realistic potential to be used for band structure calculations. In studying alkalis, which are the simplest metals, one generally introduces the Wigner-Seitz assumption which is that the potential acting on the electron is that due to the ion core within the cell [6]. However, in the case of a polyvalent material, the fields that act on a valence electron depend in an important way on the distribution of the other valence electrons, and since the valence wave functions are significantly different in the solid than they are in the free atom, the previously mentioned simplicity does not exist. Figure 4.1 shows calculated valence bands for aluminum (solid lines) compared with free-electron bands (dashed lines).
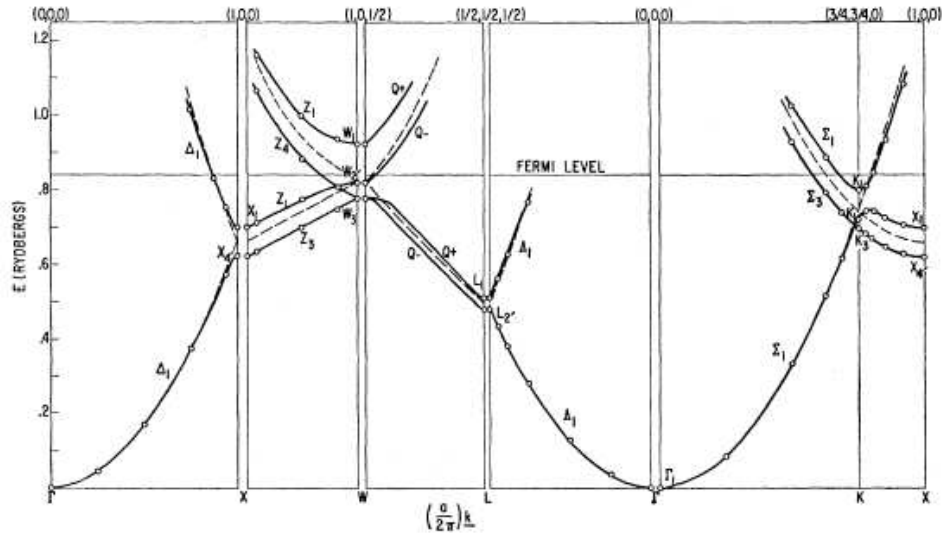

Figure 4.1: Calculated band structure of aluminum (solid lines). Dashed lines: free-electron band structure. After Ref. [92].

The calculated bands agree very well with the free-electron bands, supporting the statement that aluminum is a nearly free-electron metal. The only difference arising from

taking into account the electron-ion interactions (solid lines) is the splitting of degenerate bands.

A more detailed band structure calculation was presented by Ehrenreich *et al.* [93] who proceeded to connect the band structure with reflectivity and dielectric function measurements on aluminum. Figure 4.2 shows the result of their calculation.
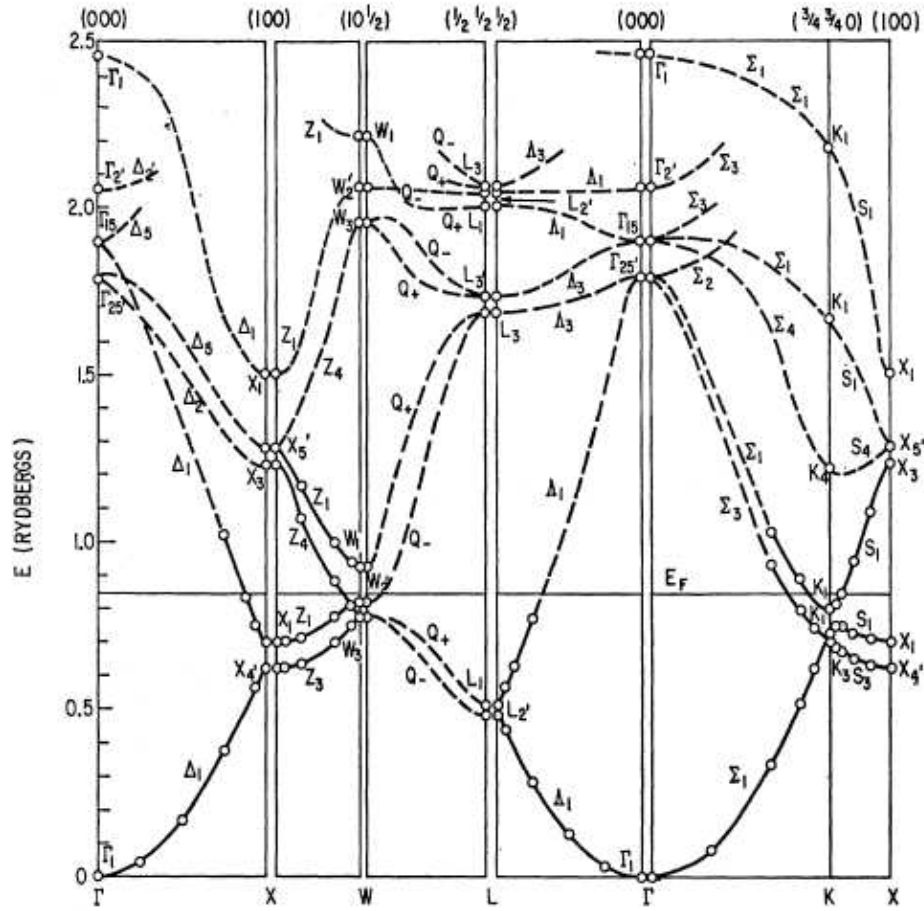

Figure 4.2: Calculated band structure of aluminum. After Ref. [93].

This calculation includes symmetry point eigenvalues up to 2.4 Ry, while the calculation in Figure 4.1 stops at 1.2 Ry. The first thing to observe from Figure 4.2 is that the

free-electron-like behavior persists in the higher energy range where the energy bands are still nearly parabolic. Another feature that manifests itself in the optical properties of the material is the existence of parallel bands that give rise to interband electronic transitions that dominate the optical response of aluminum in certain photon energies. Specifically, the authors find that interband electronic transitions between the occupied state $W_{2'}$ and the unoccupied state W_1 as well as transitions between the states Σ_3 and Σ_1 contribute significantly to the imaginary part of the dielectric function of aluminum. The calculated transition energies are 1.41 eV. The same calculations predict that allowed higher energy transitions set in at about 8 eV and above. The dielectric function of aluminum, however, exhibits no structure in this range as we shall see below. The absence of an optical feature at this energy is explained by the fact that the peak value of the contribution from a transition point in the band structure is proportional to $E_g^{-3/2}$, where E_g is the energy gap of the transition. Therefore, the numerous transitions at still higher energies would certainly be unimportant and it is the transitions around 1.41 eV that dominate the optical response of aluminum.

The dielectric function of aluminum has been studied through various experiments in the past and the most accurate results [91] appear in Figure 4.3.

The most prominent feature of the dielectric function is the resonance around 1.55 eV. We observe that the imaginary part peaks at this photon energy while the real part presents a Kramers-Kronig consistent inflexion. This feature arises from interband electronic transitions due to the parallel band structure of aluminum around the W point and the Σ axis as we discussed earlier. The discrepancy between the 1.55 eV value that appears to be the center of the resonance in the experimental data and the 1.41 eV value of the theoretically calculated energy gap between the electronic transitions that contribute to the optical feature is probably due to simplifying assumptions followed in the theoretical
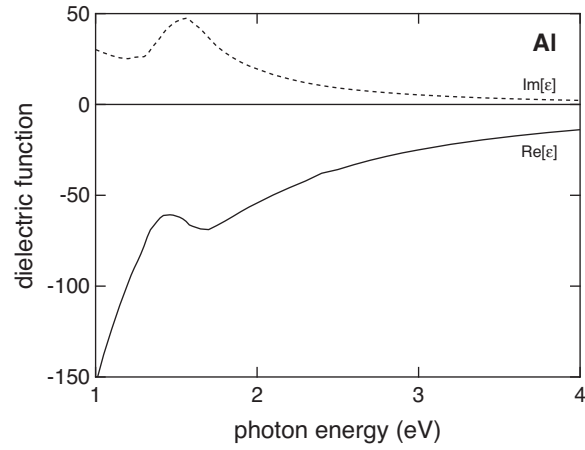
Figure 4.3: Dielectric function of solid aluminum. Dashed line: imaginary part. Solid line: real part.

calculations. A peak in the imaginary part of the dielectric function corresponds to enhanced absorption of light with photon energy of 1.55 eV. Indeed, if we calculate the reflectivity of aluminum using the Fresnel equations we observe that the reflectivity decreases around 1.55 eV, as shown in Figure 4.4.

Figure 4.4: *p*-reflectivity of solid aluminum calculated from the Fresnel equations at 68° angle of incidence.

This shape of the reflectivity of aluminum has been verified experimentally and

it is characteristic of the material. Due to the reduction in the reflectivity around 1.55 eV aluminum mirrors are not preferred for the IR and golden mirrors are used for demanding applications instead.

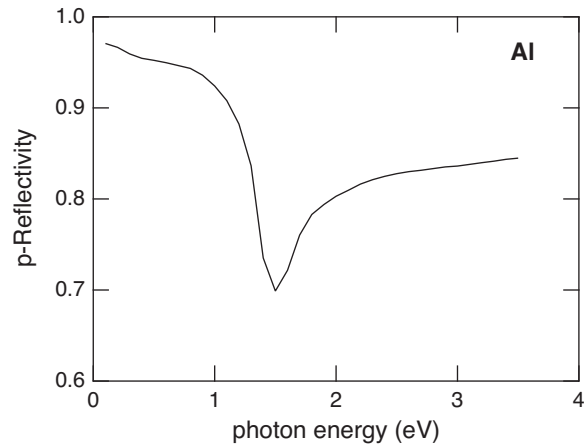## 4.1.2 Liquid aluminum

Although the optical properties of solid aluminum are well established, the optical properties of liquid aluminum have been studied much less and there are still controversies in the existing literature. The experimental challenge lies in the contamination of the samples from oxidization and requires conditions of ultra high vacuum for valid results.

The first one to report optical measurements on liquid aluminum is Miller [94] in a series of experiments where she used an ellipsometric method to study liquid metallic specimens. Aluminum was heated to 1173 K, which is above its melting temperature of 933 K, by a coil of molybdenum wire. Measurements were taken at a pressure of 10^{-1} Torr in order to prevent rapid oxidization of the heating element. The most important finding of this study was that the dielectric function of liquid aluminum shows no significant structure around 1.5 eV. The results were fitted with a Drude dielectric function, which takes into account only free-electron contributions and the result was reasonably good, although significant discrepancies were present. An attempt to improve the fitting by introducing an effective carrier density N* instead of the actual density N in Eq. 2.24 yielded unreasonable results for the effective carrier density and the author concludes "...the data may not, after all, represent the true optical properties of liquid Al in the bulk" [94].

The subject was revisited decades later by Havstad *et al.* [95], who built an apparatus to measure the optical constants and thermal radiative properties of liquid metals over a broad frequency range. The samples were contained in ultrahigh vacuum corresponding to a pressure of 10^{-10} Torr in order to minimize surface contamination. Optical measurements

were taken only after sulfur, carbon, or oxygen impurities were not detectable. Aluminum

was heated above the melting temperature and data were taken at 950 K, 990 K, and 1030
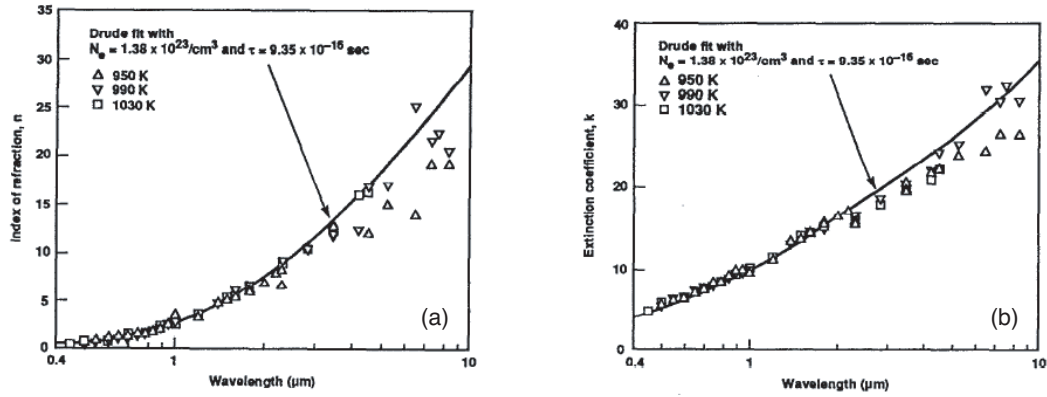
K. The results are shown in Figure 4.5.

Figure 4.5: (a) Index of refraction of liquid aluminum for different temperatures. Solid line: Drude fit. (b) Extinction coefficient of liquid aluminum for different temperatures. Solid line: Drude fit. After Ref. [95].

The first thing to note is the absence of any feature near the 1.55 eV (800 nm)

point, in agreement with Miller. According to these two studies the parallel bands in the

band structure of solid aluminum are no longer present in liquid aluminum due to loss of

long range order. Havstad *et al.* are able to fit their data with a Drude model (solid lines in

Figure 4.5). It is possible that Miller was not able to fit her data as well as Havstad *et al.*

because she didn't use ultrahigh vacuum conditions. She claims that at the temperature she

used the oxide layer on aluminum decomposes but apparently ultrahigh vacuum is needed

for reliable results.

Shortly after Havstad's results a new ellipsometric study appeared on the optical

properties of liquid aluminum, by Krishan and Nordine [96]. This time the claim was

that liquid aluminum maintains the interband feature of solid aluminum in the optical

properties. The authors eliminate oxides from the aluminum specimens by conducting the

optical measurements on electromagnetically levitated liquid aluminum and by heating the specimens to temperatures sufficient to vaporize oxides, decompose nitrides, and also reduce the oxygen and nitrogen content of the metal well below the solubility limits. Their results at 1550 K are shown in Figure 4.6.
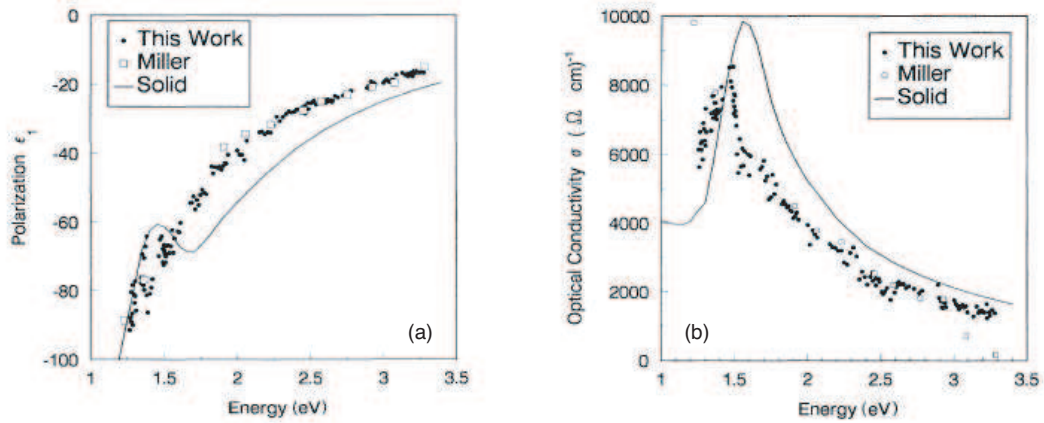

Figure 4.6: (a) Real part of the dielectric function of liquid aluminum at 1550 K. (b) Optical conductivity of liquid aluminum at 1550 K. After Ref. [96].

In the left panel the real part of the dielectric function of liquid aluminum is shown. In the right panel the authors report data on the optical conductivity, which is proportional to the imaginary part of the dielectric function (*cf.* Eq. 2.23). The most striking feature in these results is the presence of an absorption peak at 1.4 eV for the liquid, which is similar to the one found for the solid. The magnitude of the peak is similar to that for the solid, while its position is shifted to lower energy, as is also the case for solid aluminum at higher temperatures [97]. The authors attribute the persistence of the absorption peak to the existence of enough local order in the liquid state. This result is in disagreement with the previous results obtained by Miller and Havstad *et al.*, and Krishnan and Nordine attribute the discrepancy to contaminated specimens.

Krishnan and Nordine were able to take measurements at several temperatures

and this allowed them to follow the evolution of the optical constants of liquid aluminum as a function of temperature, as shown in Figure 4.7.
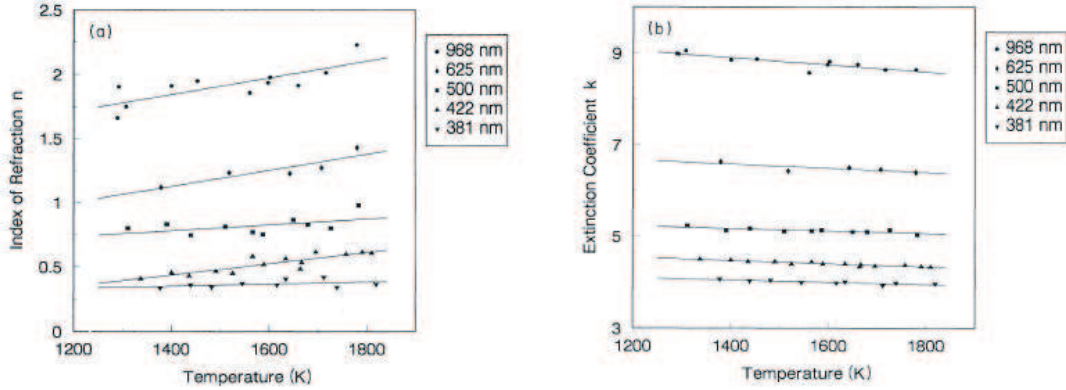

Figure 4.7: (a) Index of refraction of liquid aluminum as a function of temperature for different wavelengths. (b) Extinction coefficient of liquid aluminum as a function of temperature for different wavelengths. After Ref. [96].

In the Figure above the index of refraction is shown to increase with increasing temperature while the extinction coefficient is shown to decrease. These results are in agreement with our measurements on the reflectivity of liquid aluminum, as we will discuss in the next chapter.

The last and more recent experimental study on the optical properties of liquid aluminum was presented by Akashev and Kononenko in 2001 [98]. The authors performed ellipsometric measurements on liquid aluminum specimens and used a thermodesorption method to clean the material surface from oxides. The oxide film disappeared from the melt surface when they heated the specimen in a vacuum of 10^{-5} Pa to 1173 K. Their results agree more with the results of Miller and Havstad *et al.*, as shown in Figure 4.8.

The findings of Krishnan and Nordine are not reproduced in these results since there is no absorption peak present at the dielectric function. It seems once more that the dielectric function of liquid aluminum is that of a free-electron system without interband
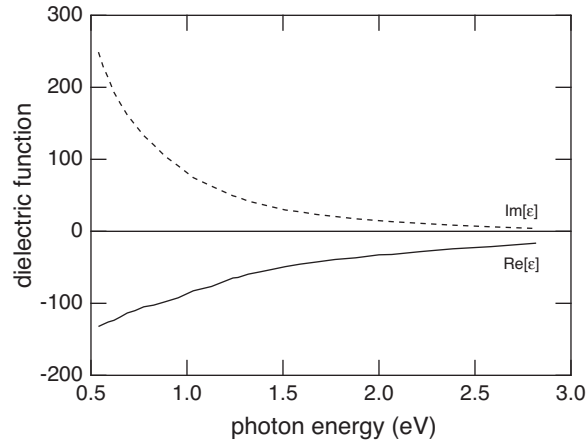
Figure 4.8: Dielectric function of liquid aluminum. After Ref. [98].

contributions.

The latest study that shed some light on the optical properties of liquid aluminum was the calculations performed by Benedict *et al.* [97] using an empirical pesudopotential technique. The authors find that the optical spectrum of liquid aluminum is Drude-like for all temperatures above the melting temperature, possessing no peak near 1.55 eV. Their results are shown in Figure 4.9.

In this Figure the imaginary part of the dielectric function, $\epsilon_2(\omega)$, is calculated for lattice temperatures below and above the melting temperature. The bold solid lines indicate $T = 0$ K, 750 K, and 950 K, with the $T = 0$ K line being the bottom one at 1 eV. The melting temperature of aluminum is 933 K. We observe that for temperatures up to 750 K the peak in the imaginary part of the dielectric function is clearly visible though its position is shifted to lower energies as the temperature increases. Just below the melt, at 900 K, the authors calculate a spectrum that looks quite featureless. For all temperatures above the melting temperature the calculated spectra look Drude-like, without any signs of interband contributions.
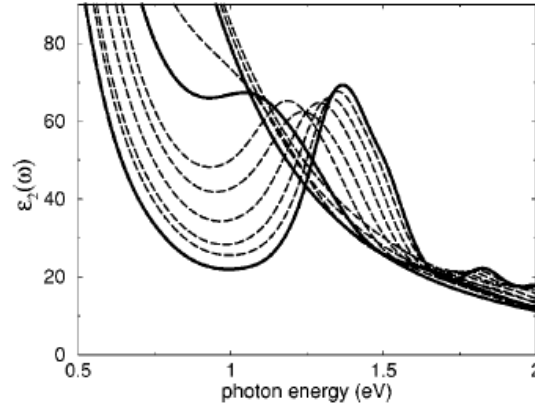
Figure 4.9: Calculated values for the imaginary part of the dielectric function of aluminum for $T = 0$ K, 100 K, 200 K, 300 K, 400 K, 550 K, 750 K, 900 K, 950 K, 1400 K, and 1800 K. Bold solid curves indicate $T = 0$ K, 750 K, and 950 K. For the purpose of identifying the curves, note that ϵ_2 is monotonically increasing with T at 1 eV. After Ref. [97].

Despite the controversies in the existing literature it seems that there is some agreement between the majority of researchers about the optical constants of liquid aluminum. This fact, combined with the well established optical properties of solid aluminum both from experimental and theoretical point of view, makes it safe to argue that aluminum is well-studied in both phases. The remaining question is how does the material pass from one state to another? As we will discuss below there is some controversy to be resolved about this question. In the rest of this chapter we will present the two major studies on this issue and we will highlight the discrepancies before we proceed to present our data in the next chapter.

4.2 An optical study of the solid-to-liquid phase transition in aluminum

In 2000, Guo *et al.* [22] did an optical pump-probe experiment on the solid-to-liquid phase transition in aluminum. They took time-resolved reflectivity data at 800 nm (1.55 eV) at two angles of incidence, and using the Fresnel equations they were able to convert the reflectivity data to dielectric constant dynamics. A schematic of their experimental setup is shown in Figure 4.10.
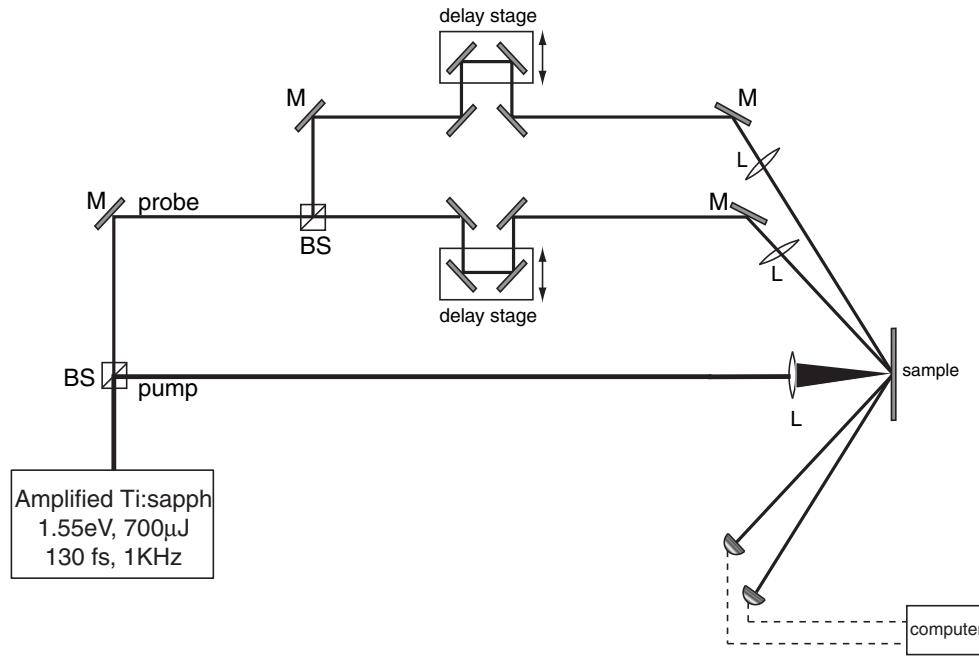

Figure 4.10: Schematic diagram of the setup of the optical pump-probe experiment of Guo *et al.* [22].

They used an amplified Ti:sapphire laser system with a central wavelength of 800 nm, producing 130-fs pulses. The laser output beam was further split into three different beams: the pump beam, which contains most of the energy of the initial beam, and two

probe beams which are much weaker than the pump in order to avoid probe-induced dynamics. Therefore in this experiment both the pump and the probes are centered around 800 nm. This is a particularly suitable wavelength since aluminum has a resonance in its optical properties at 800 nm. At this wavelength absorption is enhanced allowing for more effective coupling of light into the material. The pump beam is focused at normal incidence on the sample. The two probe beams are focused to an area ten times smaller than the pump in order to ensure probing of a homogeneously excited surface. The probe beams are incident on the sample at 47° and 58° and after reflection they are detected by two photodetectors. By varying the beam path between the pump and the probe beams the authors are able to measure the reflectivity for different time delays, either before the arrival of the pump –negative time delays– or after the arrival of the pump – positive time delays. The sample is translated between different shots, such that each pump pulse excites a fresh spot on the material's surface.

In order to study an irreversible phase transition such as a solid-to-liquid phase transition one has first to determine the damage threshold, that is the minimum incident laser fluence which induces irreversible changes in the material. The most usual way to do this is to illuminate the sample with laser pulses of increasing energy until a visible damage spot appears on the material's surface when the latter is examined under a microscope. Additionally to examining the surface under a microscope the authors employed reflectivity measurements in order to determine the damage threshold more accurately. Figure 4.11 shows changes in the reflectivity of aluminum induced by pump pulses of varying fluences. The reflectivities are recorded 2 ps and 10 ps after the arrival of the pump.

What we observe from Figure 4.11 is an increase in the probe reflectivity as the pump fluence varies up to 34 mJ/cm^2 and then, for fluences bigger than 34 mJ/cm^2, the reflectivity drops to a lower value and remains relatively unchanged as the pump fluence
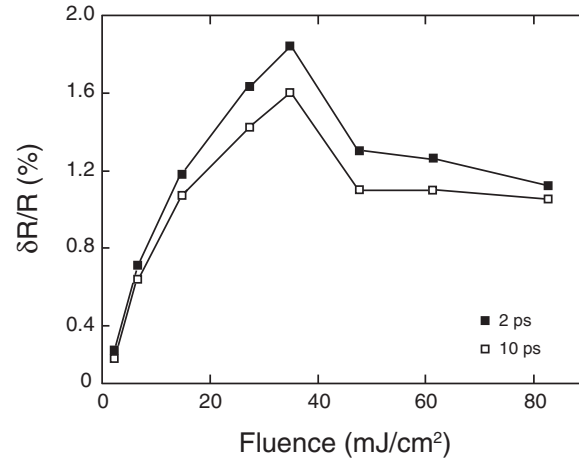
Figure 4.11: Normalized changes in the reflectivity of aluminum as a function of incident laser fluence 2 ps (solid squares) and 10 ps (open squares) after photoexcitation. After Ref. [22].

increases further. The increase in the probe reflectivity is due to transient bleaching created by the pump. Absorption of the 800-nm pump photons promotes a fraction of the material's electrons from the bottom to the top parallel band, as shown in Figure 4.12.
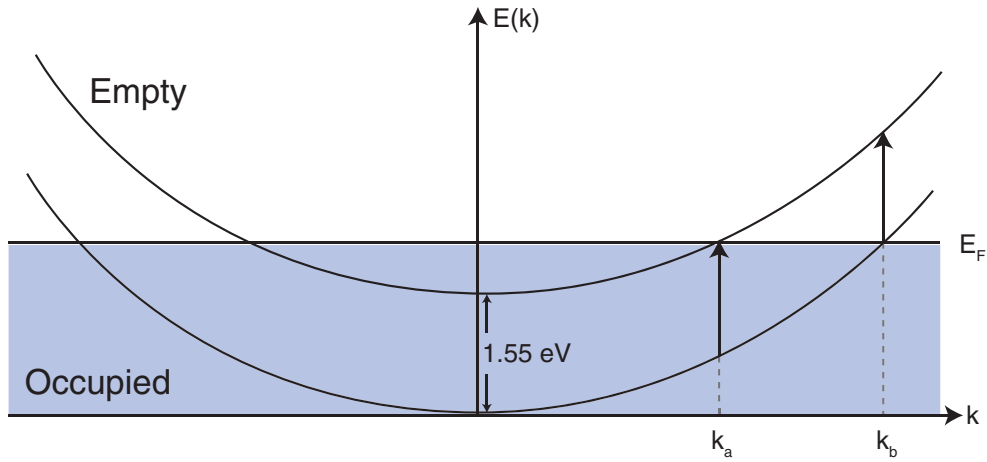
Figure 4.12: Parallel bands in the band structure of aluminum separated by 1.55 eV.

Due to Pauli blocking of the excited states the reflectivity of the 800-nm probe,

when the probe arrives shortly after the pump, will increase. As the fluence of the applied pump field increases, the electronic population promoted to higher-energy states increases and less electrons are available to absorb the probe photons, therefore the reflectivity of the probe changes monotonically with the pump fluence. Once the pump fluence exceeds the threshold value of 34 mJ/cm^2 the reflectivity of the probe does not increase any further but drops to a value that remains constant for pump fluences above the threshold value. This indicates that a severe modification of the band structure takes place at these fluences. Most probably the parallel band structure collapses and the effect of transient bleaching is not observed any further. Additionally, when the authors examine the sample under an optical microscope they detect observable damage on the surface for fluences greater than 34 mJ/cm^2.

The question at hand then is: how long after the pump pulse does the damage occur? In order to answer this question the authors measured time-resolved reflectivity dynamics using the pump-probe setup shown in Figure 4.10 and then numerically inverted the Fresnel equations to obtain dielectric constant dynamics. Their results are shown in Figure 4.13.

This Figure shows dielectric constant dynamics (at $\lambda = 800$ nm) for three different fluences. The first fluence, 2.1 mJ/cm^2, is well below the damage threshold and indeed the dielectric constant data show little variation with respect to their equilibrium values. The dielectric constant returns to the equilibrium values shortly after the excitation. The second fluence, 34 mJ/cm^2, is exactly the damage threshold fluence. From Figure 4.13 we see that the dielectric constant becomes significantly perturbed but the authors note that it returns to the equilibrium values 200 ps after the arrival of the pump. Therefore at this fluence the change for the dielectric constant is reversible. The situation becomes more interesting at the third fluence of 63 mJ/cm^2, shown in Figure 4.13. This fluence is well above the
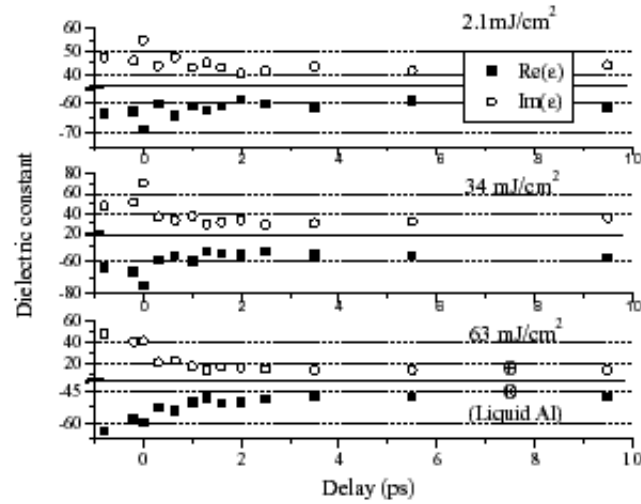
Figure 4.13: Time-resolved dielectric constant dynamics (at 800 nm) following laser excitation below the damage threshold (top panel), at the damage threshold (middle panel), and above the damage threshold (bottom panel). After Ref. [22].

damage threshold and the authors report that the changes in the dielectric constant are irreversible. In this case the dielectric constant seems to obtain the liquid aluminum values within 500 fs after the arrival of the pump. Based on these results the authors conclude that the laser-induced solid-to-liquid phase transition in aluminum is complete 500 fs after photoexcitation.

This time interval is too short for the process to be thermal. In a thermal process heat is transferred from the excited electronic population to the lattice through electron-phonon scattering events. The temperature of the lattice increases, until it reaches the melting temperature of the material and then melting occurs. However, phonon thermalization requires picoseconds to be complete and cannot be responsible for a transition which is complete within 500 fs. Therefore the conclusion is that due to resonant pumping a severe fraction of the electronic population becomes excited to higher-energy states; the electron redistribution alone modifies the potential landscape seen by the ions so dramatically that

even before the ions have the time to equilibrate to the melting temperature severe lattice disordering occurs and the material behaves like a liquid.

4.3 An electron diffraction study of the solid-to-liquid phase transition in aluminum

The results reported in Section 4.2 sparked significant attention. Although non-thermal melting has been repeatedly observed in semiconductors [10, 33–39] it isn't even clear if such a process can be realized in metals. For semiconductors, melting under intense laser irradiation is now generally accepted as an athermal transition mostly induced by a softening of the interatomic bonds, which takes place long before the more conventional thermal transition due to the energy transfer from the electrons to the ionic lattice. Metals on the other hand do not form covalent bonds which would be weakened due to the excitation of electrons from bonding to antibonding states.

Another study about the solid-to-liquid phase transition in aluminum followed in 2003 [99], this time using the diffraction of a femtosecond electron beam as a probe. The advantage of the electron diffraction probe is that it provides direct access to the lattice during the transition, while reflectivity measurements cannot directly distinguish between electron and lattice dynamics. Of course, by interpretation of the optical results and the timescales associated with the reflectivity dynamics one can often infer whether the changes are electron- or lattice-induced. Since femtosecond electron diffraction can only resolve lattice dynamics the two techniques can be used complementary to provide the complete picture of ultrafast dynamics in solids.

The ultrafast electron diffraction technique is being developed for over two decades, as shown in Figure 4.14.
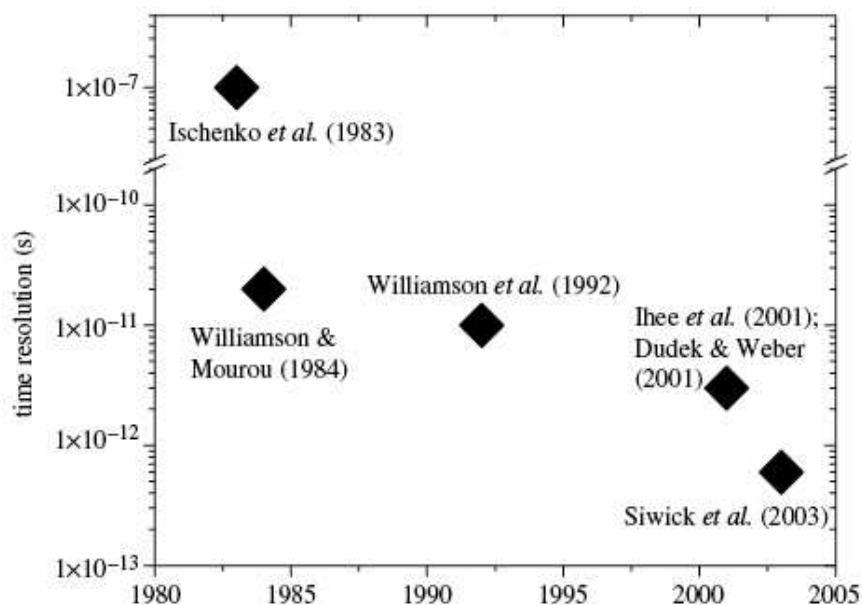
Figure 4.14: Milestones in electron diffraction history. After Ref. [58].

In this technique a laser beam provides the pump while an electron source provides electron pulses which serve as the probe. The challenge lies in obtaining a high-flux electron pulse with the required time resolution and sensitivity to capture the photoinduced dynamics. Figure 4.14 summarizes the most important advances in electron diffraction experiments with respect to achieved time resolution. In 1983 Ischenko *et al.* [100] do the first laser-pump electron-probe experiment on the gas phase photodissociation of CF_3I; one year later Williamson *et al.* [101] break the nanosecond limit with the first subnanosecond electron diffraction experiment on the laser melting of superheated Al; in 1992 Williamson *et al.* [102] revisit the photodissociation of CF_3I in an experiment with increased time resolution; in 2001 two groups achieve even shorter electron pulses in experiments involving $C_2F_4I_2$ photodissociation [103] and cyclohexadiene ring-opening [104]; finally, in 2003 Siwick *et al.* [59, 99] achieve subpicosecond electron pulses for the first time and choose to

study the solid-to-liquid phase transition in aluminum.

The experimental setup of Siwick *et al.* is shown in Figure 4.15.
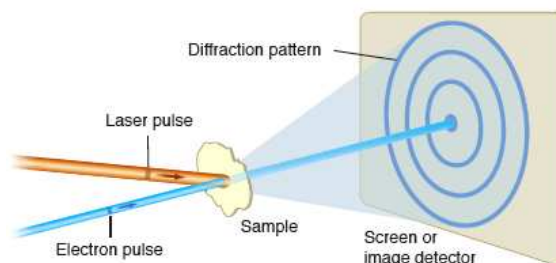
Figure 4.15: Schematic diagram of the electron diffraction experiment of Siwick *et al.* [99].

The laser beam they used as the pump was the output of an amplified Ti:sapphire laser system with a central wavelength of 775 nm and a pulse duration of 120 fs. Each laser pulse was divided into two parts, one used to photoexcite the sample and one used to drive the photoactivated electron gun which produced the electron pulses that were used as probe pulses. The electron gun was capable of delivering sub-500-fs electron pulses containing number densities sufficient for structure determinations with fewer than 100 shots. After transmission through 20-nm thick polycrystalline aluminum films the electron pulses are detected by a plate-phosphor screen and a CCD camera that images the diffraction patterns. The use of films as thin as 20 nm prevents broadening of the time resolution by velocity mismatch between optical and electron pulses over the sample volume.

The authors used pump pulses with an incident fluence of 70 mJ/cm^2 in order to drive the solid-to-liquid phase transition in aluminum. They recorded electron diffraction patterns at pump-probe delay intervals of 500 fs until the onset of the transition and coarser time steps afterwards. The results are shown in Figure 4.16.

At the top left panel we observe that 500 fs after the laser excitation the diffraction pattern still shows the diffraction rings which are associated with the fcc lattice structure of
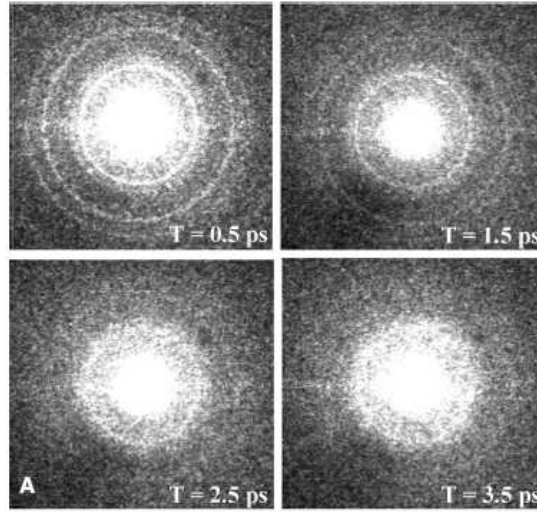
Figure 4.16: Sequence of electron diffraction patterns of aluminum taken after photoexcitation above the damage thershold. After Ref. [99].

polycrystalline aluminum. The rings are no longer visible at 3.5 ps and the authors conclude that this is the time needed for the solid-to-liquid phase transition to be completed for the 20-nm films used in this experiment. The single broad ring present at the diffraction pattern at 3.5 ps is characteristic of a liquid. The absence of discrete features in the diffraction pattern reveals the complete loss of long-range order. Measurements up to 6 ps after the arrival of the pump beam suggest that the liquid structure has not fully equilibrated by that time. It is difficult to say whether the liquid structure has equilibrated even 50 ps after the arrival of the pump beam. However, what is important in this study is not the equilibration of the liquid state but the disappearance of the solid state and this seems to happen in 3.5 ps.

These findings indicate that the solid-to-liquid phase transition in aluminum is a thermal process and its timescale is set by the electron-phonon coupling constant, g, as predicted by Eq. 2.64, in which we need to neglect the diffusion term. We can solve Eqs. 2.64 and 2.65 using the relevant parameters for Al: electron heat capacity $\gamma = 125$ J/m^{3}K^2,

lattice heat capacity $C_l = 2.4 \times 10^6$ J/m^{3}K, and electron-phonon coupling constant g = 3.1×10^{17} W/m^{3}K [105]. For the photoexcitation strength used in their experiment Siwick *et al.* expect the aluminum lattice to achieve its melting point temperature of 933 K within 750 fs after the arrival of the pump beam, according to the two-temperature model. By 3.5 ps the lattice has disordered to such degree that the diffraction peaks associated with all the lattice planes are reduced below the noise level of this experiment. This finding is in contrast with the conclusions of Guo *et al.* which we described in Section 4.2, according to which the solid-to-liquid phase transition in aluminum is a non-thermal process that is complete within 500 fs.

4.4 Comparison of previous studies and our technique

The two studies we presented in detail in the previous sections reached two different results. The optical pump-probe study centered at 800 nm concluded that the changes in the dielectric constant of aluminum during the solid-to-liquid phase transition take place within 500 fs and afterwards the material exhibits dielectric constant values which match very well the values of the dielectric constant of liquid aluminum. From these measurements it was inferred that lattice melting occurs on a subpicosecond scale, which is shorter than the time it takes for optically excited electrons to relax via lattice phonon scattering. These observations suggest a non-thermal mechanism for melting, where the lattice bonding softens because of the photoinduced changes in electron distribution. On the other hand, the electron diffraction experiment showed that the solid-to-liquid phase transition in aluminum is complete within 3.5 ps, a time which is set by the electron-phonon coupling constant in agreement with the thermal mechanism for melting.

Each of the aforementioned studies has its own limitations. The optical pump-

probe study has excellent time resolution, down to 130 fs, but limited spectral information because it tracks the changes in the dielectric constant of aluminum only at one wavelength. Furthermore, as we showed in section 3.4, in the case of metals inversion of reflectivity measurements at two angles of incidence to obtain dielectric function values is subject to big errors that compromise the validity of the results. In Figure 4.17 we show the mapping of a grid of dielectric constant values onto reflectivity space for the angles and polarization used in the optical pump probe study of Guo *et al.* We choose a set of dielectric constants with a negative real part and a positive imaginary part because this is the case for metals and particularly for aluminum in the visible range.
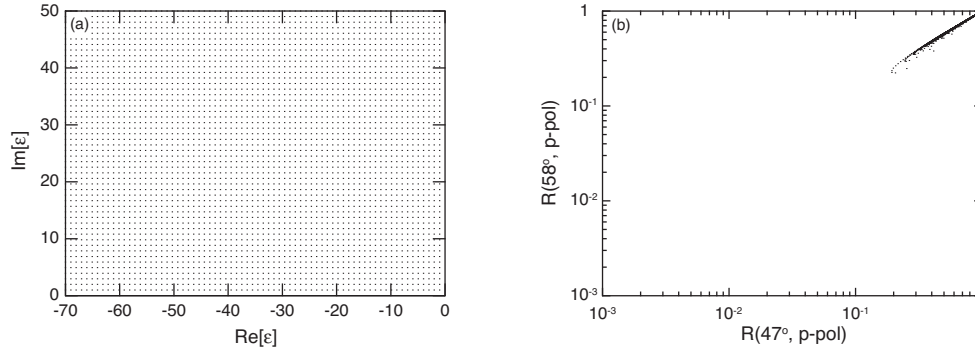
Figure 4.17: (a) A grid of dielectric constant values with negative real part and positive imaginary part. (b) The Fresnel formulas are used to calculate reflectivity pairs at the angles and polarizations indicated for each of the points in (a).

We observe that the mapping does not favor inversion of reflectivity data to dielectric constant values. To make things worse, there is a limited number of studies that provide measurements on the dielectric constant of liquid aluminum and there are significant variations between them. In particular, the study by Miller [94] that the authors use to compare their data on the liquid dielectric constant is challenged by the author herself after careful analysis which leads to unrealistic fitting parameters.

The electron diffraction study unambiguously provides information on the atomic

configuration of aluminum during the solid-to-liquid phase transition. However, being the first subpicosecond electron diffraction experiment it still suffers from limited time resolution compared to optical experiments. The time-resolved data are taken with a step of 500 fs which is the completion time of the optical study. Furthermore, electron diffraction is sensitive only to lattice changes and not to electronic redistribution effects which would provide a more complete picture of the transition.

Given the above limitations and the obvious discrepancies between the two studies we set out to revisit the optical properties of aluminum during the solid-to-liquid phase transition employing the dual-angle time-resolved reflectometry technique which we described in section 3.2. Our technique combines very high time resolution –down to 40 fs– with a broad spectral window, extending from 1.7 to 3.5 eV. Therefore it is suitable for resolving ultrafast phase changes clearly and unambiguously. The results are a combination of the electronic and structural response. Due to the different timescales of electronic and structural effects it is usually straightforward to interpret the observed dynamics. In the next chapter we present the results of broadband reflectometry on the solid-to-liquid phase transition in aluminum.

4.5   Summary

Aluminum is one of the most widely used metals and its optical properties are extensively studied, both theoretically and experimentally. The band structure of aluminum is very similar to a free-electron band structure. However, the existence of parallel bands with an energy gap 1.55 eV, lying above and below the Fermi level, introduce prominent interband electronic transitions in the optical spectrum of the material. The result is that aluminum exhibits pronounced absorption at wavelengths around 800 nm (1.55 eV). Liquid

aluminum does not exhibit the same enhanced absorption at 800 nm, most probably because the parallel bands do not longer exist due to the loss of long range order in this phase. The phase transition of aluminum from the solid to the liquid state has recently been a subject of debate. An optical study completed in 2000, found that the phase transition is complete within 500 fs, indicating a non-thermal mechanism, since this time is much shorter than the lattice thermalization time. Later, in 2003, an electron diffraction study produced a different result. The transition was complete after 3.5 ps, indicating a thermal mechanism, consistent with the two-temperature mode. Motivated by this discrepancy we chose to perform another optical study on the solid to liquid phase transition in aluminum, using our broadband reflectometry technique, presented in chapter 3. We discuss the results and compare them with the two existing studies in the next chapter.

Chapter 5

Laser-induced solid-to-liquid phase transition in aluminum

In this chapter we present femtosecond time-resolved measurements of the reflectivity of aluminum during the solid-to-liquid phase transition over the spectral range 1.7 – 3.5 eV. Previous optical and electron diffraction studies have shown discrepancies in the time scale of the solid-to-liquid phase change, and have led to different interpretations of the transition mechanism. Our experiments yield optical data that agree with the electron diffraction study and verify that this transition is a thermal process mediated through the transfer of heat from the photoexcited electronic population to the lattice.

5.1   Introduction

The dynamical properties of the electrons and the lattice in solids define many basic properties of these materials, such as their conductivity, superconductivity, magnetism, and their linear and nonlinear optical characteristics. Excitation with intense ultrafast laser pulses is one way to induce non-equilibrium processes and observe resulting dynamics.

However, a comprehensive understanding of the relevant physics remains elusive due to the extreme non-perturbative nature of strong-field laser interactions with valence and core states. Therefore ultrafast pump-probe measurements are vital for preparing matter into an exotic state within hundreds of femtoseconds, and elucidating the mechanisms by which the excited matter reaches equilibrium.

Previous studies have shown that large laser-induced changes in carrier occupation in metals and semiconductors can lead to substantial band structure renormalization and even to structural phase transitions [10, 21–25]. An ultrafast laser pulse, with a duration shorter than the excited electron energy-loss lifetime, can rapidly heat electrons to a very high temperature while leaving the lattice relatively cool since the heat capacity of the electrons is much smaller than that of the lattice. This transient two-temperature system tends to reach equilibrium within a few picoseconds via electron-phonon interactions as well as electron transport out of the excited region. In the perturbative low-intensity regime, the excited region reaches equilibrium with little disorder. In the high-intensity regime, on the other hand, structural changes such as melting and ablation take place and the material is permanently modified. Previous studies have shown a novel non-thermal melting mechanism in semiconductors [10, 33–39]. This non-thermal process is typically very fast, on the order of hundreds of femtoseconds, and occurs when the ions rapidly gain kinetic energy after the laser-induced electronic excitation and rearrange themselves in a liquid configuration before the lattice has enough time to thermalize.

In this paper we present an ultrafast pump-probe study of the solid-to-liquid phase transition in aluminum. Even though solid-to-liquid phase transitions in metals are of fundamental importance in materials processing and manufacturing, the understanding of laser-induced melting in metals is still mostly at the phenomenological level. The optical properties of aluminum have been a subject of intense research over the past decades [91].

However, there are only a few studies providing information about the optical properties of liquid aluminum and the results often contradict each other [94–98]. The reason is that experimental studies encounter errors arising from surface contamination and the high melting temperature of metals, while theoretical studies are challenged by the breakdown of translational invariance needed in the usual band structure calculations. Even less information exists on how aluminum passes from one phase to another. The widespread use of Ti:sapphire lasers operating at wavelengths in the 800-nm regime (photon energy = 1.55 eV) is particularly suitable for the photoexcitation of aluminum because its absorption is enhanced at these wavelengths and light can couple into it more effectively. The reason for this enhanced absorption is the existence of nearly parallel electronic bands around the Fermi energy, separated by a gap of 1.55 eV, which induce an interband contribution to the dielectric function around 800 nm [93]. These parallel bands, leading to enhanced absorption, allow the excitation of a large population of electrons. The presence of such a large excited electronic population poses the question of whether or not the material can undergo an electronically induced non-thermal solid-to-liquid phase transition. So far there have been two studies that looked into this particular question. Guo *et al.* [22] performed optical pump-probe measurements on the dielectric constant of aluminum at 800 nm, with femtosecond time resolution. They have shown that at 800 nm the dielectric constant of solid aluminum reaches its liquid value within 500 fs. This time is shorter than the time scale for lattice thermalization, which lies in the picosecond regime, therefore the material was believed to undergo a non-thermal, electronically induced phase transition. Siwick *et al.* [99] sent 500-fs long electron pulses through an optically excited thin aluminum film and studied the resulting electron diffraction spectra. It was found that for the 20-nm thick aluminum films used, the solid-to-liquid phase transition was completed within 3.5 ps and that it was propagated by thermally sampled configurations.

Each of the two aforementioned studies has its limitations. The optical pump-probe experiment was performed with high time resolution, down to 130 fs, but was spectrally limited since it tracked the dynamics of the dielectric constant at only one frequency. The electron diffraction experiment provided a direct picture of the aluminum lattice during the phase transition but it was performed with limited time resolution, only down to 500 fs. We set out to link the two experiments with a broadband time-resolved reflectometry technique, which enables the study of the optical properties of aluminum during the solid-to-liquid phase transition over a wide frequency range, from 1.7 to 3.5 eV, and with high time resolution, down to 40 fs. Our findings indicate that the solid-to-liquid phase transition in aluminum is a thermal process that takes place on a picosecond timescale. The observed optical properties over this broad frequency range do not exhibit a subpicosecond equilibration time as was observed by Guo *et al.* [22].

5.2 Experimental

We performed dual-angle-of-incidence reflectometry in a pump-probe setup [60] to measure the changes in the reflectivity of aluminum during the solid-to-liquid phase transition. We use a commercially available Ti:sapphire oscillator to seed a home-built 1-kHz-repetition-rate Ti:sapphire multipass amplifier which produces 40-fs, 0.5-mJ pulses at 800 nm [62]. Our pump beam consists of 800 nm s-polarized pulses that we focus on the sample. We use a *p*-polarized white-light (1.7-3.5 eV) probe, which we obtain by focusing an 800 nm laser pulse into a 3-mm thick piece of CaF_2. To correct for dispersive stretching of this broadband probe pulse, we measure the chirp separately using a Te sample [12] and time-shift the data accordingly. We use a small fraction of the probe beam as a reference beam in order to normalize the effect of pulse energy fluctuations. The pump beam spot size

is about four times larger than the probe beam spot on the sample in order to ensure probing of a homogeneously excited region. We performed single-pulse measurements where we translate the sample between different shots so that each pump pulse excites an undamaged area. Each data point was averaged over 20 shots. Two sets of reflectivity measurements were taken at 68.4° and 58.7° angles of incidence for the probe beam. The detection system is calibrated so as to obtain absolute reflectivity values. For all data sets, the angle between the pump and probe beams was kept as small as possible (approximately 13°) to minimize the loss of temporal resolution that accompanies non-collinear pump-probe experiments.

The polycrystalline 1-μm thick aluminum samples were prepared by electron beam evaporation of aluminum in high vacuum on clean glass microscope slides. The thickness of the films is much greater than the expected penetration depth of the optical fields, 10 nm, and thus the samples can be considered to be optically thick. Reflectivity measurements performed on aluminum and Al_2O_3 at laser intensities and wavelengths similar to the ones used in our study, determine that a thin oxide layer does not significantly affect the aluminum metal data [106].

5.3   Results

In order to study the solid-to-liquid phase transition in aluminum we had to determine the minimum incident laser fluence which induces a permanent change on the material surface; this is otherwise known as the damage threshold fluence. For this purpose we irradiated our aluminum sample with single pump pulses of varying intensity. With the aid of a scanning electron microscope, we were able to determine the minimum laser fluence required to damage. Our results are shown in Figure 5.1, where we observe a spectrum of damage: at high fluences, we clearly see damage spots, and at low fluences, there is

no visible damage. From Figure 5.1, we conclude that the damage threshold fluence for our aluminum sample lies between 157 mJ/cm^2 and 262 mJ/cm^2 and we estimate it to be $F_{th} = 210$ mJ/cm^2. A more physically relevant quantity is the absorbed fluence because it directly correlates with the degree of electronic excitation. For our samples the peak absorbed fluence that corresponds to an incident fluence of 210 mJ/cm^2 is 34 mJ/cm^2. In this chapter we report our results in terms of the peak absorbed fluence.
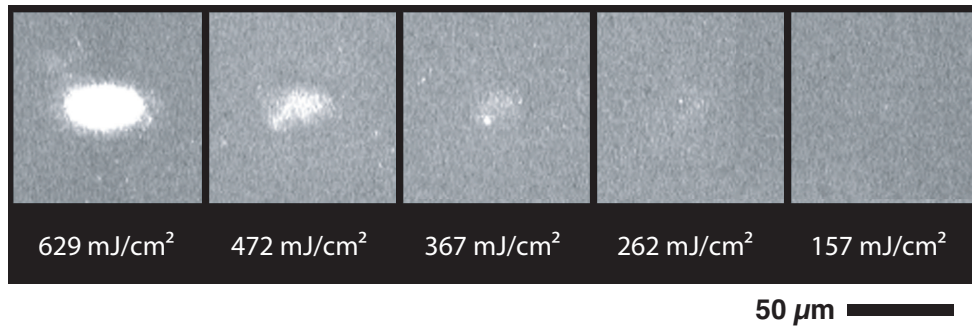

Figure 5.1: Scanning electron micrographs of a 1-μm thick Al film irradiated with single 40-fs, 800-nm pulses of varying incident fluences. A damage spot appears after irradiation for fluences down to 262 mJ/cm^2.

Figure 5.2 shows time-resolved reflectivity dynamics of aluminum across 1.8 – 3.5 eV following single pulse excitation where the peak absorbed fluence is 121 mJ/cm^2. The angle of incidence of the probe is 68.4°. For negative time delays, when the probe arrives before the pump, we find that the reflectivity data are in very good agreement with ellipsometric measurements of the aluminum sample used. After the arrival of the pump, for positive time delays, we observe that across all frequencies within our spectral range the reflectivity starts to drop as the solid-to-liquid phase transition is initiated. The transition is complete after 1.9 ps, as can be seen by the darkened flat region in Figure 5.2. This is when the reflectivity reaches its equilibrium value, which, for all frequencies in the white-light probe, is lower than the reflectivity of solid aluminum.
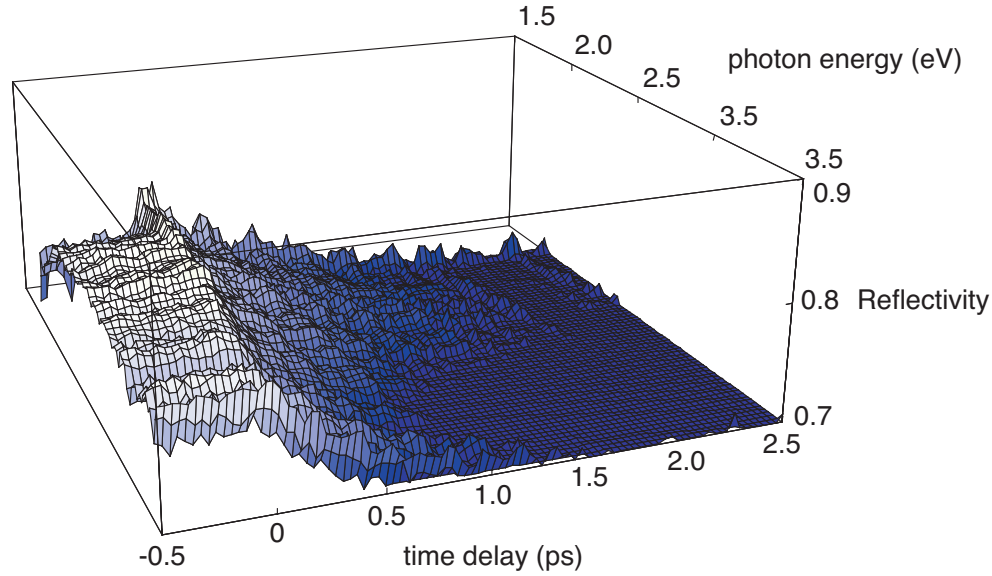
Figure 5.2: Time-resolved reflectivity dynamics of aluminum following single-pulse photoexcitation across the frequency range 1.8 – 3.7 eV. The peak absorbed fluence of the incident laser pulse is 121 mJ/cm^2.

Figure 5.3(a) shows reflectivity dynamics for one frequency in the white-light spectrum, 2.1 eV, for the peak absorbed fluence of 121 mJ/cm^2 shown in Figure 5.2, as well as for three other fluences, namely 104 mJ/cm^2, 141 mJ/cm^2, and 167 mJ/cm^2. All data are measured with the probe beam incident at 68.4° with respect to the sample normal. Figure 5.3(b) shows reflectivity dynamics for fluences similar to those in Figure 5.3(a), measured with the probe beam incident at 58.7°. Because the first angle of incidence, 68.4°, is the one closer to the angle for minimum p-reflectivity, the laser induced changes in the white-light reflectivity are expected to be larger compared with the changes observed at 58.7°, in agreement with Figure 5.3. In both angles the reflectivity of the liquid state decreases as the incident pump fluence increases. This is because the optical properties of liquid aluminum are known to change monotonically with temperature in the wavelength range that is accessible to our experiment [96, 107]. Specifically, the index of refraction increases

and the absorption coefficient decreases with increasing temperature. These changes, when accounted for in the Fresnel equations, predict a decrease in reflectivity with increasing temperature. Our observations as shown in Figure 5.3, are in agreement with intuition that a high pump fluence results in high temperatures for the liquid state, which then leads to decreased reflectivity.
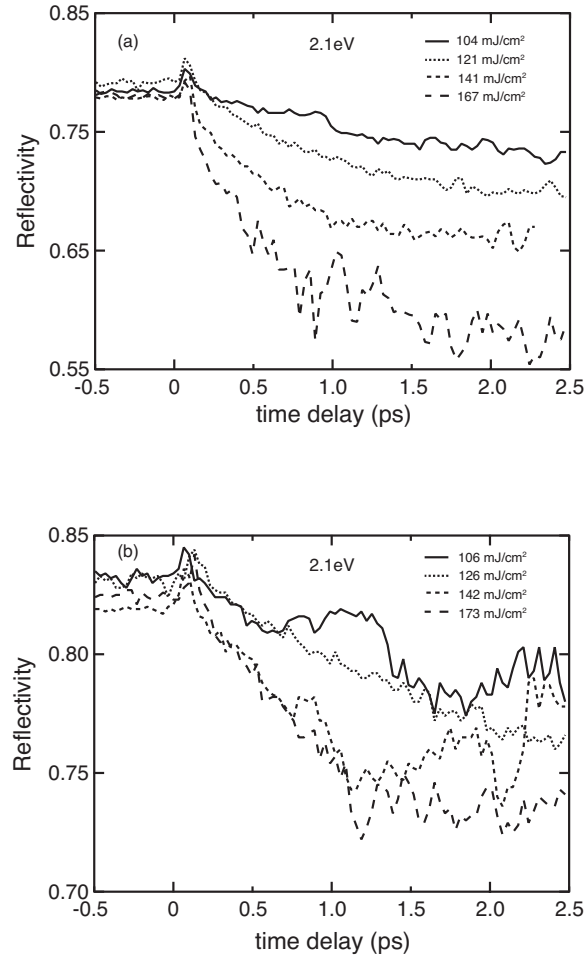

Figure 5.3: Time-resolved reflectivity dynamics of aluminum following single-pulse photoexcitation at 2.1 eV for different peak absorbed fluences of the excitation pulse. The reflectivity measurements are taken at a probe beam incidence angle of (a) 68.4° and (b) 58.7°.

We find that the solid-to-liquid phase transition is complete within 1-2 ps for all

fluences applied. We extract this time scale from curves similar to the ones shown in Figure 5.3 for all the different frequencies contained in our white-light probe. The dynamics in all frequencies show similar time scales. For each fluence, we take the average of the solid-to-liquid transition time over a frequency range of 2 – 3.3 eV, and plot it in Figure 5.4. In the averaging process we did not take into account the two extrema of our spectral window because the signal to noise ratio is lower for those frequency values. Figure 5.4 shows that the average transition times are similar for like fluences with the biggest discrepancies present at the lowest and highest fluence values. For the two lowest fluences the changes in the reflectivity were small and the signal to noise ratio was significantly reduced. For the two highest fluences we had to decrease the amount of light entering our detector to prevent saturation by the intense scattered pump light. As a result there was a reduction in the intensity of the measurable white-light probe and the signal to noise ratio was also reduced. The results show no clear dependence on fluence. This is further supported by the least-squares fit (solid line) plotted in Figure 5.4, which almost has a zero slope.

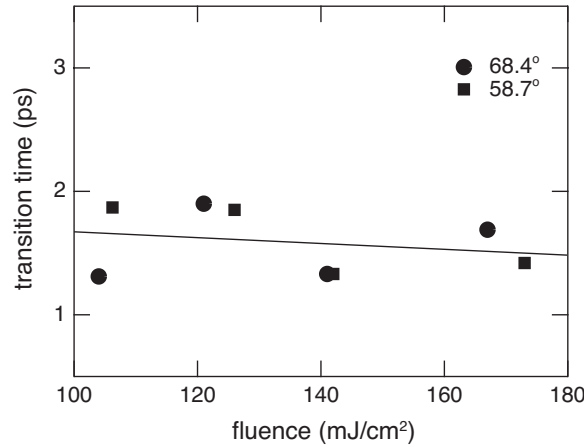Figure 5.4: Average transition times extracted from reflectivity measurements similar to the ones shown in Figure 5.2 for different peak absorbed excitation fluences. Transition times of reflectivity curves in the range 2-3.3 eV were averaged for each fluence. Reflectivity data at probe incidence angles of 68.4° (circles) and 58.7° (squares) are analyzed. The solid line is the least squares fit to the data points.

In order to exclude the possibility that what we observe is a transient superheated state or a plasma expansion process we took data up to 11 ps. In Figure 5.5 we plot reflectivity data at 2.1 eV for a peak absorbed fluence of 121 mJ/cm^2 for the pump and an angle of incidence of 70° for the probe. The dynamics across all frequencies of the white-light spectrum are similar to the ones shown in Figure 5.5: the reflectivity drops for about 2 ps and after that it remains constant up to 11 ps. In a similar pump-probe experiment [108] it was shown that the effect of plasma expansion on aluminum results initially in a pulse-width-limited drop in the reflectivity followed by a slower recovery to approximately 60% of the original value within 15 ps. However this is not what we observe in our experiment where aluminum simply melts within 1-2 ps and then remains in the liquid state. Our result also rules out a transient superheated state, which would evolve over the course of 11 ps.
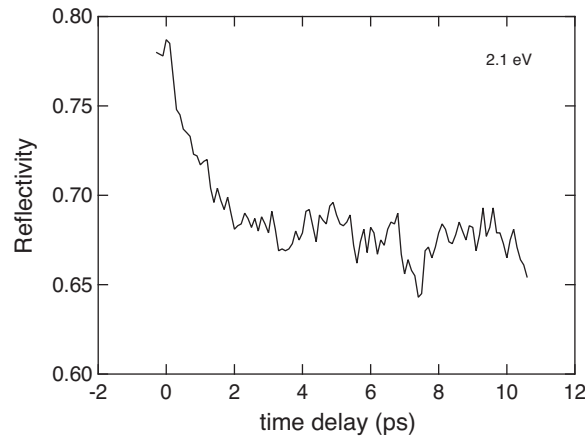

Figure 5.5: Time-resolved reflectivity dynamics of aluminum following single-pulse photoexcitation at 2.1 eV, extending up to 11 ps. The peak absorbed fluence of the incident laser pulse is 121 mJ/cm^2. The reflectivity measurements are taken at an angle of 70°.

5.4   Discussion

Our value for the damage threshold fluence is significantly higher than the values reported in the two previous studies on the solid-to-liquid phase transition of aluminum [22, 99]. Guo *et al.* [22] observed damage formation for incident laser fluences higher than 34 mJ/cm^2 and Siwick *et al.* [99] initiated the melting process with an incident laser fluence of 70 mJ/cm^2. In our case, however, we observe no damage formation for incident laser fluences less than 210 mJ/cm^2. The reason for this discrepancy lies in the different sample thicknesses of the aluminum films used in our study and the two previous studies. Our samples were 1-μm thick in contrast to Siwick *et al.*'s 20-nm thick films and Guo *et al.*'s reported use of thin films. For film thicknesses on the order of 20 nm, the length scale is comparable to the ballistic range of the photoexcited electrons. As a result, the film becomes uniformly heated upon electron thermalization and there are no significant hot-electron diffusion effects [26]. The diffusion inhibition in very thin films results in a higher energy density stored in the material and therefore thin films require a lower incident fluence for damage to occur. However, in the 1-μm thick aluminum samples used in our study, diffusion of hot electrons through bulk material becomes significant. The energy deposited by the laser pump pulse is distributed deeper via electron diffusion, resulting in a lower energy density stored in the material. The damage threshold for our aluminum films is therefore about 6-7 times higher than the one previously reported for thin aluminum films, in agreement with similar studies in other materials [26].

The solid-to-liquid phase transition times that we observe in our experiment lie in the picosecond regime (*cf.* Figure 5.4). Our results qualitatively agree with the results of Siwick *et al.* [99] in that the phase transition is a thermal process, mediated by heat transferred from the excited electronic population to the lattice through electron-phonon

coupling and becomes complete within a few picoseconds. The discrepancy between our transition times and the 3.5 ps obtained in their study is primarily due to the different thicknesses of the aluminum samples. As we already mentioned, in the 20-nm thick aluminum films that Siwick *et al.* used, hot-electron diffusion was inhibited while for the 1-μm thick aluminum films we used it is strongly present. This results in not only the higher damage threshold that we discussed earlier but also in faster equilibration times for our experimental conditions according to the two-temperature model [26]. Another factor that contributes to the faster dynamics we observe is that we excite the material 3-4 times above the damage threshold fluence while Siwick *et al.* applied an excitation only twice as much as their damage threshold fluence. We can only detect reflectivity changes down to 3-4%, so we use such a strong excitation field to generate a large signal. Our sensitivity is limited by large shot-to-shot fluctuations in the white-light intensity. It should be noted also, that our results agree very well with recent experiments on phase transitions in Au [24], where the transition from the solid state to a quasisteady liquid state takes place in 1.5 ps. The fluences used in these experiments are similar to the fluences we used in aluminum.

The reason that Guo *et al.* [22] observe an ultrafast phase transition with a 500 fs timescale is most probably because they monitor only one frequency, the frequency of the resonance in the dielectric function of aluminum. Indeed, our data at 1.7 eV, as shown in Figure 5.6, exhibit faster dynamics than most of the other frequencies in our white-light probe. This is the frequency in our spectral window closest to the aluminum resonant frequency of 1.55 eV. In Figure 5.6, we plot the transient reflectivity at 1.7 eV following an excitation of 141 mJ/cm^2. The transient reflectivity at 2.1 eV for the same excitation fluence is the dashed line in Figure 5.3(a). We observe that the reflectivity at 1.7 eV reaches an equilibrium value at 800 fs after the arrival of the pump pulse. This time is close to the 500 fs reported by Guo *et al.* and it is much less than the time we extracted from Figure
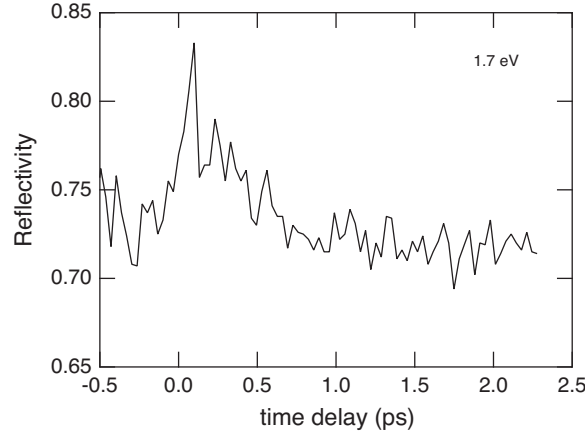
5.3(a).

Figure 5.6: Time-resolved reflectivity dynamics of aluminum at 1.7 eV following single-pulse photoexcitation. The peak absorbed fluence of the incident laser pulse is 141 mJ/cm^2. The reflectivity measurements are taken at a probe incidence angle of 68.4°.

The explanation for this discrepancy lies in the difference between the optical properties of solid and liquid aluminum. To compare this, Figure 5.7 shows the solid line representing the reflectivity of solid aluminum at 68.4° [91], and the dashed line representing the reflectivity of liquid aluminum at the same angle [98]. We observe that while the changes in the reflectivity are big in most frequencies depicted in Figure 5.7, the reflectivity remains almost the same at the resonant frequency of 1.55 eV. It seems that when looking at the resonant frequency alone there is not much change to observe and therefore one can obtain misleading results, which indicate a non-thermal transition. Reflectivity changes measured across a wider frequency range indicate that the transition is slower, in agreement with the thermal mechanism [99].

In all the fluences we studied, the data exhibit a sudden increase in the reflectivity near $t = 0$, which is then followed by a decrease towards the liquid value. This feature however is not present in all frequencies contained in our probe. It appears at the lower frequencies of the white light and then disappears. Figure 5.8 shows the maximum photon
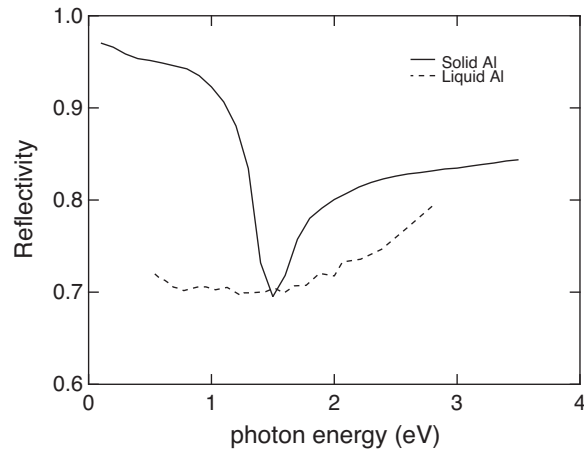
Figure 5.7: *p*-polarized reflectivity of solid aluminum (solid line) and liquid aluminum (dashed line) calculated for an angle of 68.4°. Solid aluminum data: after Ref. [91], liquid aluminum data: after Ref. [98].

energy for which we observe the peak near $t = 0$ at the reflectivity traces, for all the fluences we applied. Electron heating is not likely to be the cause of this observation because it would create a drop rather an increase in reflectivity [108].
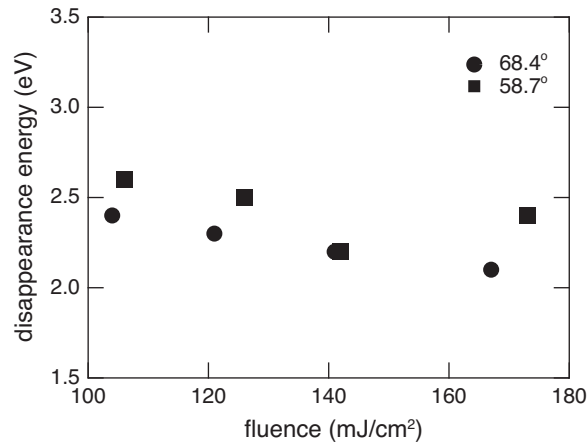
Figure 5.8: Maximum photon energy in the white-light probe for which we observe a sudden reflectivity increase near $t = 0$ for all fluences we applied.

The presence of a feature near $t = 0$ is customary in single-color pump probe experiments and is considered to be a coherent artifact, arising from the interference of

the pump and the probe beams when they arrive simultaneously at the material surface [109–114]. More precisely, as the pump and the probe interfere, a transient absorption grating is produced, which scatters a portion of the pump beam into the probe beam. A coherent artifact is almost always present in pump-probe experiments where the two beams have the same polarization. However, when the polarizations of the two beams are crossed, as is the case in our experiment, the coherent artifact completely disappears or it appears with reduced amplitude [112]. All this discussion applies when the pump and the probe beams have the same frequency and they are derived from the same pulse. In our case the pump and the probe do not have the same frequency, since our pump is centered at 1.55 eV and our probe spans the range of 1.7 – 3.5 eV. Nevertheless, it has been shown that if the two beams are coherent and the pump beam has a frequency ω_1 while the probe beam has a different frequency ω_2, there can still be a coherent artifact [112]. This is true when $|\omega_2 - \omega_1|^{-1} > \tau_{resp}$, where τ_{resp} is the decay time of the impulse response of the material to a delta function excitation. In our experiment the pump and the white-light probe are coherent because they are derived from the same laser pulse. Therefore, from Figure 5.8 we conclude that the decay time of the impulse response of our aluminum sample is about 5 fs. The presence of a coherent artifact does not affect the conclusions of this dissertation because we don't use the data near $t = 0$ for this purpose. However, it can be a severe limitation for experiments that want to study effects which take place during the pump pulse duration.

In Figure 5.9, we show reflectivity data at a negative time delay, that is before the arrival of the pump (dashed line), superimposed on the reflectivity of our sample at this particular angle of incidence (solid line), which we determine through ellipsometry. Our data agree very well with the expected reflectivity and they confirm the decrease in the reflectivity around the 1.55 eV aluminum resonance. The dotted line in Figure 5.9 represents

the reflectivity spectrum of the final liquid state. We observe that for the liquid state the resonant feature is absent and the reflectivity no longer has an interband contribution near 1.55 eV.
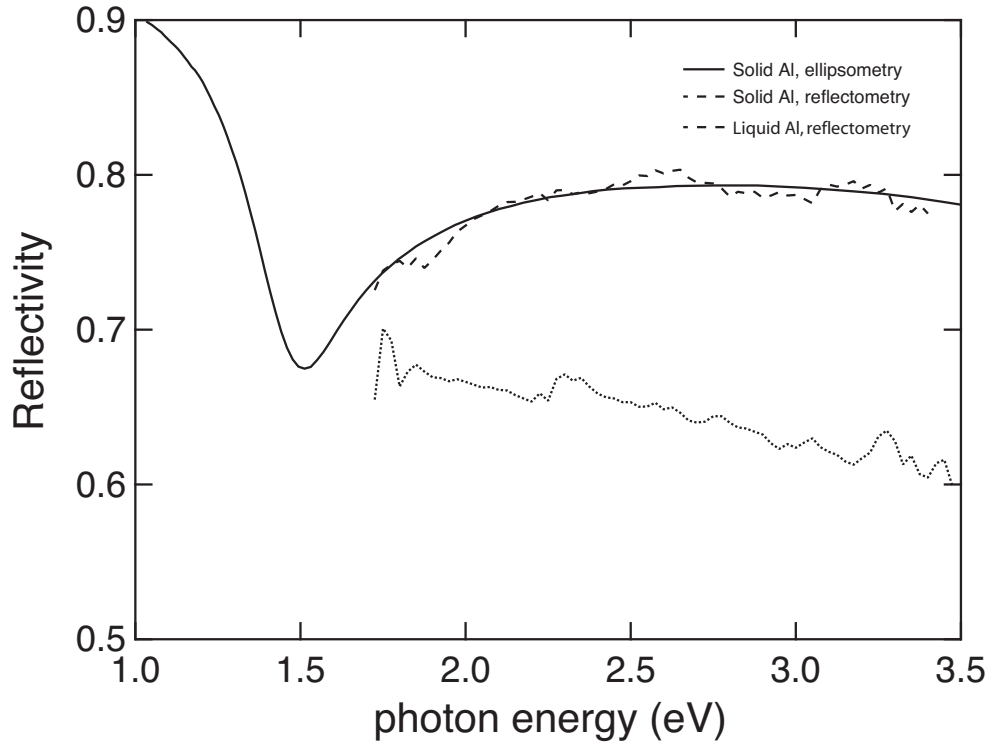
Figure 5.9: *p*-polarized reflectivity of solid aluminum, determined through ellipsometry (solid line) and reflectometry (dashed line) at 68.4°. *p*-polarized reflectivity of liquid aluminum at the same angle (dotted line).

This is true for all the fluences we studied, as shown in Figure 5.10. Due to the loss of long-range order in the lattice, the parallel band structure is absent in the liquid state of aluminum. This conclusion is in agreement with most of the studies on the optical properties of liquid aluminum, which observe only Drude-like contributions to the reflectivity of the liquid state [94, 95, 98].
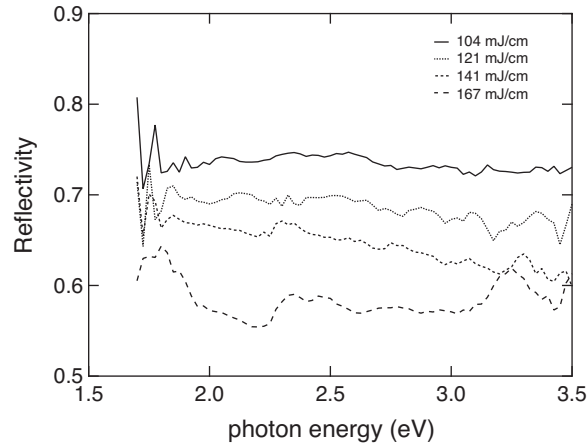
Figure 5.10: Reflectivity spectra of liquid aluminum following single-pulse photoexcitation for different peak absorbed fluences. Measurements are taken at 68.4°.

5.5   Summary

We presented broadband reflectometry results on the solid-to-liquid phase transition in aluminum. The timescale of the transition appears to be 1–2 ps indicating a thermal mechanism, in agreement with electron diffraction studies. The resonance in the optical properties of solid aluminum at 1.55 eV is absent in the liquid state, demonstrating that the parallel band structure is no longer present. The reflectivity of the liquid state is lower than that of the solid state and remains constant over a period of 10 ps, showing no plasma expansion contributions. A single-color optical probe, centered at the resonant frequency of 1.55 eV, is not the most valid indicator for the completion of the solid-to-liquid phase transition in aluminum. Broadband reflectivity data are required for an accurate study of the timescales involved in the phase transition process.

Chapter 6

Summary and outlook

The development of a variety of ultrafast spectroscopic techniques, such as optical, x-ray, or electron pump-probe experiments, allows for the complementary study of physical processes that occur in materials during the first hundreds of femtoseconds after photoexcitation. Intense laser excitation prepares matter in unique conditions of temperatures and pressures, which otherwise would be encountered only in the interior of stars. Therefore we have access to exotic states of matter in the controlled laboratory environment, where we can experiment in order to further our understanding about the critical first picoseconds that follow the excitation of a medium, with the ultimate goal of being able to tailor the properties of materials according to the needs of technology.

The optical pump-probe method of ultrafast spectroscopy offers the highest time resolution, down to a few femtoseconds, and allows tracking of the evolution of both the lattice and electronic populations of the material under excitation.The method is well-founded on Maxwell's equations which describe the interaction of matter with light. The dielectric function of a crystalline solid, along with knowledge of the band structure allow for in depth interpretation of the optical data. Intense excitation of materials with ultrashort pulses cre-

ates novel physical processes, which are not accessible with picosecond or nanosecond laser pulses. Non-thermal melting is one process which is achieved through transfer of heat in a material at a rate which is faster than the ionic response times.

Rather than following the traditional single-color reflectivity pump-probe technique, we developed a broadband dual-angle reflectometry method in order to study ultrafast processes in solids. Our technique combines multiple advantages. First, by allowing for the collection of broadband reflectivity data, it offers a more clear and unambiguous interpretation of the mechanisms under study, as well as the relevant time scales. Often, single-color studies observe responses particular to the specific wavelength and they mistakenly interpret them as the material's overall behavior. Broadband data are able to distinguish between general trends and exceptional responses, giving a more complete picture of the dynamics under study. Moreover, where the error is small enough, inverting the reflectivity data to dielectric function values is possible by virtue of having data sets at two different angles of incidence. Having access to the dielectric function response of a material offers a wealth of information, because dielectric function can be translated to transmissivity, electrical conductivity, or band structure, thus offering a view of the intrinsic properties of the medium.

In order to collect broadband optical data we need broadband optical sources. Transparent materials, such as CaF_2, fused silica, or water can be turned into white-light sources when seeded with a femtosecond laser pulse. The spectrum of the generated white light spans the visible and the UV, when the seed is an 800-nm pulse. Recently, the continuous growth in the field of photonic crystals has provided us with a new white-light source: the photonic crystal fiber. These fibers, which are able to confine light in an area of very small diameter, allow for enhancement of nonlinear effects and generation of white light using nJ of input energy. The produced spectrum spans the visible and the near-infrared,

acting complementarily to the white light produced by CaF_2.

Having such elaborate tools and techniques allowed us to study the solid-to-liquid phase transition in aluminum. Aluminum is one of the most widely used metals and the study of its properties is of extreme importance for numerous industrial and technological applications. The band structure of solid aluminum is well studied and it occurs that although the material behaves much like a free-electron metal, the presence of parallel bands above and below the Fermi energy at some symmetry points gives rise to a dominant interband electronic transition which enhances absorption of 800-nm light. The existence of this transition manifests itself as a pronounced dip in the reflectivity of the material. Liquid aluminum, on the other hand, does not preserve this feature due to loss of long range order.

Although the optical properties of solid and liquid aluminum are well established, the transition process from one phase to the other, is a subject of recent debate. In 2000, Guo *et al.* performed single-color reflectivity pump-probe experiments on the dynamics of the particular phase transition in aluminum and they found that the process was complete within 500 fs. This time interval is shorter than the time it takes from heat to be transferred from the photoexcited electrons to the lattice and for subsequent lattice thermalization, therefore they concluded that the observed dynamics indicate a non-thermal melting mechanism. Later, Siwick *et al.* performed an electron-diffraction pump-probe experiment on the same subject and they did not confirm the non-thermal character of the transition. The time scale of the dynamics in their experiment seems to be about 3.5 ps, which is compatible with a thermal melting mechanism.

Intrigued by the difference in the results we set out to study the problem, employing our technique. Our technique offers advantages over both competing techniques because it has a much better time resolution than the 500 fs of the electron diffraction data, while offering broadband reflectivity information in contrast with the single color optical data.

We found that the broadband reflectivity response of the material corroborates the thermal mechanism explanation. Our data indicate that the phase transition is complete within 1.5-2 ps and not 500 fs as the previous optical study reported. It seems that aluminum does not support a non-thermal melting mechanism, as is the case with other metals, due to the increased scattering times which allow for fast heat transfer from the electrons to the lattice.

Aluminum is not the only metal that offers intriguing questions about ultrafast processes which need to be answered. Indicatively, we mention future studies on thin gold films which can be performed with our technique. The existence of an athermal electronic population for more than 500 fs in gold films after moderate laser excitation has been an intriguing result, which renders the two-temperature model invalid. We would like to measure and characterize the dielectric function of such an athermal system and observe the pathway to thermalization. Furthermore, intense laser excitation of gold films is assumed to generate acoustic phonons that bounce back and forth between the two surfaces of the films. The study of the dielectric function of such films will reveal how the lattice deformation caused by the acoustic phonons affects the Fermi level and whether Fermi level oscillations are initiated by this process. The proposed experiments will provide a new probe of phonon dynamics in metals.

References

[1] T. H. Maiman, "Stimulated optical radiation in ruby," *Nature*, vol. 187, p. 493, 1960.

[2] I. S. Ruddock and D. J. Bradley, "Bandwidth-limited subpicosecond pulse generation in mode-locked CW dye lasers," *Appl. Phys. Lett.*, vol. 29, p. 296, 1976.

[3] J. D. Jackson, *Classical Electrodynamics*. New York: Wiley, 3rd ed. ed., 1999.

[4] H. A. Haus, *Waves and Fields in Optoelectronics*. Englewood Cliffs, NJ: Prentice-Hall, 1984.

[5] G. P. Agrawal, *Nonlinear Fiber Optics*. San Diego: Academic Press, 3rd ed., 2001.

[6] N. W. Ashcroft and N. D. Mermin, *Solid State Physics*. Philadelphia: Saunders College, 1976.

[7] J. P. Callan. PhD thesis, Harvard University, 2000.

[8] R. W. Schoenlein, W. Z. Lin, and J. G. Fujimoto, "Femtosecond studies of nonequilibrium electronic processes in metals," *Phys. Rev. Lett.*, vol. 58, p. 1680, 1987.

[9] W. S. Fann, R. Storz, H. W. K. Tom, and J. Bokor, "Electron thermalization in gold," *Phys. Rev. B*, vol. 46, p. 13592, 1992.

[10] P. N. Saeta, J. K. Wang, Y. Siegal, N. Bloembergen, and E. Mazur, "Ultrafast electronic disordering during femtosecond laser melting of GaAs," *Phys. Rev. Lett.*, vol. 67, p. 1023, 1991.

[11] K. Sokolowski-Tinten, J. Bialkowski, A. Cavalleri, D. v. d. Linde, A. Oparin, J. Meyer-ter Vehn, and S. I. Anisimov, "Transient states of matter during

short pulse laser ablation," *Phys. Rev. Lett.*, vol. 81, p. 224, 1998.

[12] D. v. d. Linde and K. Sokolowski-Tinten, "The physical mechanisms of short-pulse laser ablation," *Appl. Surf. Sci*, vol. 154-155, p. 1, 2000.

[13] Y. Y. Tsui, J. Santiago, Y. M. Li, and R. Fedosejevs, "Melting and damage of aluminum surfaces by 80 ps KrF laser pulses," *Opt. Commun.*, vol. 111, p. 360, 1994.

[14] J. Yang, Y. Zhao, and X. Zhu, "Transition between nonthermal and thermal ablation of metallic targets under the strike of high-fluence ultrashort laser pulses," *Appl. Phys. Lett.*, vol. 88, p. 094101, 2006.

[15] H. E. Elsayed-Ali and T. Juhasz, "Femtosecond time-resolved thermomodulation of thin gold films with different crystal structures," *Phys. Rev. B*, vol. 47, p. 13599, 1993.

[16] H. V. Nguyen, I. An, and R. W. Collins, "Evolution of the optical functions of thin-film aluminum: A real-time spectroscopic ellipsometry study," *Phys. Rev. B*, vol. 47, p. 3947, 1993.

[17] P. Y. Yu and M. Cardona, *Fundamentals of Semiconductors*. Berlin: Springer-Verlag, 1996.

[18] M. L. Cohen and J. Chelikowsky, *Electronic Structure and Optical Properties of Semiconductors*. Berlin: Springer-Verlag, 2nd ed., 1989.

[19] M. Born and E. Wolf, *Principles of Optics*. Oxford: Pergamon, 6th ed., 1980.

[20] E. Hecht, *Optics*. Reading, MA: Addison-Wesley, 2nd ed., 1987.

[21] K. Sokolowski-Tinten, J. Solis, J. Bialkowski, J. Siegel, C. N. Alfonso, and D. v. d. Linde, "Dynamics of ultrafast phase changes in amorphous GeSb films," *Phys. Rev. Lett.*, vol. 81, p. 3679, 1998.

[22] C. Guo, G. Rodriguez, A. Lobad, and A. J. Taylor, "Structural phase transition of aluminum induced by electronic excitation," *Phys. Rev. Lett.*, vol. 84, p. 4493, 2000.

[23] A. Cavalleri, C. Toth, C. W. Siders, J. A. Squier, F. Raksi, P. Forget, and J. C. Kieffer, "Femtosecond structural dynamics in VO_2 during an ultrafast solid-solid phase transition," *Phys. Rev. Lett.*, vol. 87, p. 401, 2001.

[24] T. Ao, Y. Ping, K. Widmann, D. F. Price, E. Lee, H. Tam, P. T. Springer, and

A. Ng, "Optical properties in nonequilibrium phase transitions," *Phys. Rev. Lett.*, vol. 96, p. 055001, 2006.

[25] M. Rini, A. Cavalleri, R. Schoenlein, R. Lopez, L. C. Feldman, R. F. Haglund, L. A. Boatner, and T. E. Haynes, "Photoinduced phase transition in VO_2 nanocrystals: ultrafast control of surface-plasmon resonance," *Opt. Lett.*, vol. 30, p. 558, 2005.

[26] J. Hohlfeld, S.-S. Wellershoff, J. Gudde, U. Conrad, V. Jahnke, and E. Matthias, "Electron and lattice dynamics following optical excitation of metals," *Chem. Phys.*, vol. 251, p. 237, 2000.

[27] A. Ng, P. Celliers, A. Forsman, R. M. More, Y. T. Lee, F. Perrot, M. W. C. Dharma-wardana, and G. A. Rinker, "Reflectivity of intense femtosecond laser pulses from a simple metal," *Phys. Rev. Lett.*, vol. 72, p. 3351, 1994.

[28] H. M. Milchberg, R. R. Freeman, and S. C. Davey, "Resistivity of a simple metal from room temperature to 10^6 K," *Phys. Rev. Lett.*, vol. 61, p. 2364, 1988.

[29] U. Teubner, J. Bergmann, B. v. Wonterghem, and F. P. Schafer, "Angle-dependent X-ray emission and resonance absorption in a laser-produced plasma generated by a high intensity ultrashort pulse," *Phys. Rev. Lett.*, vol. 70, p. 794, 1993.

[30] R. Fedosejevs, R. Ottmann, R. Sigel, G. Kuhnle, S. Szatmari, and F. P. Schafer, "Absorption of femtosecond laser pulses in high-density plasma," *Phys. Rev. Lett.*, vol. 64, p. 1250, 1990.

[31] A. N. Mostovych and Y. Chan, "Reflective probing of the electrical conductivity of hot aluminum in the solid, liquid, and plasma phases," *Phys. Rev. Lett.*, vol. 79, p. 5094, 1997.

[32] R. Fedosejevs, R. Ottmann, R. Sigel, G. Kuhnle, S. Szatmari, and F. P. Schafer, "Absorption of subpicosecond ultraviolet laser pulses in high-density plasma," *Appl. Phys. B*, vol. 50, p. 79, 1990.

[33] H. W. K. Tom, G. D. Aumiller, and C. H. Brito-Cruz, "Time-resolved study of laser-induced disorder of Si surfaces," *Phys. Rev. Lett.*, vol. 60, p. 1438, 1988.

[34] K. Sokolowski-Tinten, J. Bialkowski, and D. v. d. Linde, "Ultrafast laser-induced order-disorder transitions in semiconductors," *Phys. Rev. B*, vol. 51, p. 14186, 1995.

[35] I. L. Shumay and U. Hofer, "Phase transformations of an InSb surface induced by strong femtosecond laser pulses," *Phys. Rev. B*, vol. 53, p. 15878, 1996.

[36] L. Huang, P. Callan, E. N. Glezer, and E. Mazur, "GaAs under ultrafast excitation: response of the dielectric function," *Phys. Rev. Lett.*, vol. 80, p. 185, 1998.

[37] C. W. Siders, A. Cavalleri, K. Sokolowski-Tinten, C. Toth, T. Guo, M. Kammler, M. H. v. Hoegen, K. R. Wilson, D. v. d. Linde, and C. P. J. Barty, "Detection of nonthermal melting by ultrafast X-ray diffraction," *Science*, vol. 286, p. 1340, 1999.

[38] A. Rousse, C. Rischel, S. Fourmaux, I. Uschmann, S. Sebban, G. Grillon, P. Balcou, E. Foster, J. P. Geindre, P. Audebert, J. C. Gauthier, and D. Hulin, "Non-thermal melting in semiconductors measured at femtosecond resolution," *Nature*, vol. 410, p. 65, 2001.

[39] A. M. Lindenberg, J. Larsson, K. Sokolowski-Tinten, K. J. Gaffney, C. Blome, O. Synnergren, J. Sheppard, C. Caleman, A. G. MacPhee, D. Weinstein, D. P. Lowney, T. K. Allison, T. Matthews, R. W. Falcone, A. L. Cavalieri, D. M. Fritz, S. H. Lee, P. H. Bucksbaum, D. A. Reis, J. Rudati, P. H. Fuoss, C. C. Kao, D. P. Siddons, R. Pahl, J. Als-Nielsen, S. Duesterer, R. Ischebeck, H. Schlarb, H. Schulte-Schrepping, T. Tschentscher, J. Schneider, D. v. d. Linde, O. Hignette, F. Sette, H. N. Chapman, R. W. Lee, T. N. Hansen, S. Techert, J. S. Wark, M. Bergh, G. Huldt, D. v. d. Spoel, N. Timneanu, J. Hajdu, R. A. Akre, E. Bong, P. Krejcik, J. Arthur, S. Brennan, K. Luening, and J. B. Hastings, "Atomic-scale visualization of inertial dynamics," *Science*, vol. 308, p. 392, 2005.

[40] J. Hohlfeld, J. G. Muller, S.-S. Wellershof, and E. Matthias, "Time-resolved thermoreflectivity of thin gold films and its dependence on film thickness," *Appl. Phys. B*, vol. 64, p. 387, 1997.

[41] *American Institute of Physics Handbook*. New York: McGraw-Hill, 3rd ed., 1972.

[42] S. I. Anisimov, B. L. Kapeliovich, and T. L. Perelman, "Electron emission from metal surfaces exposed to ultrashort laser pulses," *Sov. Phys. JETP*, vol. 39, p. 375, 1974.

[43] C. V. Shank, R. Yen, and C. Hirlimann, "Time-resolved reflectivity measurements of femtosecond-optical-pulse-induced phase transitions in silicon," *Phys. Rev. Lett.*, vol. 50, p. 454, 1983.

[44] S. K. Sundaram and E. Mazur, "Inducing and probing non-thermal transitions in semiconductors using femtosecond laser pulses," *Nature Materials*, vol. 1, p. 217, 2002.

[45] K. Sokolowski-Tinten, C. Blome, J. Blums, A. Cavalleri, C. Dietrich, A. Tarasevitch, I. Uschmann, E. Forster, M. Kammler, M. Horn-von Hoegen, and D. v. d. Linde, "Femtosecond X-ray measurement of coherent lattice vibrations near the Lindemann stability limit," *Nature*, vol. 422, p. 287, 2003.

[46] P. Stampfli and K. H. Bennemann, "Time dependence of the laser-induced femtosecond lattice instability of Si and GaAs: Role of longitudinal optical distortions," *Phys. Rev. B*, vol. 49, p. 7299, 1994.

[47] J. A. Kash, J. C. Tsang, and J. M. Hvam, "Subpicosecond time-resolved Raman spectroscopy of LO phonons in GaAs," *Phys. Rev. Lett.*, vol. 54, p. 2151, 1985.

[48] D. v. d. Linde, K. Sokolowski-Tinten, and J. Bialkowski, "Laser-solid interaction in the femtosecond time regime," *Appl. Surf. Sci*, vol. 109, p. 1, 1997.

[49] J. Shah, *Ultrafast Spectroscopy of Semiconductors and Semiconductor Nanostructures.* Berlin: Springer-Verlag, 1996.

[50] A. H. Zewail, *Femtochemistry: Ultrafast Dynamics of the Chemical Bond.* Singapore: World Scientific, 1994.

[51] M. Cardona, *Modulation Spectroscopy.* New York: Academic, 1969.

[52] C. Guo and A. J. Taylor, "Nonlinear optical study of the Fermi-surface oscillation in gold induced by acoustic-phonon excitation," *Phys. Rev. B*, vol. 64, p. 245106, 2001.

[53] P. Callan, A. M. T. Kim, C. A. D. Roeser, and E. Mazur, "Universal dynamics during and after ultrafast laser-induced semiconductor-to-metal transitions," *Phys. Rev. B*, vol. 64, p. 073201, 2001.

[54] C.-K. Sun, F. Valle, L. H. Acioli, E. P. Ippen, and J. G. Fujimoto, "Femtosecond-tunable measurement of electron thermalization in gold," *Phys. Rev. B*, vol. 50, p. 15337, 1994.

[55] R. W. Boyd, *Nonlinear Optics.* San Diego: Academic Press, 1992.

[56] A. Yarif, *Quantum Electronics.* New York: Wiley, 3rd. ed., 1989.

[57] M. C. Downer, R. L. Fork, and C. V. Shank, "Femtosecond imaging of melting and evaporation at a photoexcited silicon surface," *J. Opt. Soc. Am. B*, vol. 2, p. 595, 1985.

[58] J. R. Dwyer, C. T. Hebeisen, R. Ernstorfer, M. Harb, V. B. Deyirmenjian, R. E. Jordan, and R. J. D. Miller, "Femtosecond electron diffraction: making the molecular movie," *Phil. Trans. R. Soc. A*, vol. 364, p. 741, 2006.

[59] B. J. Siwick, J. R. Dwyer, R. E. Jordan, and R. J. D. Miller, "Femtosecond electron diffraction studies of strongly driven structural phase transitions," *Chem. Phys.*, vol. 299, p. 285, 2004.

[60] C. A. D. Roeser, A. M.-T. Kim, P. Callan, L. Huang, E. N. Glezer, Y. Siegal, and E. Mazur, "Femtosecond time-resolved dielectric function measurements by dual-angle reflectometry," *Rev. Sci. Instrum.*, vol. 74, p. 3413, 2003.

[61] C. A. D. Roeser, M. Kandyla, A. Mendioroz, and E. Mazur, "Optical control of coherent lattice vibrations in tellurium," *Phys. Rev. B*, vol. 70, p. 212302, 2004.

[62] S. Backus, J. Peatross, C. P. Huang, M. M. Murnane, and H. C. Kapteyn, "Ti:sapphire amplifier producing millijoule-level, 21-fs pulses at 1KHz," *Opt. Lett.*, vol. 20, p. 2000, 1995.

[63] R. J. Younkin, J. E. Carey, E. Mazur, J. A. Levinson, and C. M. Friend, "Infrared absorption by conical silicon microstructures made in a variety of backgrounf gases using fetosecond-laser pulses," *J. Appl. Phys.*, vol. 93, p. 2626, 2003.

[64] C. H. Crouch, J. E. Carey, M. Shen, E. Mazur, and F. Y. Genin, "Infrared absorption by sulfur-doped silicon formed by femtosecond laser irradiation," *Appl. Phys. A*, vol. 79, p. 1635, 2004.

[65] J. E. Carey, C. H. Crouch, M. Shen, and E. Mazur, "Visible and near-nfrared responsivity of femtosecond-laser microstructured silicon photodiodes," *Opt. Lett.*, vol. 30, p. 1773, 2005.

[66] G. Yang and Y. R. Shen, "Spectral broadening of ultrashort pulses in a nonlinear medium," *Opt. Lett.*, vol. 9, p. 510, 1984.

[67] A. L. Gaeta, "Catastrophic collapse of ultrashort pulses," *Phys. Rev. Lett.*, vol. 84, p. 3582, 2000.

[68] Y. R. Shen, *The Principles of Nonlinear Optics*. New York: Wiley, 1984.

[69] A. Brodeur and S. L. Chin, "Ultrafast white-light continuum generation and self-focusing in transparent condensed media," *J. Opt. Soc. Am. B*, vol. 16, p. 637, 1999.

[70] J. D. Joannopoulos, R. D. Meade, and J. N. Winn, *Photonic Crystals: Molding the Flow of Light.* Princeton, N. J.: Princeton University Press, 1995.

[71] J. C. Knight, J. Broeng, T. A. Birks, and P. S. J. Russell, "Photonic band gap guidance in optical fibers," *Science*, vol. 282, p. 1476, 1998.

[72] F. Zolla, G. Renversez, A. Nicolet, B. Kuhlmey, S. Guenneau, and D. Felbacq, *Foundations of photonic crystal fibers.* New Jersey: World Scientific, 2005.

[73] J. M. Dudley, X. Gu, L. Xu, M. Kimmel, E. Zeek, P. O'Shea, R. Trebino, S. Coen, and R. S. Windeler, "Cross-correlation frequency resolved optical gating analysis of broadband continuum generation in photonic crystal fiber: simulations and experiments," *Opt. Express*, vol. 10, p. 1215, 2002.

[74] W. J. Wadsworth, A. Ortigosa-Blanch, J. C. Knight, T. A. Birks, T.-P. M. Man, and P. S. J. Russell, "Supercontinuum generation in photonic crystal fibers and optical fiber tapers: a novel light source," *J. Opt. Soc. Am. B*, vol. 19, p. 2148, 2002.

[75] M. N. Islam, G. Sucha, I. Bar-Joseph, M. Wegener, J. P. Gordon, and D. S. Chemla, "Femtosecond distributed soliton spectrum in fibers," *J. Opt. Soc. Am. B*, vol. 6, p. 1149, 1989.

[76] P. K. A. Wai, C. R. Menyuk, Y. C. Lee, and H. H. Chen, "Nonlinear pulse propagation in the neighborhood of the zero-dispersion wavelength of monomode optical fibers," *Opt. Lett.*, vol. 11, p. 464, 1986.

[77] E. B. Treacy, "Optical pulse compression with diffraction gratings," *IEEE J. Quant. Elect.*, vol. QE-5, p. 454, 1969.

[78] D. Strickland and G. Mourou, "Compression of amplified chirped optical pulses," *Opt. Commun.*, vol. 56, p. 219, 1985.

[79] P. Maine, D. Strickland, P. Bado, M. Pessot, and G. Mourou, "Generation of ultrahigh peak power pulses by chirped pulse amplification," *IEEE J. Quant. Elect.*, vol. 24, p. 398, 1988.

[80] W. H. Press, S. A. Teukolsky, W. T. Vetterling, and B. P. Flannery, *Numerical Recipies in C: The Art of Scientific Computing.* New York: Cambridge University Press, 2nd ed., 1992.

[81] P. M. Fauchet, "Enhanced sensitivity of time-resolved reflectivity measurements near Brewster's angle," *IEEE J. Quant. Elect.*, vol. 25, p. 1072, 1989.

[82] A. M.-T. Kim, C. A. D. Roeser, and E. Mazur, "Modulation of the bonding-antibonding splitting in Te by coherent phonons," *Phys. Rev. B*, vol. 68, p. 012301, 2003.

[83] H. J. Zeiger, J. Vidal, T. K. Cheng, E. P. Ippen, G. Dresselhaus, and M. S. Dresselhaus, "Theory for displacive excitation of coherent phonons," *Phys. Rev. B*, vol. 45, p. 768, 1992.

[84] T. K. Cheng, S. D. Brorson, A. S. Kazeroonian, J. S. Moodera, G. Dresselhaus, M. S. Dresselhaus, and E. P. Ippen, "Impulsive excitation of coherent phonons observed in reflection in bismuth and antimony," *Appl. Phys. Lett.*, vol. 57, p. 1004, 1990.

[85] T. K. Cheng, J. Vidal, M. J. Zeiger, G. Dresselhaus, M. S. Dresselhaus, and E. P. Ippen, "Mechanism for displacive excitation of coherent phonons in Sb, Bi, Te, and Ti_2O_3," *Appl. Phys. Lett.*, vol. 59, p. 1923, 1991.

[86] P. Tangney and S. Fahy, "Density-functional theory approach to ultrafast laser excitation of semiconductors: Application to the A_1 phonon in tellurium," *Phys. Rev. B*, vol. 65, p. 054302, 2002.

[87] M. Kandyla, C. A. D. Roeser, E. Mazur, and S. Kudryashov, "Intraband and interband optical deformation potential in femtosecond-laser excited a-Te," *submitted to Phys. Rev. B*, 2006.

[88] M. Hase, K. Mizoguchi, H. Harima, S. Nakashima, M. Tani, K. Sakai, and M. Hangyo, "Optical control of coherent optical phonons in bismuth films," *Appl. Phys. Lett.*, vol. 69, p. 2474, 1996.

[89] M. F. DeCamp, D. A. Reis, P. H. Bucksbaum, and R. Merlin, "Dynamics and coherent control of high-amplitude optical phonons in bismuth," *Phys. Rev. B*, vol. 64, p. 092301, 2001.

[90] D. Beaglehole *Proc. Phys. Soc. (London)*, vol. 85, p. 1007, 1965.

[91] E. D. Palik, *Handbook of optical constants of solids.* New York: Academic Press, 1985.

[92] B. Segall, "Energy bands of aluminum," *Phys. Rev.*, vol. 124, p. 1797, 1961.

[93] H. Ehrenreich, H. R. Philipp, and B. Segall, "Optical properties of Aluminum,"

Phys. Rev., vol. 132, p. 1918, 1963.

[94] J. C. Miller, "Optical properties of liquid metals at high temperatures," *Philos. Mag.*, vol. 20, p. 1115, 1969.

[95] M. A. Havstad, W. M. II, and S. A. Self, "Apparatus for the measurement of the optical constants and thermal radiative properties of pure liquid metals from 0.4 to 10 μm," *Rev. Sci. Instrum.*, vol. 64, p. 1971, 1993.

[96] S. Krishnan and P. C. Nordine, "Optical properties of liquid aluminum in the energy range 1.2-3.5 eV," *Phys. Rev. B*, vol. 47, p. 11780, 1993.

[97] L. X. Benedict, L. E. Klepeis, and F. H. Streitz, "Calculation of optical absorption in Al across the solid-to-liquid transition," *Phys. Rev. B*, vol. 71, p. 064103, 2005.

[98] L. A. Akashev and V. I. Kononenko, "Optical properties of liquid aluminum and Al-Ce alloy," *High Temperature*, vol. 39, p. 384, 2001.

[99] B. J. Siwick, J. R. Dwyer, R. E. Jordan, and R. J. D. Miller, "An atomic-level view of melting using femtosecond electron diffraction," *Science*, vol. 302, p. 1382, 2003.

[100] A. A. Ischenko, V. V. Golubkov, V. P. Spiridonov, A. V. Zgurskii, A. S. Akhmanov, M. G. Vabischevich, and V. N. Bagratashvili, "A stroboscopical gas-electron diffraction method for the investigation of short-lived molecular species," *Appl. Phys. B*, vol. 32, p. 161, 1983.

[101] S. Williamson, G. Mourou, and J. C. M. Li, "Time-resolved laser-induced phase transformation in aluminum," *Phys. Rev. Lett.*, vol. 52, p. 2364, 1984.

[102] J. C. Williamson, M. Dantus, S. B. Kim, and A. H. Zewail, "Ultrafast diffraction and molecular-structure," *Chem. Phys. Lett.*, vol. 196, p. 529, 1992.

[103] H. Ihee, V. A. Lobastov, U. M. Gomez, B. M. Goodson, R. Srinivasan, C. Y. Ruan, and A. H. Zewail, "Direct imaging of transient molecular structures with ultrafast diffraction," *Science*, vol. 291, p. 458, 2001.

[104] R. C. Dudek and P. M. Weber, "Ultrafast diffraction imaging of the electrocyclic ringopening reaction of 1,3-cyclohexadiene," *J. Phys. Chem.A*, vol. 105, p. 4167, 2001.

[105] B. Rethfeld, A. Kaiser, M. Vicanek, and G. Simon, "Ultrafast dynamics of nonequilibrium electrons in metals under femtosecond laser irradiation," *Phys.*

Rev. B, vol. 65, p. 214303, 2002.

[106] D. F. Price, R. M. More, R. S. Walling, G. Guethlein, R. L. Shepherd, R. E. Stewart, and W. E. White, "Absorption of ultrafast laser pulses by solid targets heated rapidly to temperatures 1-1000 eV," *Phys. Rev. Lett.*, vol. 75, p. 252, 1995.

[107] B. Huttner, "Optical properties of polyvalent metals in the solid and liquid state: aluminium," *J. Phys.: Condens. Matter*, vol. 6, p. 2459, 1994.

[108] X. Y. Wang and M. C. Downer, "Femtosecond time-resolved reflectivity of hydrodynamically expanding metal surfaces," *Opt. Lett.*, vol. 17, p. 1450, 1992.

[109] C. V. Shank and E. P. Ippen, "Anisotropic absorption saturation with picosecond pulses," *Appl. Phys. Lett.*, vol. 26, p. 62, 1975.

[110] E. P. Ippen and C. V. Shank, "Techniques for measurement," in *Ultrashort Light Pulses* (S. L. Shapiro, ed.), Berlin: Springer, 1977.

[111] Z. Vardeny and J. Tauc, "Hot-carrier thermalization in amorphous silicon," *Phys. Rev. Lett.*, vol. 46, p. 1223, 1981.

[112] Z. Vardeny and J. Tauc, "Picosecond coherence coupling in the pump and probe technique," *Opt. Commun.*, vol. 39, p. 396, 1981.

[113] K. L. Hall, G. Lenz, A. M. Darwish, and E. P. Ippen, "Subpicosecond gain and index nonlinearities in InGaAsP diode lasers," *Opt. Commun.*, vol. 111, p. 589, 1994.

[114] P. Borri, F. Romstad, W. Langbein, A. E. Kelly, J. Mork, and J. M. Hvam, "Separation of coherent and incoherent nonlinearities in a heterodyne pump-probe experiment," *Opt. Express*, vol. 7, p. 107, 2000.